FORSCHUNGSZENTRUM ROSSENDORF FZR
Mitglied der Wissenschaftsgemeinschaft Gottfried Wilhelm Leibniz

WISSENSCHAFTLICH-TECHNISCHE BERICHTE
FZR-387
Juli 2003
ISSN 1437-322X

Anita Peeva

Microstructural Characterization and Engineering of Defects in Silicon

Herausgeber:
Forschungszentrum Rossendorf e.V.
Postfach 51 01 19
D-01314 Dresden
Telefon +49 351 26 00
Telefax +49 351 2 69 04 61
http://www.fz-rossendorf.de/

FORSCHUNGSZENTRUM ROSSENDORF
WISSENSCHAFTLICH-TECHNISCHE BERICHTE
FZR-387
Juli 2003

Anita Peeva

Microstructural Characterization and Engineering of Defects in Silicon

Dissertation

Microstructural Characterization and Engineering of Defects in Silicon

Dissertation

Zur Erlangung des akademischen Grades

Doctor rerum naturalium
(Dr. rer. nat.)

vorgelegt

der Fakultät Mathematik und Naturwissenschaften
der Technischen Universität Dresden

von

Dipl.-Phys. Anita Peeva
geboren am 6 April 1971 in Sofia, Bulgarien

Gutachter:	Prof. Dr. W. Möller, FZ Rossendorf, Technische Universität, Dresden
	Prof. Dr. U. Gösele, Max-Planck-Institut für Mikrostrukturphysik, Halle
	Prof. Dr. B.G. Svensson, University of Oslo
Vorsitzender der Promotionskommision:	Prof. Dr. G. Soff, Technische Universität, Dresden

Eingereicht am : 19.12.2002
Tag der Verteidigung: 06.06.2003

Contents

page

Chapter 1

Chapter 2

Chapter 3

Chapter 4

Chapter 6

Chapter 1

Introduction

Transition metals are unintentionally introduced into silicon at all production stages of microelectronic devices. Although bulk metal concentrations are generally very low, impurities tend to accumulate in active device regions. This is frequently detrimental because the transition metal solutes in Si possess properties that can lead to degradation of electronic properties even when the average metal concentration is less than one atom per cubic micrometer. Among these properties is a very rapid interstitial diffusion that allows transport over macroscopic distances during the heat treatments associated with the device processing [Web83]. In the extreme case of Cu, recent experimental results indicate a room-temperature diffusion rate sufficient to produce transport over several tenths of millimetres in 1h [Ista98]. Equally important is the small solubility of the metals in Si; typically, solution enthalpies of several electron volts per atom result in extremely small concentrations in equilibrium with the metal-silicide phase at temperatures where diffusion is still rapid [Web83]. Where these two characteristics are combined with the pronounced barriers to metal-silicide nucleation and growth in defect-free region of the Si lattice, there is the possibility of impurity atoms converging from a macroscopic volume to precipitate at an isolated lattice irregularity within a high-quality wafer during cooling. Among the locations where precipitation occurs is the base of gate oxide in metal-oxide-semiconductor structures, resulting in electrical breakdown [W-Leu98]. Within the Si matrix, metal atoms in solution and metal-silicide precipitates both introduce deep electronic levels into the band gap [Sei98]. These states may reduce minority-carrier lifetimes by orders of magnitude, degrading the performance of devices. Fast diffusing transition elements can also cause increase of leakage currents or reduction of the breakdown strength of gate oxides [Wen89]. The importance of these effects is reflected in metal-impurity specifications for starting wafers used for high-density memories. The metal impurity concentrations are projected to be decreased to a value as low as 2.5×10^9 atoms/cm^2 [roa97].

In dealing with metal impurities in Si, manufacturers often supplement clean-room procedures with the use of gettering, a class of procedures whereby sinks for the diffusing impurities are introduced into a noncritical region of the wafer. Gettering has proved to be very effective, and is employed in microelectronics. High performance, reliability and production yield are required at minimum cost. To these objectives, the importance of understanding of the gettering mechanisms has been widely recognised.

During the gettering development a specialised nomenclature has emerged. For example, “internal gettering” and “intrinsic gettering” generally refer to the controlled precipitation of oxygen in Cz-Si leading to nucleation of metal silicides [Gill90b], while “extrinsic gettering” and “external gettering” usually refer to sinks of any type that are introduced at the back of the wafer [Apel94]. “Precipitation gettering” and “relaxation gettering” include all processes based on metal-silicide precipitation [Bor95, Kon96]. “Segregation gettering” denotes equilibrium enrichment of metal impurities in a portion of the Si wafer or in a deposited back side layer that results from effects other than metal-silicide precipitation; such effects include atomic pairing with dopants and atomic trapping at defects [Tho82, Hug98]. Metal gettering due to the interaction between metal impurities and point-defect gradients associated with dopant indiffusion has been called “dopant-diffusion gettering” and “injection gettering” [Schrö91].

Circumstances, such as annealing conditions, the use of Si-on-insulator structures and the need to reduce impurity concentrations to very low levels, may require the use of gettering sinks that are beneath the device zone with the property of remaining active at metal concentrations below supersaturation. High-energy (up to several MeV) ion implantation is among the most promising gettering methods for achieving low concentration of metals in Si (below 10^{-10} cm^{-3}) [Wong88]. It is known to produce damage that is capable of gettering metal impurities as well as intrinsic oxygen. In the so called “proximity gettering” technique a gettering layer is formed in the bulk of the Si wafer near the active device area by means of ion implantation and annealing [Che89]. The aim of this procedure is to getter unwanted metal impurities inside of a prefabricated buried damage layer. This damage layer is located where most of the implanted atoms come to rest. The gettering ability of such a layer has been proven by several analytical techniques, such as secondary ion mass spectrometry (SIMS), carrier lifetime measurements, deep level transient spectroscopy (DLTS) and Rutherford backscattering channelling spectrometry (RBS/C). Moreover, it has been shown that the suitably positioned gettering layer has practically no influence on the properties of *p-n* junctions formed within the near surface layer of the wafer [Ben96]. The proximity gettering has been extensively studied in view of its potential application in advanced large scale integration technology.

During ion implantation, damage is created in the whole depth range from the wafer surface to the position where the implanted ions come to rest. The total distance traveled by the ion in the material is called range R. In this thesis, the depth position of the implanted ions is given by the projection of R along the direction perpendicular to the surface of the wafer, mean projected ion range R_p. When high-energy ion implantation is explored as a means to introduce defect-related gettering sites beneath the device region of wafers, the damage from the surface to the R_p region must be annealed out and only extended defects at R_p are needed to survive during the heat treatment. The trends of the device technology require lowering of the thermal budget for the device processing. In relation to these requirement, undesired strong gettering in Si after MeV ion implantation and annealing was detected at depths between the surface and R_p, indicating the presence of residual defects therein. This phenomena is called "the $R_p/2$ effect" irrespective of the actual shape of the defect depth distribution, and was first reported by Tamura et al. [Tam91] with regard to gettering of intrinsic oxygen in high-energy ion-beam processed Cz Si. A number of papers have been published about the gettering abilities and the properties of the $R_p/2$ defects in MeV ion implanted and annealed Si in the last 10 years. Chapter 2 focuses on reviewing the major aspects and the current understanding of the processes causing the $R_p/2$ effect in the high-energy ion implanted Si. Different experimental approaches have been applied in order to determine the nature of the $R_p/2$ defects. The size of the defects responsible for the metal gettering at $R_p/2$ has been reported to be below the resolution limit of the transmission electron microscopy (TEM). The conventional variable-energy positron annihilation spectroscopy (PAS) does not show clearly the existence of vacancy-type defects in the $R_p/2$ region. In most cases the existence of defects at $R_p/2$ was verified experimentally by labelling them with metal and measuring the metal concentration depth profile. The ballistic models predict special separation of the vacancies and interstitials created during ion implantation process. This separation results from the creation of static vacancy and mobile, forward-directed interstitial atom. There are two different explanations proposed for the existence of the $R_p/2$ effect. The first explanation is based on the assumption that a full local vacancy-interstitial recombination takes place during annealing, vacancies are supposed to remain in the region from the surface up to about R_P after annealing while interstitials are expected to remain deeper than the region where the vacancies are located, up to slightly beyond R_P. It was suggested that the remaining vacancies are the origin of the defects responsible for the metal gettering at $R_P/2$. The second proposed explanation for the existence of defects in the $R_P/2$ region assumes that during the annealing the implantation induced defects do not annihilate locally. There could be remains from both kind of defects, vacancies and interstitials that can agglomerate during annealing and form interstitial type defects as well as vacancy type defects that can co-exist in the $R_P/2$ region. The idea that non-complete vacancy-interstitial local recombination takes place during the annealing is supported by some experimental findings showing co-existence of supersaturation of vacancies and interstitials in the $R_P/2$ region after annealing as well as diffusion of interstitials from the R_P region to the $R_P/2$ region during the annealing. At this point the existing experimental findings cannot prove without any doubts the nature of the $R_P/2$ defects that act as gettering centres for metals.

The main goals of this study are:

- To get a clear understanding of the nature of the $R_P/2$ defects in the high-energy ion implanted Si. Therefore improvement of the TEM imaging of the $R_P/2$ defects was carried out in order to achieve clear visualisation of the $R_P/2$ defects and determine their nature.
- To investigate the role of the ion implantation process and the annealing processes for the defect evolution in the $R_P/2$ region during high energy ion implantation and subsequent annealing. MeV ion implantations in different geometry and multiple implantations were carried out using different kind of Si substrates. In order to verify the general appearance of the $R_P/2$ effect in Si substrates after ion implantation and subsequent annealing, the $R_P/2$ defect related study was extended to low defect production regimes by means of low energy implantations of light ion in random and channel direction at different implantation temperatures.
- To optimise the ion implantation conditions in combination with annealing at relatively low temperature in order to avoid the $R_P/2$ defect production. This defect engineering is necessary for the further application of the proximity gettering under low thermal budget for annealing required by the device technology.

Chapter 2

Aspects of the $R_p/2$ effect

The $R_p/2$ effect is illustrated in Fig. 2.1 [Kög99a]. A gettering R_p layer at a depth of about 2.7 μm has been formed by 3.5 MeV ion implantation, 5×10^{15} Si $^{+}$cm^{-2} in Cz-Si. The implantation damage was annealed by Rapid Thermal Annealing (RTA) in an Ar ambient in the temperature range 700-1150 °C for times between 5 s and 5 min. All samples were contaminated with Cu by ion implantation on the rear surface. The redistribution of Cu throughout the sample bulk was performed simultaneously with the damage annealing. Cu depth distributions measured by SIMS after Si^+ ion implantation for different annealing temperature are shown in Fig. 2.1 (a). With the exception of the highest temperature (1150 °C) a well-defined double-peak structure is observed. The deeper peak correlates with the region around R_p. In this region the implanted ions come to rest, and therefore at temperatures in excess of 850 °C a secondary-defect band is formed. The Cu gettering in this region is consistent with what is known about the gettering behaviour of impurities in Si^+- implanted Si [Kur93]. However, in the depth range between the surface and R_p a second defect band appears which is centred at about $R_p/2$. The accumulation of Cu in this region evidences the presence of damage therein. At lower temperatures the Cu depth profile is characterised by a broad distribution which becomes narrower for higher temperatures. After annealing at the highest temperature of 1150 °C, the gettering peak at $R_p/2$ has disappeared. This means that the defects acting as gettering sites have been removed by the annealing cycle. The microstructure of the sample after annealing at 1000 °C is shown in Fig. 2.1 (b). The defects acting as gettering sites are of different kind in the two gettering regions around R_p and $R_p/2$, as shown by microscopy. A well-defined band of extrinsic dislocations has formed around R_p. At the depth of the gettering band around $R_p/2$, no defects are observed by TEM. The defects at $R_p/2$ are assumed to be very small defect complexes as they are not resolved by Cross-section TEM (XTEM). This is consistent with the results reported in the $R_p/2$ effect related literature [Tam91, Aga96, Kon97, Kög98, Kov98a, Kov98b, Bro98].

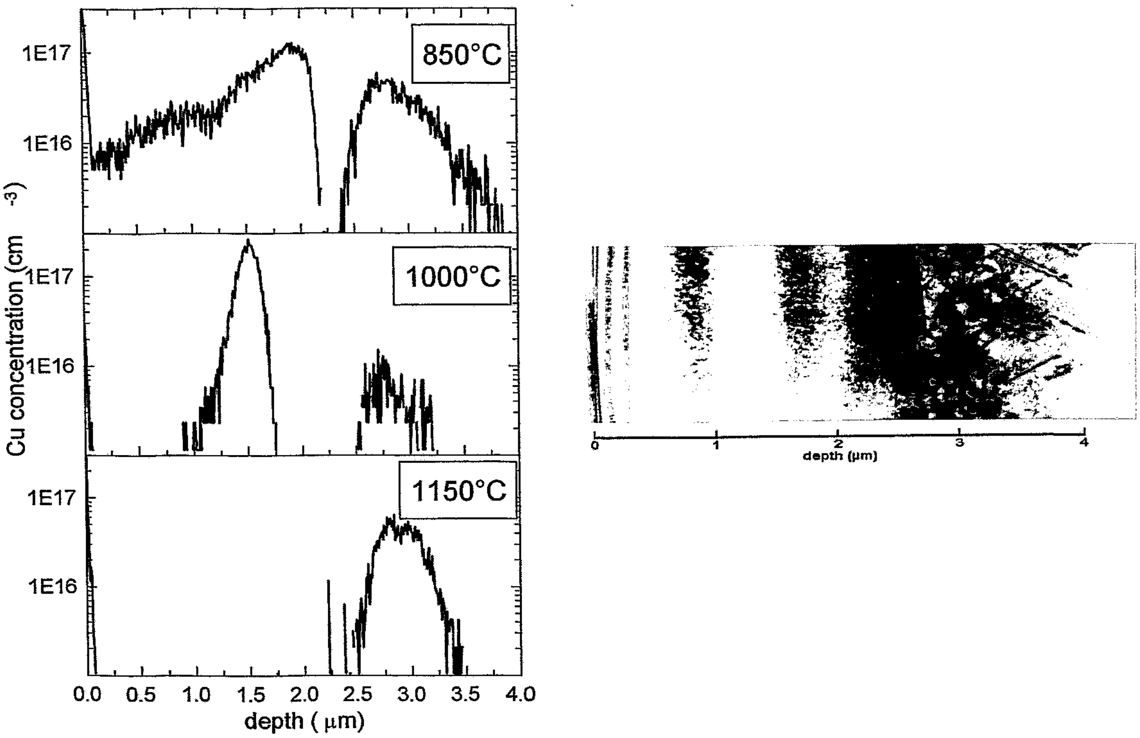

(a) (b)

Fig.2.1 Cu depth profiles for 3.5 MeV, $5\text{x}10^{15}\text{Si}^{+}\text{cm}^{-2}$ implanted n-type (100) Cz-Si after RTA for 30s (a) combined with a TEM bright field micrograph (b). The micrograph is obtained after annealing at 1000°C.

Gettering of both, metal impurities and intrinsic oxygen around $R_p/2$ has been found for a variety of implanted ions in different type of Si substrate after conventional furnace annealing as well as after RTA at temperatures between 800 and 1000°C as summarised in Tab. I.1.

The next paragraphs will give an overview of the models reported in the literature, both on the nature of the $R_p/2$ defects and the metal gettering mechanisms of the MeV ion implantation induced $R_p/2$ defects.

Substrate	**Implanted species**	**Implantation conditions**	**Annealing**	**Gettered species**	**Reference**
Cz	C	2.5 MeV, 5×10^{15} at/cm^2	850°C, 30s , RTA 1000°C, 30s, RTA	Fe	[Kög98]
Cz	F	1.8 MeV, 5×10^{15} at/cm^2	1000°C/60 min, furnace	O	[Tam91]
Cz	Si	140 keV, 1×10^{16} at/cm^2	850°C, 1h, furnace	Cu	[Str01a] [Str01b]
Cz	Si	245 keV, 3×10^{15} at/cm^2-1.4×10^{16} at/cm^2	850°C, 1h, furnace	Au	[Will01]
Fz	Si	1 MeV, 2 MeV, 8 MeV, 1×10^{16} at/cm^2	850-1000°C, 10 min furnace +750°C, 2h furnace 950°C, 10s-10 min RTA + 750°C, 2h furnace	Au	[Ven98]
Cz	Si	1.8 MeV, 5×10^{15} at/cm^2	1000°C/60 min, furnace	O	[Tam91]
Fz	Si	2 MeV, 1×10^{15} at/cm^2	800°C, 1h,+ 800-950°C, 1-3h, furnace	Au	[{Kal00] [Kal01b]
Epi	Si	2.3 MeV, 1×10^{15} at/cm^2	900°C, 1h, furnace	Fe	[Roz00]
Cz	Si	2.3 MeV, 1×10^{15} at/cm^2	800-1000°C, 30 min, furnace	O	[Kon97]
Cz	Si	2.3 MeV, 1×10^{15} at/cm^2	800°C, 30 min, furnace	Cu	[Kon97]
Cz	Si	2 MeV, 1×10^{15} at/cm^2	1000°C, 1h, furnace	O	[Aga96]
Epi	Si	2.3 MeV, 1×10^{15} at/cm^2	900°C, 1h +600-900°C, 1-2h, furnace	Fe	[Kov98a]
Epi	Si	2.3 MeV, 1×10^{15} at/cm^2	900°C, 1h+600-900°C, 1h, furnace	Cu	[Kov98b]
Epi	Si	2.3 MeV, 1×10^{15} at/cm^2	900°C, 1h +600-900°C, 1h, furnace	Ni	[Kov98b]
Cz, Epi	Si	2.3 MeV, 1×10^{15} at/cm^2	900°C, 1h +600-800°C, 1h, furnace	Fe,Cu, Ni	[Bro98]
Cz	Si	2.3 MeV, 1×10^{15} at/cm^2	900°C, 1h +800-1000°C, 1h, furnace	O	[Bro98]
Fz	Si	2 MeV, $1\times10^{15\text{-}16}$ at/cm^2	815°C, 10 min + 750°C, 2-24h, furnace	Au	[Kal01a]
Cz	Si	3.5 MeV, 5×10^{15} at/cm^2	850°C, 30s1000°C, 30 900°C, 30s, 900°C, 180s RTA	Cu	[Kög98] [Kög99a]
Cz	P	2 MeV, 5×10^{15} at/cm^2	1000°C/60 min, furnace	O	[Tam91]
Cz	Ge	3 MeV, 5×10^{15} at/cm^2	1000°C/60 min, furnace	O	[Tam91]
Cz	Ge	4 MeV, 5×10^{15} at/cm^2	1150°C, 30s, RTA	Fe	[Kög98]
Epi	Ge	4.2 MeV, 5×10^{15} at/cm^2	900°C, 1h, furnace	Fe	[Roz00]
Cz	As	3 MeV, 5×10^{14} at/cm^2 3 MeV, 1×10^{15} at/cm^2 3 MeV, 5×10^{15} at/cm^2	1000°C/60 min, furnace	O	[Tam91]

Table I.1 Literature review on the experimental parameters for which the $R_P/2$ effect was observed.

2.1 The nature of the $R_p/2$ defects

The ballistic models of Transport of Ions in Matter (TRIM) [Bier80] predict that during the ion implantation process two distinct regions are created containing a net excess of either vacancies or interstitials. These two regions are formed because of the spatial separation of point defects due to the momentum component of the displaced Si atoms into the beam direction. This displacement results from the creation of a static vacancy and a mobile, forward-directed interstitial host atom. An experimental concept for comparing the depth profiles of vacancy-type and interstitial-type defects in ion implanted Si was recently proposed [Pell01]. This concept is based on DLTS measurements. The vacancy profile was represented by the vacancy-oxygen center while the interstitial profile was attributed to the substitutional carbon-interstitial carbon pair. The authors suggest that the interstitial profile is displaced by ~ 0.5 μm towards larger depths compared to that of the vacancy profile.

Assuming *a complete local vacancy-interstitial annihilation during annealing* one can calculate the depth profiles of the remaining vacancies and interstitials by simply subtracting their respective depth profiles. Such depth profiles of the excess vacancies and interstitials for the case of 3.5 MeV Si^+ion implantation into Si are shown in Fig. 2.2 and illustrate the expected formation of a vacancy-rich layer from the surface nearly up to R_p and the formation of an interstitial-rich region slightly extended beyond the R_p depth.

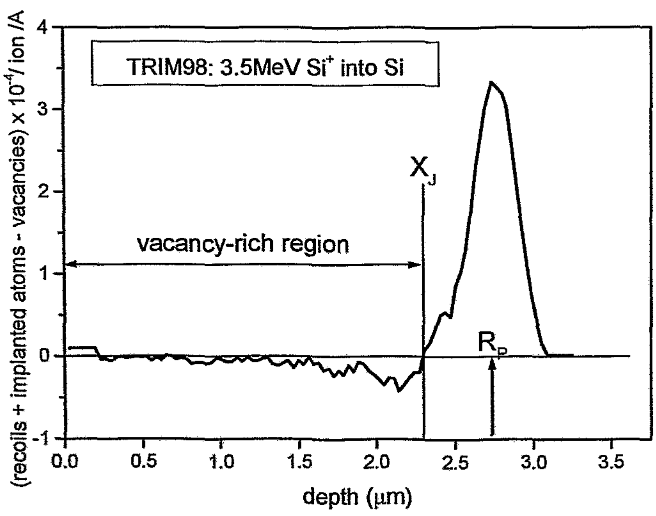

Fig. 2.2 The excess vacancy and interstitial profiles for 3.5 MeV Si^+ implantation into Si calculated by TRIM'98; x_j - junction depth, indicating the transition from vacancy rich region to interstitial rich region.

For the MeV ion implantation, the $R_p/2$ gettering effect is attributed to the formation of excess vacancies at the $R_p/2$ region [Holl96, Kon97, Bro98, Kov98a, Kov98b,Ven98, Hei99].

The major part of the studies presented in Tab. I.1 report that no defects are visible in the $R_P/2$ region by means of TEM. There are a few studies that report on TEM observation of cavities in the region shallower than R_P. These cavities have been observed extremely seldom by TEM only under special conditions characterised by very high damage production during the performed ion implantations:

1) high fluence (~10^{18} at/cm^2) oxygen implantation at elevated temperature (~500°C) [Vena92, Zhou93, Holl95]. In this case not only vacancies were observed at $R_P/2$ but also high-density dislocations and aggregates of SiO_2 precipitates;

2) implantation of heavy ions i.e. Ge^+ at relatively high fluence (5×10^{15} at/cm^2) [Roz00];

3) high fluence (1.4×10^{16} at/cm^2) Si^+ ion implantation of low energy (245 keV) [Will01], both voids and interstitial loops are found to coexist.

The cavities that were observed in the above cases are very rarely distributed. Their concentration and depth distribution does not mirror the metal depth profile and concentration in the $R_P/2$ region. Therefore the observed cavities cannot be attributed to be the major gettering centres for metals.

The existence of defects at $R_P/2$ was verified experimentally in the most cases only by means of the impurity decoration method. The so called "Au labelling" technique has been used to measure the concentration and to profile the defect cluster distribution at $R_P/2$ [Ven98, Kal00, Kal01]. The use of Au for *vacancy* clusters labelling was attributed to the kick-out diffusion mechanism, by which Au diffuses in Si. This diffusion mechanism predicts enhanced formation of substitutional Au in the vicinity of interstitial sinks. However, Au always was found to be gettered not only to the $R_P/2$ defects but to the R_P damage as well, which is of interstitial type.

The conventional variable-energy PAS was used to investigate the depth distribution of vacancy-type defects in the samples revealing metal gettering at $R_P/2$ [Bro98, Kög99]. The data for the samples annealed at temperatures between 800°C and 1000°C (typical annealing temperatures in the $R_P/2$ effect studies) do not show clearly the existence of vacancy-type defects. This means, that the concentration of residual open volume defects is below the sensitivity of the PAS technique, which was applied.

However, a recent PAS investigation using low positron energy, combined with a stepwise removing of the surface in order to obtain high-resolution defect depth profiling, shows the presence of open volume defects in the $R_P/2$ region [Kra00].

The experimental findings discussed above give evidences for existence of vacancy type defects in the region shallower than R_P. However, the concentration of these defects is too low to explain the metal gettering in the same region. It has not been proven so far are these defects agglomerates from the predicted excess vacancies at $R_P/2$ or they result from incomplete vacancy-interstitial recombination during annealing. Moreover, some other experimental results support the idea of non-complete vacancy-interstitial local recombination. It was found out that both type of defects, vacancies and interstitials co-exist in the $R_P/2$ region of MeV ion-implanted and annealed Si. The supersaturation of vacancies at $R_P/2$ was monitored by the transient enhanced diffusion (TED) of Sb δ-layers while the TED of B δ-layers in the same region indicates supersaturation of self-interstitials there [Eag97].

At this point the nature of the defects at $R_P/2$ that act like gettering centres for impurities is not undoubtfully clear.

2.2 The influence of oxygen

Due to the crystal growth process, oxygen is the impurity most frequently present in Si. Oxygen is known to form complexes with vacancies (V-O), the so called E-centers. Precipitation of oxygen in silicon is a process which injects interstitials or consumes vacancies, because of the molar volume difference between elemental Si and its oxide phases. Therefore, it should be energetically favourable for precipitation to occur in a vacancy-rich region, and in fact vacancies are known to enhance oxygen precipitation [Fal97]. The metal gettering capability of the $R_p/2$ region in Cz-Si can be strongly suppressed due to interaction with oxygen [Aga97, Kon97, Bro98]. The behaviour of the transition metals and the oxygen in the $R_p/2$ region is different due to the difference in their solubility and diffusivity. Indeed, at all annealing temperatures for which the $R_p/2$ effect appears (800 – 1000°C) the fast diffusing transition metals, such as Cu and Fe, are introduced into the crystal rapidly at concentrations equal to or below their solid solubility. Because of the low diffusivity of oxygen it is not gettered noticeably at $R_p/2$ defects during annealing at 800°C, allowing the metals (Cu, Fe or Ni) to selectively be gettered therein. With increasing of the annealing temperature up to 900°C, the accumulation of oxygen at both R_p and $R_p/2$ also increases, resulting from the increasing diffusion length of the oxygen during this anneal [Bro98]. Assuming the $R_p/2$ damage layer to be vacancy-rich, the excess vacancies will form complexes with oxygen there when the annealing temperature is high enough to make the oxygen mobile. These sites lead to the further precipitation of oxygen atoms giving rise to the oxygen accumulation at $R_p/2$.

To isolate the simultaneous and competitive gettering between the transition metals and oxygen at $R_p/2$, the investigations can be performed in Float Zone (FZ) or in epitaxial grown (Epi) Si both with at least 2 orders of magnitude lower oxygen concentration than the CZ-Si (oxygen content ~ 10^{18} cm^{-3}). When the Si material has lower concentration of oxygen, a preferential metal trapping occurs at $R_P/2$ [Kon97, Bro98, Kov98a].

2.3 Gettering kinetics

In order to distinguish between the relaxation- and segregation-induced gettering mechanisms (discussed in Chapter 1) and to determine their relative contribution, one should be able to evaluate the impurity concentration during high temperature annealing. This can be done by rapid quenching of samples. Rapid quenching of samples after annealing, which was performed in wide range of temperature and time allowed Koveshnikov et al [Kov98a, Kov98b] to determine the Fe, Cu and Ni gettering by the $R_p/2$ defects as *segregation-induced gettering*. The ability of the $R_p/2$ damage to reduce the metal concentration to well below the thermal equilibrium solubility level is strong evidence of the segregation-induced gettering in the $R_p/2$ region.

Decreasing the ion implantation fluence results in a substantial reduction of the metal concentration captured in the $R_p/2$ [Tam91, Kon97, Kov98a]. The comparison of two 2.3 MeV epi-Si samples implanted with a fluence of 1×10^{15} Si$^+$cm^{-2} and 5×10^{14} Si$^+$cm^{-2} [Kov98a] and annealed at 900°C for 1h shows a significant decrease of the metal concentration at $R_p/2$ region. The results for the sample implanted and annealed in similar conditions [Kon97] with a fluence of 1×10^{14} Si$^+$cm^{-2} shows no $R_p/2$ gettering. The capture of metal at the R_p defects was approximately the same in all samples, indicating a negligible reduction of the gettering site density. Thus, in contrast to the R_p defects, the gettering capacity of the $R_p/2$ damage is very sensitive to the ion implantation fluence.

The slowly cooled samples reveal much higher metal concentrations than the quenched ones [Kon97, Kov98a] Another feature is that during cooling the $R_p/2$ damage has much stronger gettering activity than the R_p damage layer. The $R_p/2$ to R_p Cu peak ratio increases from 0.16 (detected after rapid quenching) to 4 after slow cooling as reported by Kononchuk et al [Kon97, Kov98a]. The same ratio reported for gettering of Fe [Kon97] in the samples treated with the same implantation and annealing conditions is 0.6 for the quenched sample and 0.67 for the slowly cooled sample.

Redistribution of metal between the R_P and the $R_P/2$ regions during a sequence of several 1h annealing steps at different temperatures shows that the metal gettering at the R_p and $R_p/2$ layers is completely reversible [Kov98b]. The metal concentration in the $R_p/2$ region notably increases at temperatures up to 800°C and it is higher than the one at R_p. The metal concentration at R_p is higher then the one at $R_p/2$ at temperatures over 800°C. There is a temperature-dependent equilibrium occupation of the two regions in the temperature range between 600°C and 900°C. In Ref. [Kov.98a] kinetic equations are discussed to describe the temperature dependence of the captured Cu in the $R_p/2$ and R_p region. The calculations reveal the difference between the binding energies for Cu in the $R_p/2$ and R_p regions, $\Delta E^{Cu} = E_{Rp/2} - E_{Rp} = 1.35$ eV, their E_{Rp} being smaller than $E_{Rp/2}$. Such a difference in the binding energies indicates a much stronger gettering ability of the $R_p/2$ region than the R_p region. The capture of metal at R_p above 800°C is explained by the larger number of gettering sites in the R_p region compared to the density of the gettering sites at $R_p/2$. The investigation of the Ni gettering performed under similar implantation and annealing/cooling conditions reveals similar gettering behaviour at the $R_p/2$ and R_p regions.

2.4 Defect decoration in silicon by copper

Copper gettering can be also used as a defect decoration method for detection of very small defects, which sizes are under the resolution of the structural analyses techniques like TEM. The diffusion of interstitial copper, D_{Cu}, in silicon is known to be very fast. It is described by a diffusion coefficient D_{Cu} with a migration barrier for copper diffusion of 0.39 eV, $D_{Cu} = 4.5 \times 10^{-3} \exp(-0.39/ k_BT)$ cm^2/s, [Mes94]. This results in a high mobility even at room temperature. The fast diffusion of Cu at low temperatures allows the defect decoration to be performed during low temperature short time anneals. In this way the original defect structure, which needs to be decorated, is not influenced by the additional thermal treatment. By measuring the depth profile the metal concentration with Secondary Ion Mass Spectrometry (SIMS) or Rutherford Backscattering Spectrometry (RBS) the defects capable to getter Cu can be detected. Using this technique, Cu was found to monitor the presence of interstitial loops as well as voids, being selectively trapped by the voids, if both type of defects coexist. However, if there are insufficient open volume defects to accommodate the Cu, it will also decorate the interstitial loops [Str01a, Str01b].

Special care must be taken about the concentration of Cu impurities inside the wafer, when Cu is used for decoration of small defects. If present in high concentrations, Cu may modify the original defect structure by the Si-interstitial emission that takes place during the Cu precipitation. Below the eutectic temperature of 802°C the phase in equilibrium with silicon is Cu_3Si. A considerable volume expansion is associated with the copper precipitation. For the Cu_3Si it is estimated that the emission of one Si self-interstitial is necessary for two precipitating Cu atoms to allow the formation of strain-free precipitates. The emitted Si interstitials may form punch-out dislocations or interact with the original defect structure that needs to be decorated. TEM studies have shown that platelets surrounded by stacking faults form upon quenching from high temperatures [Sei98].

In the work presented in this thesis low dose Cu contamination was applied in order to decorate the defects in the $R_P/2$ region.

Chapter 3

Experimental

3.1 Ion implantation and annealing conditions

The metal gettering layers were formed by Si^+ ion implantation at energies in the MeV region or He^+ ion implantation at energies in the keV region to the fluences of $5\times10^{15} \div 3.5\times10^{16}$ cm^{-2}. The implantations were done into different kinds of Si substrates i.e. (100)-oriented, n-type CZ-Si; (111)-oriented, p-type FZ-Si; Epi-Si; bond-and-etched silicon-on-insulator substrates (BESOI). The Si^+ implantations were performed with 3 MeV-Tandetron Implanter. The He^+ ion implantations were carried out with 500 keV Implanter. The ion implantations were performed at room temperature unless stated others. The substrate temperature during the implantation process was measured to be up to 100°C depending on the ion current density. The implantations were performed under an orientation of 7° tilt with respect to the crystal axes to prevent channelling effect.

The implantation damage was annealed by thermal treatment in an Ar ambient at temperatures 700° ÷ 900°C. Conventional furnace annealing (FA) was used for long time treatments (30min ÷ 60min). Rapid thermal annealing (RTA) was used for short time anneals (30s ÷ 180s).

The contamination of the samples with Cu was performed by 20 keV Cu^+ ion implantation with 50 keV Implanter to the fluences of 1×10^{12} or 3×10^{13} Cu^+/cm^2. The Cu implantations were performed on the rare face of the samples either before or after the damage annealing. The redistribution of the Cu throughout the sample bulk was performed either simultaneously with the damage annealing or subsequently by an additional RTA treatment at 700°C for 5 min.

3.2 Transmission electron microscopy

In the studies described in this thesis, the TEM analysis was performed in two different transmission electron microscopes, a Philips CM 300 and a JEOL 400, operating at 300 and 400 kV, respectively.

The wave nature of the electrons is used in the transmission electron microscope in order to visualise features which are too small to be observed in the optical microscope. A beam of electrons is accelerated by a high voltage (100-400 kV), passes through the sample, as well as through a set of apertures and electromagnetic lenses and creates an image of the sample on, e. g., a fluorescent screen. The objective lens, placed after the sample holder (Fig. 3.1), produces a picture of the reciprocal space of the sample, in its back focal plane and the real picture of the sample in its image plane. Further projection of either the back focal plane or the image plane decides whether the image on the screen is a picture of the real or the reciprocal space.

There are two important mechanisms, which produce image contrast in the electron microscope.

(1) *Diffraction contrast.* In the bright field imaging (BF), diffracted electrons leaving the lower surface of a crystalline specimen are intercepted by the objective aperture inserted in the back focal plane and prevented from contributing to the image (see Fig 3.1 a). Alternatively only one diffracted beam forms the image in the dark field (DF) mode (see Fig. 3.1 b). Bright field is the mostly used imaging mode in this study. DF mode was used as a part of a technique to determine the nature of defects discussed in details in Chapter 4.1.1. The diffraction (Bragg) contrast of crystalline specimens is caused by the elastically diffracted electrons in Bragg reflections. The interpretation of the TEM images is explained by the dynamical theory of the electron diffraction [Edin35, Rei97]. Electron beams interact strongly with the atoms in a crystal, and any beam can easily be scattered more than ones, i.e. a beam which has been diffracted can be rediffracted. Any electron beam that is oriented at the Bragg angle is ideally oriented to be rediffracted. Dynamical diffraction theory deals with the interaction between primary and reflected electron beams. When the Bragg condition is only met for one point in the reciprocal lattice or one diffraction vector g (usually with small Miller indices, {220} used in this study), *a two-beam case* results, and the primary and reflected beams oscillate in intensity with increasing crystal thickness.

If the Bragg condition is met exactly the so called excitation error is equal to zero, this is a dynamical case. When the Bragg condition is met only approximately (excitation error < 0 or > 0), this is the so called kinematical case.

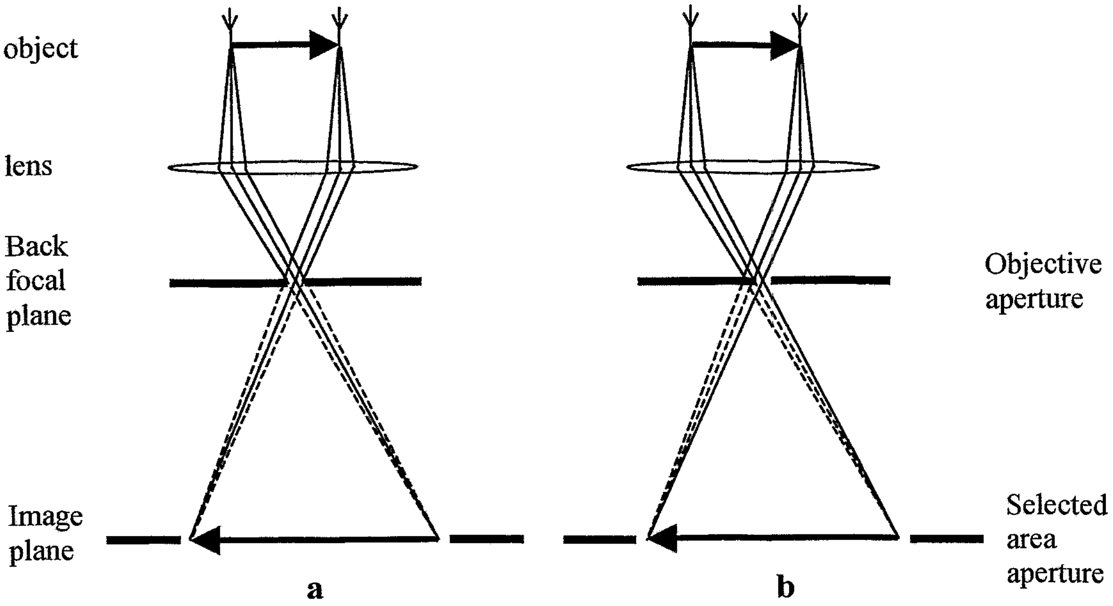

Fig. 3.1 Ray diagrams showing the principles of formation of (a) BF contrast and (b) DF contrast. The dashed rays will not contribute to the final image.

(2) *Phase contrast.* Some of the electrons leaving the specimen are recombined to form the image so that phase differences present at the exit surface of the specimen are converted into intensity differences in the image. In this work (Chapter 4) cavities in silicon substrate were made visible in TEM by means of their phase-contrast under controlled amounts of objective lens defocusing. Images were generally obtained in bright field, on a region of the specimen in which no Bragg reflection was strongly excited. Under these conditions, underfocusing the objective lens by typically 1000 nm yields reasonably sharp images in which the cavity is lighter than the background and is surrounded by a dark fringe. A similar degree of overfocus gives rise to images in which this contrast is reversed, i.e. the cavities appear darker than the background with a light fringe around them.

In transmission *electron diffraction*, the reciprocal space patterns in the back focal plane of the objective lens are projected down to the screen. Mostly used is the technique of selected area electron diffraction (SAED), where a selected area aperture is inserted in the image plane of the objective lens (see Fig. 3.1). This is done to shield certain areas of the sample, i. e., only electrons which have passed a chosen sample area will give intensity to the different patterns. In the work presented in this thesis, the SAED was used to orient the sample in a way that a certain crystallographic direction is parallel to the electron beam. This thesis contains SAED pattern images as a part of a technique for determination of the nature of loops (vacancy or interstitial type) discussed in details in Chapter 4.

An important part of TEM investigation is the specimen preparation. Bulk samples must be prepared for viewing in the TEM so that they became transparent for electrons. Typical thickness of 100 nm or below have to be employed. Obtaining specimens thin enough and containing the defects to be investigated in the right geometry (e.g. in cross-section XTEM) is a crucial point in the TEM studies. In what follows the XTEM specimen preparation techniques that were used for the preparation of the samples investigated in this study will be described.

3.2.1 TEM specimen preparation by ion-milling

The XTEM specimens were prepared conventionally by cutting 2 stripes (3 × 3 mm) of the material and gluing them face–to–face. A dummy Si material was glued to both rear sides of the original material till the thickness of the "sandwich" became 3 mm in order to cut a disk with a diameter of 3 mm. The disk contains the range of interest (see Fig. 3.2a) which is a standard size used of the TEM microscopy holders. Mechanical thinning of the specimen was performed by grinding to get a disk with flat plane-parallel surfaces (thickness ≈ 0.2 mm). As a next step, the sample was dimpled till the central area has thickness of about 5 – 10 μm. For the final thinning the sample was subsequently ion-milled. Ion–milling is a TEM sample preparation technique where the sample material is typically bombarded by argon ions. Thereby material is removed away to cause a small perforation in the middle of the sample in the region of interest. The thinning of the specimen is achieved by sputtering of the near surface atoms of the sample during argon bombardment (see Fig. 3.2 b) performed almost always using commercial ion-milling machines. Due to this ion-milling procedure it is possible to achieve a large, uniform thin area in the centre of the sample (thickness < 100 nm), which is electron-transparent. The thinning process can be prolonged until a hole is generated.

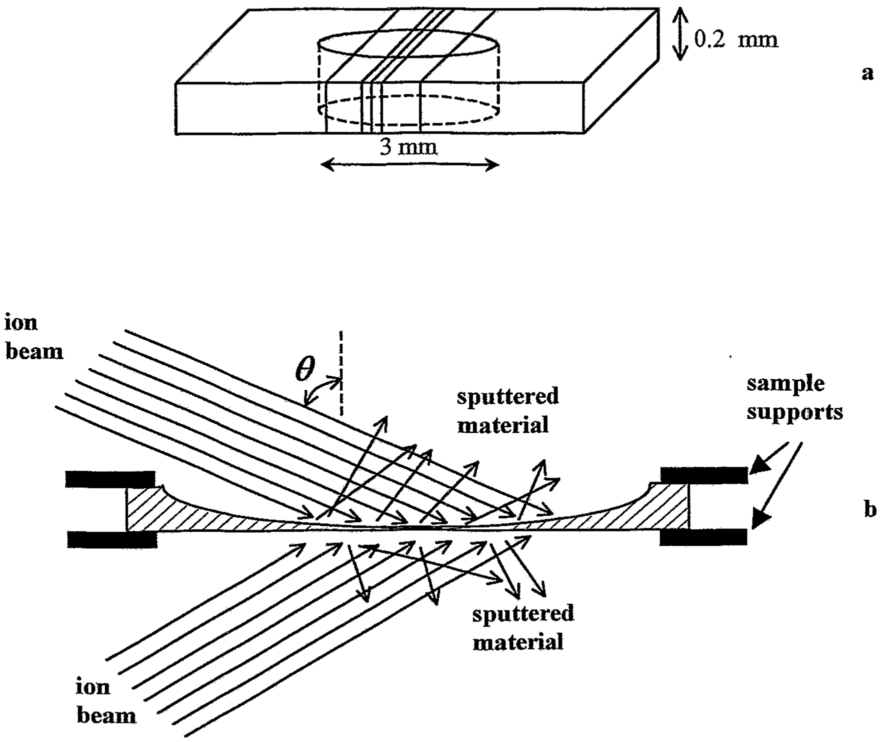

Fig. 3.2 Scheme of cross-section TEM sample preparation: a) two stripes of the material containing areas of interest are glued face-to-face, b) the sample is dimpled on the upper side and ion-milled from both sides

The sputtering yield, defined as a ratio of the mean number of the emitted atoms to the flux of the incident particles depends on the energy of the incident particles, i. e., ions and neutrals; the angle of incidence of the sputtering beam θ, the relative masses of the specimen atoms and incident particles, the characteristics of the material as the mass and the cohesive energy of the sputtering target. Other factors influencing the sputtering yield are the specimen temperature, the concentration and chemical nature of any background gases, the crystallinity of the specimen, any chemical interactions occurring between the incident particles and the specimen, and specimen contamination. The ion-milling process has the effect of producing surface damage, i.e., amorphization. This effect is extremely undesirable when sputtering is used for the final thinning of the XTEM specimen. The presence of thick amorphous layer (7 - 10 nm) on the surface of the TEM specimen reduce the resolution of the TEM imaging. All above mentioned parameters have to be optimised in order to achieve a reasonable sputtering yield while causing minimum thickness of the amorphous layer on the surface of the specimen. The range of available accelerating voltage of Ar^+ ions amounts to ~ 0.1 – 10 keV (depending on the manufacturer), but the samples with the least damage are prepared at voltages lower than 4 keV. One of the widely used conventional ion-milling machine is the ”Duo Ion Mill 600” produced by GATAN Inc. In this machine ion-milling can be performed under milling angles in the range of 70° ÷ 80°. It was used for the preparation of a part of the Si specimens that were investigated in this work. The milling parameters for the Si substrates were: 4 keV Ar^+ ions, 1mA total current at incidence angles of θ = 73°, 75° and 77°. There are no references found in the literature which show that the ion milling performed in this machine introduces any modification of the real structure of the sample (including $R_P/2$ defects).

In recent years one can observe a trend to increase the milling angle θ in order to minimise the specimen surface damage. The new generation ion-milling system ”PIPS” by GATAN has the capability of increasing θ to values higher than 85°, in this way decreasing the amorphisation of the TEM specimen surface. Another advantage of the high-angle ion milling process is that the resulting wedge surrounding the perforation hole of the specimen consists of a larger area of interest thin enough to be observed by TEM compared to the corresponding area of the wedge achieved by milling performed under lower angle. Additionally to the ”Duo Ion Mill 600”, the high-angle ion-milling system used in this study is ”PIPS” by GATAN with the following parameters: 4 keV Ar^+ ions and 10 μA ion current at a milling angle $\theta = 86°$.

In order to increase the probability for TEM imaging of the $R_P/2$ defects, i.e. very small defect complexes, a special effort was made to improve the quality of the XTEM specimens in respect of decreasing the amorphous surface layer, and to avoid the use of any treatment during the XTEM sample preparation which can modify the defect structure needing to be investigated. As an alternative to the conventional XTEM specimen preparation by ion milling, the cleavage technique was used in the $R_P/2$ effect related studies reported in this thesis.

3.2.2 TEM specimen preparation by cleaving

Cleaving is a technique for producing cross-sectional TEM specimens of crystalline materials such as semiconductor substrates. "Cleaving" refers to the separation of a crystal along specific atomic planes. A small-angle cleavage technique for semiconductors and related materials was developed by McCaffrey [Caf91]. When sufficient stress is applied to a silicon crystal, it will typically cleave along a plane which requires the fewest bonds to be broken. The cleavage plane orientation for a [001] Si wafer is shown in Fig. 3.3. The (111) planes are the preferred cleavage planes in Si crystal as there is the lowest number of bonds, n, in these planes – $n_{(111)}$ = 7.83 bonds/nm^2 compared to the (110) planes – $n_{(110)}$ = 9.59 bonds/nm^2, and (120) planes – $n_{(120)}$ = 12.14 bonds/nm^2. However, in practice, the (110) planes are the standard cleavage planes in [001] silicon wafers because the (111) planes in a [001] wafer form an angle of 54.75° to the surface of the wafer shown in Fig. 3.3 (a). Because of this inclined configuration, the area of the (111) plane crossing the wafer with thickness x (respectively the number of bonds across the wafer along the (111) plane) increases by the factor of $f = 1/\sin(54.75°)$ times the wafer thickness x, or $f = 1.22x$. This gives for the (111) planes exactly the same number of bonds as for the (110) planes. In cleaving a [001] wafer, a scribe line is usually made along a (110) plane at the position where the sample is to be cleaved. The scribe line introduces damage to this plane and effectively makes the wafer thinner along this line. A cleave along this plane is then energetically favourable because it contains the fewest number of bonds. The small-angle cleavage technique requires the sample to be thinned from the back side to approximately 100 µm. The wafer thickness is optimised, taking into account that cleaving is more easily performed in a thinner wafer as the number of bonds needed to be broken is smaller, but the sample must be also mechanically stable. The wafer has to be cleaved along two planes which on one side have to be both perpendicular to the original surface of the wafer to achieve a XTEM specimen. On the other side these two planes have to form a small angle between each other that the resulting XTEM specimen will exibit a sharp tip being thin enough to be transparent for the electrons. The area of interest must be situated in the tip. For the [001] wafer, a suitable set of cleaving planes is (120) and (110). As shown in Fig. 3.3 (a), the (120) plane is perpendicular to the surface (001) plane but has more bonds than the standard (110) cleavage plane (as mentioned above). To allow the wafer to cleave along a (120) plane, a scribe line is first made along this plane on the back face of the wafer. As the total wafer sample thickness in the small-angle cleavage technique is approximately 100 μm, a scribe line more than 20 μm deep will create the situation where a cleave along this scribe line breaks the fewest number of bonds in the crystal. In practice, a scribe line of this depth is easily achieved, allowing the sample to cleave along a (120) plane.

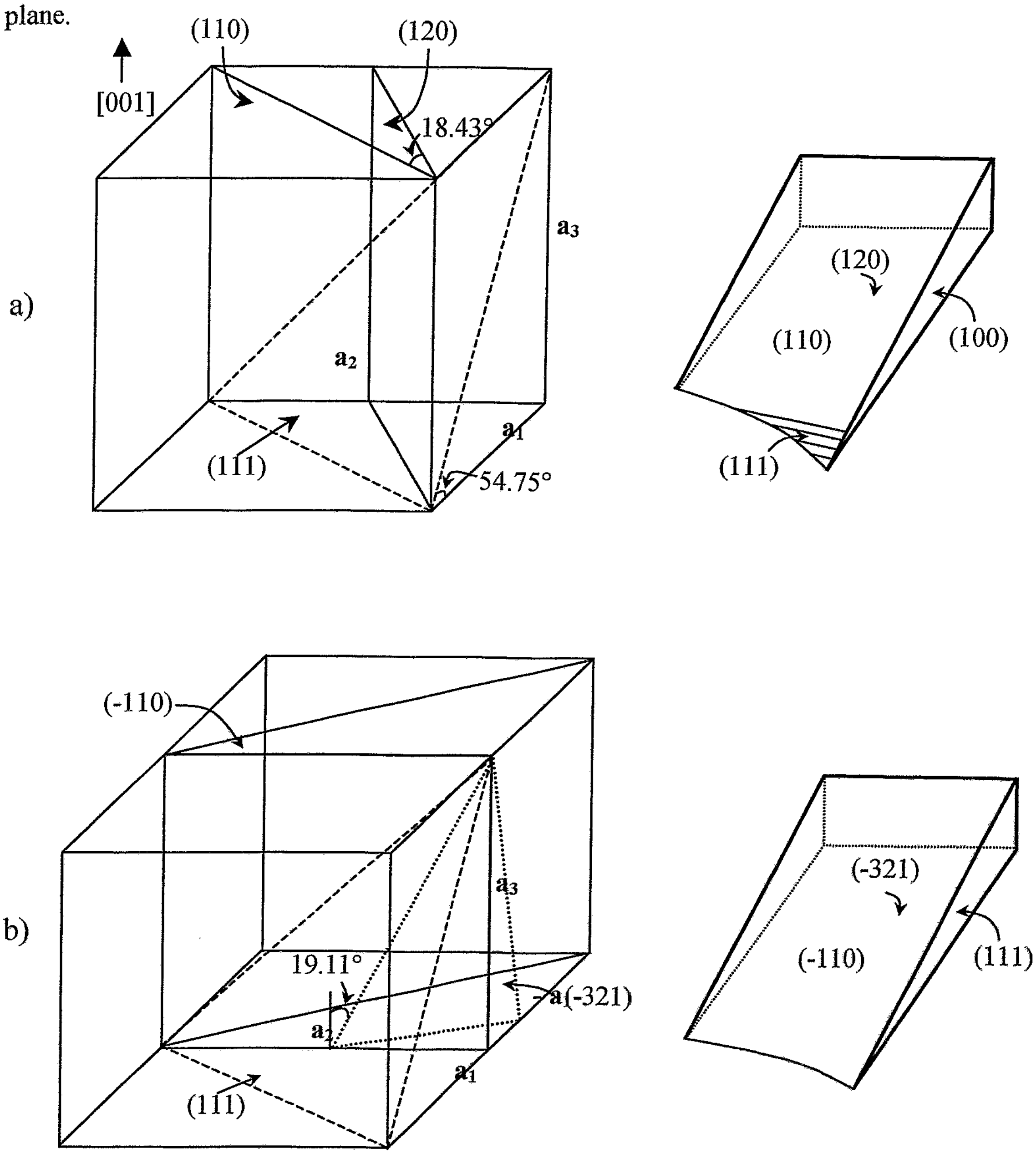

Fig. 3.3(a) Cleavage plane orientations for a [001] Si wafer (a) and for [111] wafer (b) together with a scheme of the resulting XTEM sample prepared by cleaving; $\mathbf{a}_1$, $\mathbf{a}_2$ and $\mathbf{a}_3$ are the vectors of the unit cell

A second cleave is then introduced from the front face of the wafer, and a scribe line is made along a (110) plane, avoiding scribing the wafer at the intersection of the (120) and (110) planes which will be the region of TEM investigation. The wafer will cleave along the (110) plane, except at the tip where the (120) and (110) planes intersect. There (shown in Fig. 3.3 (a)) as the cleaving approaches the intersection of these two planes, it reaches a point where the distance perpendicular to the (120) plane is less than 82% of the total thickness of the wafer. At this point there are fewer bonds along the (111) plane than the (110) plane and the wafer will finish to cleave along the (111) plane. This forms a tip bounded by the (100) surface plane, the (120) and (111) cleaved planes. The so prepared cross-section specimen has a wedge shape with a triangular needle tip. This thin wedge is mounted on a slot for TEM examination. For the case of [111] oriented wafer the set of the planes used for cleaving are (-110) and (-321). The plane orientations and the scheme of the resulting wedge are shown in Fig. 3.3(b).

The cleaving technique for TEM sample preparation provides automatically clean specimen surfaces. Therefore it was chosen to be employed in the presented study of TEM imaging of the $R_P/2$ defects. As the cleaved specimen is exposed in air, a thin, 1.0 – 1.5 nm layer of amorphous SiO_2 is spontaneously formed on the cleaved surface from exposure to air. This oxidation is the only source of amorphous layer of the surface, unlike in the ion milling sample preparation technique that can induce amorphisation and defect modification as discussed in 3.2.1. Micrographs from samples made by the small-angle cleavage technique are presented in this thesis, in its variations of cleaving [001] and [111] oriented Si wafers.

3.3 Secondary Ion Mass Spectrometry

In this work the SIMS depth profiles are used to detect metal and other impurities present in particular layers (R_P and $R_P/2$), their concentrations, and their depth distributions. The SIMS depth profiling measurements were performed on a Cameca IMS-5F instrument.

Bombardment of a sample surface with a primary ion beam followed by mass spectrometry of the emitted secondary ions constitutes SIMS. The impact of the primary ions generates neutral atoms and positively and negatively charged secondary ions, which are sputtered from the sample surface. Positive or negative ions can then be mass-separated and detected by an electron multiplier in order to measure their spatial distribution on the surface. The sputtering process removes material from the surface, constantly exposing new, previously buried, layers to analysis by the ion beam. Monitoring the intensity of secondary ions as a function of time provides a profile of elemental concentration as a function of depth. The sputter rates can be adjusted to analyse depths ranging from nanometers to many micrometers.

3.4 Ion beam analysis

3.4.1 Rutherford Backscattering Spectrometry

RBS is based on collisions between atomic nuclei and high energy ions. It involves measuring the number and energy of ions of a beam which backscatter after colliding with atoms in the near-surface region of a sample at which the beam has been targeted. A typically used RBS scattering geometry is shown in Fig. 3.4 a). When a sample is bombarded with a beam of high energy particles, the majority of particles are implanted into the material and do not escape. This is because the diameter of an atomic nucleus is on the order of 1×10^{-15} m while the spacing between nuclei is on the order of 2×10^{-10} m. A small fraction of the incident particles do undergo a direct collision with a nucleus of one of the atoms in the upper few micrometers of the sample. The interaction can be described as an elastic collision using classical physics. A particle will lose energy as the result of the collision. The collisional energy loss depends on the masses of the projectile and the target atoms. The ratio of the energy of the projectile before and after collision is the kinematic factor. The number of backscattering events that occur from a given element in a sample depend upon two factors: the concentration of the element and the effective size of its nucleus, its scattering cross section. The energy measured for a particle backscattering at a given angle depends upon two processes. The particles lose energy while they pass through the sample, both before and after the collision. The amount of energy lost is dependent on that material's stopping power.

For crystalline targets, channeling can occur. Channeling is the steering of a beam of energetic ions into open spaces (channels) between close-packed rows or planes of atoms in a crystal. The steering is the result of a correlated series of small-angle screened

Coulumb collisions between an ion and the atoms bordering the channel. Thus, channeled ions do not penetrate closer than the screening distance of the vibrating atomic nuclei, and the probability of large-angle Rutherford collisions is greatly reduced compared with the probability of such interactions from a non-channeled (random) beam of ions. Channeling results in surface peak and reduced sub-surface yield in the backscattering spectrum. The effect of crystalline imperfections (point defects, dislocations) on channeling can be used to detect their presence in the crystal. Channeling atoms are gradually deflected out of channels (dechanneled) by multiple scattering with the displaced atoms resulting in an enhanced backscattering yield in the RBS spectrum. This technique was used in the presented studies to detect the damage caused in the silicon crystal by He^+ ion implantation discussed in details in Chapter 4.2. The depth distribution of the displaced silicon atoms was analysed by Rutherford Backscattering/channeling spectrometry (RBS/C) with a 1.2 MeV He^+ beam aligned to the (100) crystal direction. The detector was placed at 28° with respect to the beam direction.

More can be read about the principles of RBS and channeling in the book of Chu at. al [Chu78].

3.4.2 Elastic Recoil Detection Analysis

For the ERDA-method the samples are irradiated with highly energetic heavy ions under grazing conditions. The energy as well as the number of the outscattered atoms (recoils) of the sample components are measured at a fixed angle relative to the beam direction (see Fig. 3.4 b). ERDA, like RBS, depends on the following physical concepts: 1) The kinematic factor describes the energy transfer from a projectile to a target nucleus in elastic two-body collisions; 2) The differential scattering cross section gives the probability for the scattering event to occur, 3) The stopping powers give the average energy loss of the projectile and the recoiled target atom as they traverse the sample (thereby giving a method for establishing a depth scale). By applying these physical concepts, the elastic recoil spectrum can be transformed into a quantitative concentration profile as a function of depth.

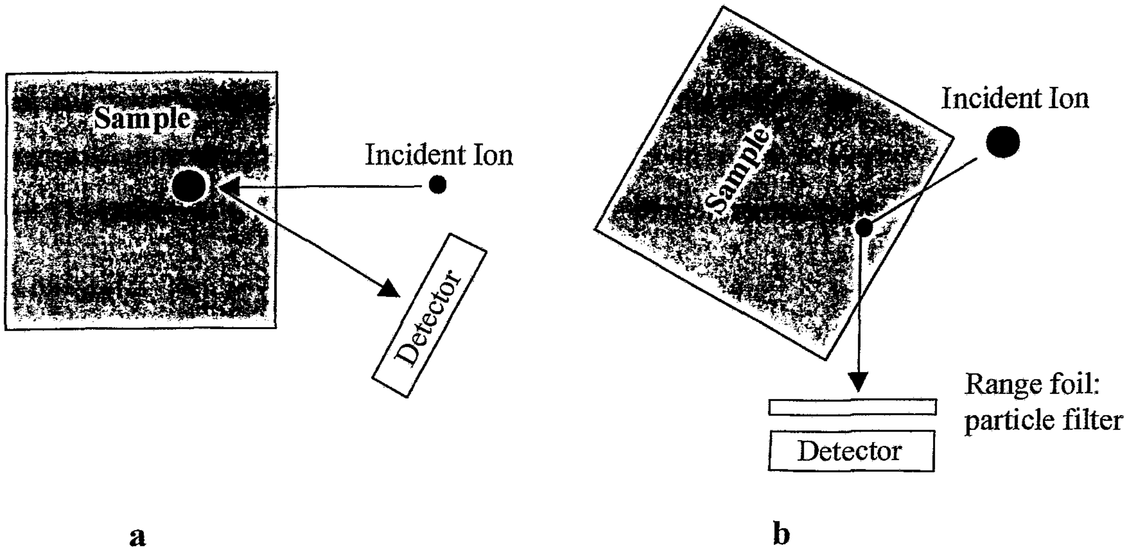

Fig. 3.4 A schematic geometry of Rutherford backscattering spectrometry (RBS) (a) and Elastic Recoil Detection Analyses (ERDA) (b)

In the presented study the distribution of the He content in Si was investigated by ERDA technique, using a 10 MeV C^{4+} beam. The samples were tilted 73.5° and the detector placed at 28° with respect to the beam direction.

3.5 X-ray diffraction

The technique of x-ray diffraction is used for structural characterisation of solids, to determine crystal structures, orientation, strain, film thickness, grain size etc. It is a non-contact and non-destructive technique, convenient to apply in many cases since no sample preparation is needed. The basic features of an XRD experiment is shown in Fig 3.5. A monochromatic beam of x rays is incident to a sample, containing crystallites with lattice planes separated by a distance *d*. A detector is placed at an angle 2θ from the direction of the incident x rays, and the diffracted intensities are measured as a function of 2θ. The measured diffraction pattern is a picture of the reciprocal space of the sample, and thus depends on orientations and separations of the lattice planes in the sample. All the atomic planes will scatter x rays, but through interference phenomena between the x rays, diffracted intensities will only appear in certain directions, i.e., for certain 2θ values. The conditions for such constructive interference is given by Bragg's law, $\lambda = 2\, d_{hkl}\sin(2\theta_{hkl}/2)$, where $2\theta_{hkl}$ is the angle in which direction the planes (*hkl*) (with plane distance d_{hkl}) diffract x rays with the wavelength λ. If the angle ω between the incident x rays and the sample surface is equal to θ_{hkl}, as in Fig 3.5, then only planes parallel to the sample surface will generate diffraction intensities into the detector, during a so called θ-2θ scan.

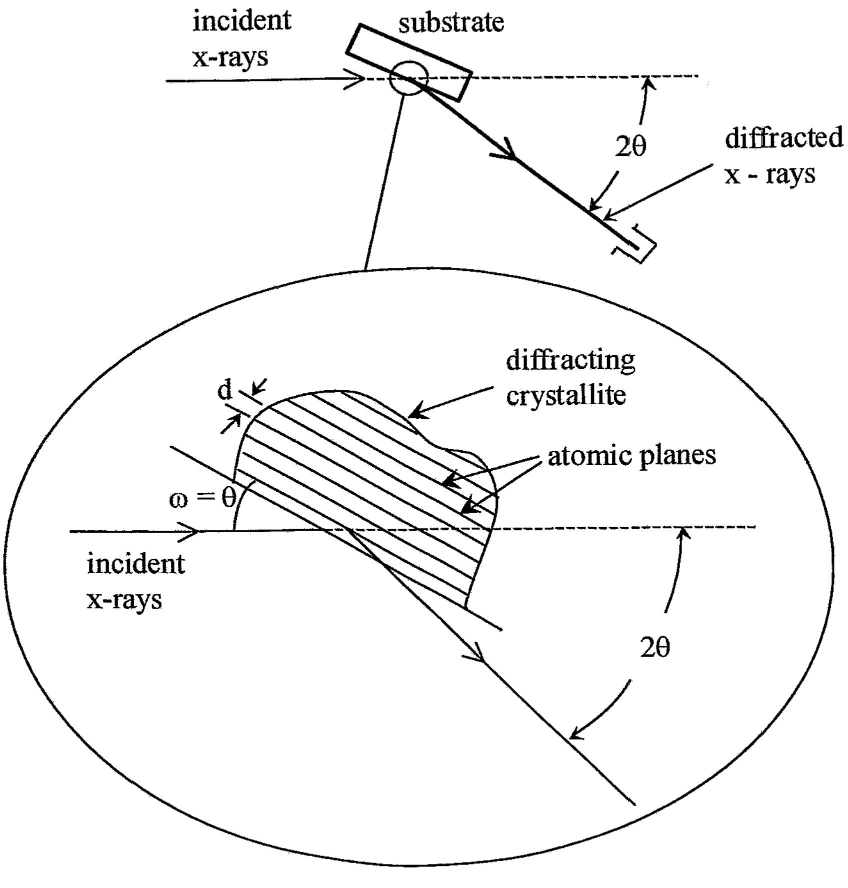

Fig.3.5 Basic features of an x-ray diffraction experiment.

In the work present in this thesis, the XRD analyses were performed using the θ-2θ scan on the (004) Si reflection. Further, rocking curve analysis is made. An X-ray rocking curve is an angular reflectivity plot used for analysing the structure and composition of crystal lattices.

Chapter 4

Results

4.1 MeV Si^+ ion implanted silicon

The results from the literature discussed in Chapter 2, are consistent in finding that it is hard to directly observe the defect structure at $R_P/2$ by means of TEM, as the defect sizes are probably smaller than the resolution of the performed TEM analyses. The following two subchapters are focused on the crucial importance of the TEM specimen sample preparation technique in the study of the structure of the $R_P/2$ defects.

4.1.1 $R_P/2$ defects investigated in TEM specimens prepared by ion-milling

It will be demonstrated that the conventional ion milling process introduces structural modification of the original $R_P/2$ defect structure. This feature in turn could indicate, as will be argued below, that interstitial type defects are present at the $R_P/2$ damage layer.

The $R_P/2$ defects were formed by 3.5 MeV, 5×10^{15} at/cm^2 Si^+ implantation and subsequent annealing at 850-900°C thermal treatment in an Ar atmosphere for duration between 30 s and 1 h using furnace annealing or RTA. The substrates were <100>-oriented n-type CZ-Si , <111>-oriented p-type FZ-Si wafers and <100>-oriented p-type Epi-Si layers. One part of the samples were implanted with 20 keV Cu^+ ions at a fluence of 3×10^{13} cm^{-2} on the rear face, either before or after the damage annealing. The redistribution of Cu throughout the sample bulk has been performed either simultaneously with the damage annealing or subsequently by an additional thermal treatment at 700°C for 5 min. The other part of the samples was annealed without being implanted with Cu.

The Cu implanted samples were analysed by SIMS to determine the resulting Cu distribution in order to confirm the existence of the $R_P/2$ defects after the above mentioned implantation and annealing. The microstructure of the residual defects after annealing was investigated by XTEM in all samples (with and without Cu). The TEM specimens were prepared under low milling angle $\theta = 77°$ using the Gatan Duo Mill 600 or under high milling angle $\theta = 86°$ using the Gatan PIPS system as described in Chapter 3.2.1.

Fig. 4.1 shows a set of cross-section TEM bright-field micrographs of a Si-self-ion implanted p-type FZ-Si sample contaminated with Cu and annealed at 850°C for 1 h. The TEM micrographs are compared with the corresponding Cu depth profile (Fig. 4.1 a) measured by SIMS. In all TEM micrographs (Fig. 4.1 b, c, and d) a well-defined band of extended dislocations can be seen which have been formed around R_P. At the depth of the gettering band around $R_P/2$ (Fig. 4.1 a), no defects have been observed in the sample milled under $\theta = 86°$ (Fig. 4.1 d). This result is in agreement with previous published results [Tam91, Kög96, Kon97, Bro98, Kov98a, Kov98b]. In contrast, a well defined band of defects around $R_P/2$ has been observed in the specimen thinned by ion-milling at an angle of $\theta = 77°$ (Fig. 4.1b) $\theta = 75°$ (Fig. 4.1c), c and $\theta = 73°$ (not shown). The defects at $R_P/2$ are observable when the milling conditions for sample preparation are appropriate. However, the defects detected at $R_P/2$ are surprisingly not of vacancy type. The defects at $R_P/2$ are interstitial-type loop-like planar defects on (111) planes. Their interstitial character has been determined by the diffraction contrast technique following the experimental procedure described in details by Edington [Edin76]. The technique includes:

(1) imaging of the loops in both bright field (BF) and dark-field (DF) under dynamical two-beam conditions so that the dynamical theory can be qualitatively applied. In this work the 220 beam dynamic conditions were used (see Fig. 4.2).

(2) determination of the reflecting plane vector ***g*** from the diffraction pattern images in both DF and BF conditions (Fig. 4.2 the inserts);

(3) A vector ***l*** is defined as joining the black to the white lobe of the loop (marked with an arrow on the inserts in Fig. 4.2). The directions of ***g*** and ***l*** are compared.

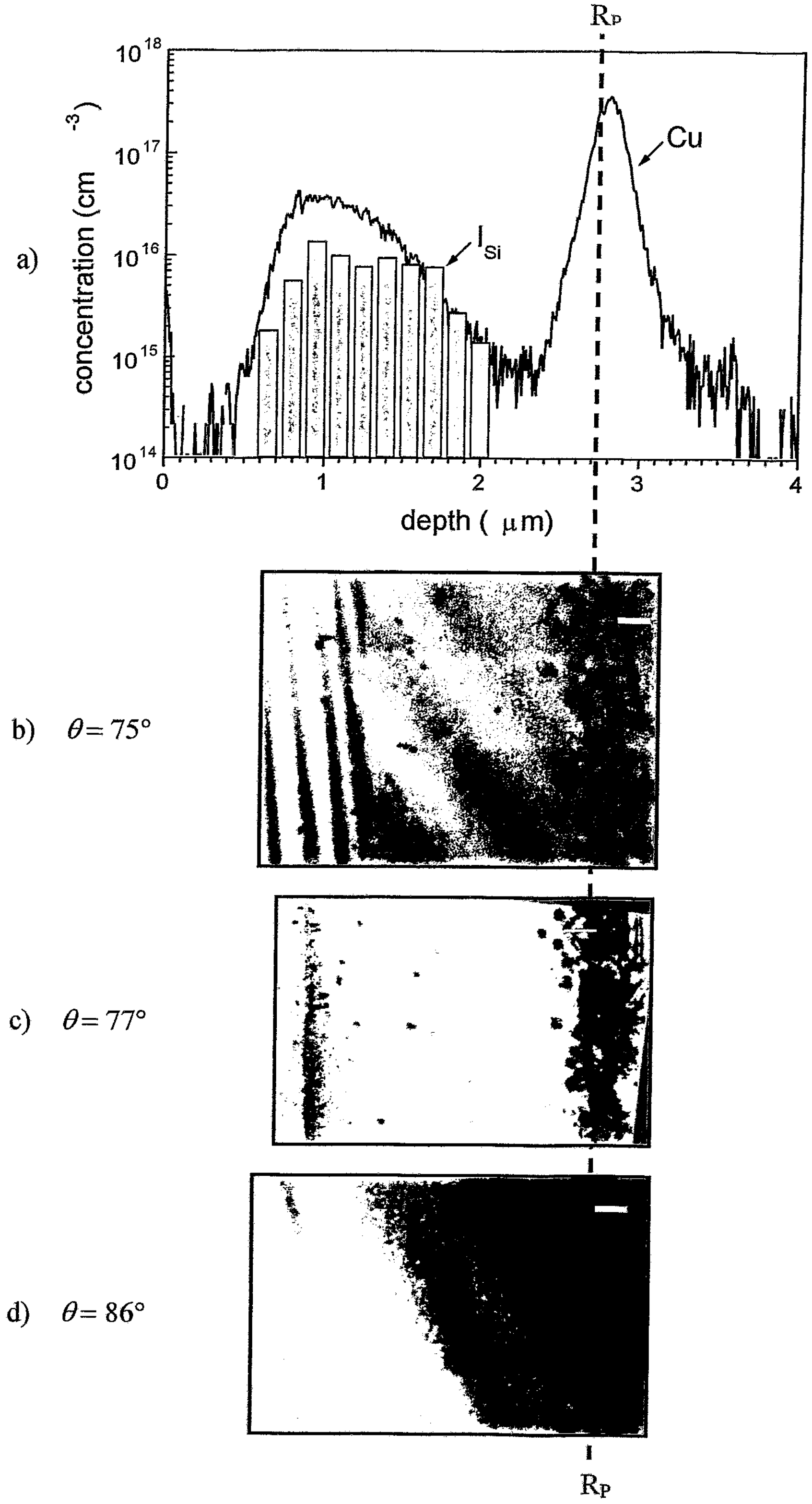

Fig. 4.1 a) SIMS Cu depth profile for 3.5 MeV, 5×10^{15} Si^+cm^{-2} implanted FZ-Si (111) contaminated by $3\times10^{13}Cu^+cm^{-2}$ after furnace anneal of 850°C/1h correlated with the concentration of self-interstitials bound in loops, I_{Si}, (bars). I_{Si} was calculated from the TEM images obtained for samples prepared under $\theta = 77°$; (b, c, d) XTEM bright-field micrographs for the corresponding sample prepared under $\theta = 75°$, 77° and 86°, respectively.
The bar in the micrographs corresponds to 200 nm.

The depth position of R_P is indicated (resulting from TRIM). The same sample shows defects at $R_P/2$ for low θ of 75° and 77° or no defects at $R_P/2$ for high θ of 86°.

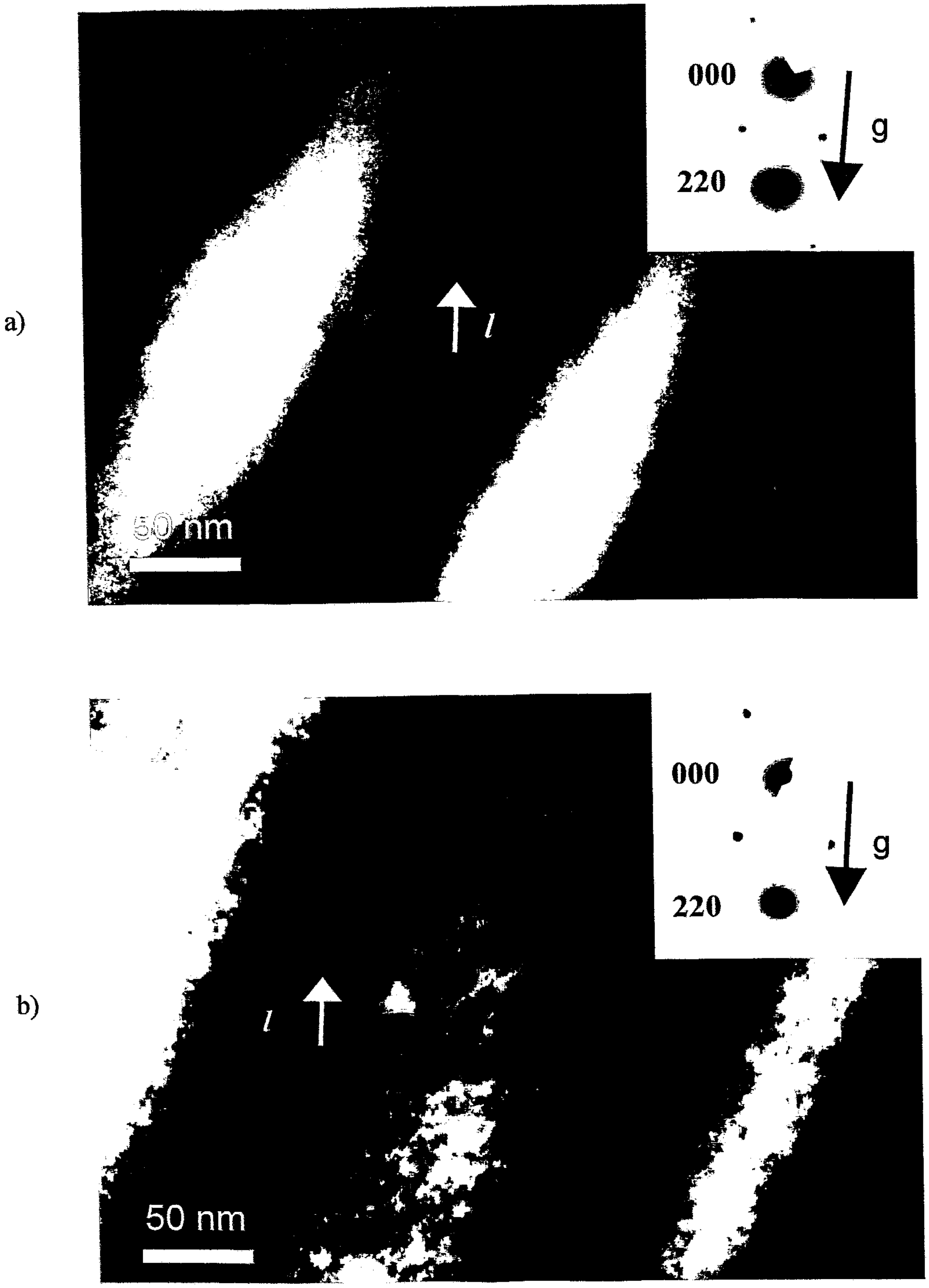

Fig. 4.2 (a) XTEM bright field (a) and dark-field (b) micrograph of the ion-milling induced defect at $R_P/2$. The sample is the same as in Fig. 4.1 . The inserts shows the diffraction pattern (dynamic (220) beam case), ***g*** - the reflective plane vector.

(4) For a given type of loop, that is vacancy or interstitial, the black/white contrast in relation to ***g*** depends on the depth of the loop. The TEM specimen can be divided into three layers at the top and bottom surface corresponding to depths of $0.25\xi_g$, $0.35\text{-}0.7\xi_g$ and $0.8\text{-}1.25\xi_g$ where ξ_g is the extinction length of the microscope for the actual ***g***. The depth of the loops visible at $R_P/2$ is estimated to be about 10 nm, taking into account the TRIM calculations of the damage caused by the Ar^+- sputtering beam (discussed in details below). The extinction length for the microscope operated at 300 kV in the (220) beam case, is 53 nm. Hence the loops investigated in this study are located in the layer with thickness of $0.25\xi_g$. Referring to [Edin76], for an interstitial loop, ***g*** and ***l*** point in the opposite approximate direction in this layer in BF conditions as well as in the DF conditions (Fig. 4.2). If the loops had vacancy character the situation would be reversed, i.e. ***g*** and ***l*** would have the same direction in BF and DF conditions. The last case (vacancy character) was never observed.

Fig. 4.3 shows another example for generation of ion-milling induced defects in the samples showing at $R_P/2$ a gettering effect. The samples were RTA annealed at 900°C for 180s. The SIMS analysis (Fig. 4.3 a) shows that the $R_P/2$ layer is narrower than the one presented in Fig. 4.1 (a). In this case the band of the ion-milling induced interstitial loops (shown in Fig. 4.3 b) is also narrower than the one shown in Fig. 4.1 b) and it mirrors the depth distribution of the metal around $R_P/2$. Moreover, interstitial loops were observed in the $R_P/2$ region of the sample implanted and annealed under the same conditions but not contaminated with Cu (Fig. 4.3 c). The defects around $R_P/2$ appear exactly at the same depth as in the sample contaminated with Cu (Fig. 4.3b). This means that the presence of Cu plays no important role in the formation of the defects during milling which were observed in $R_P/2$ region.

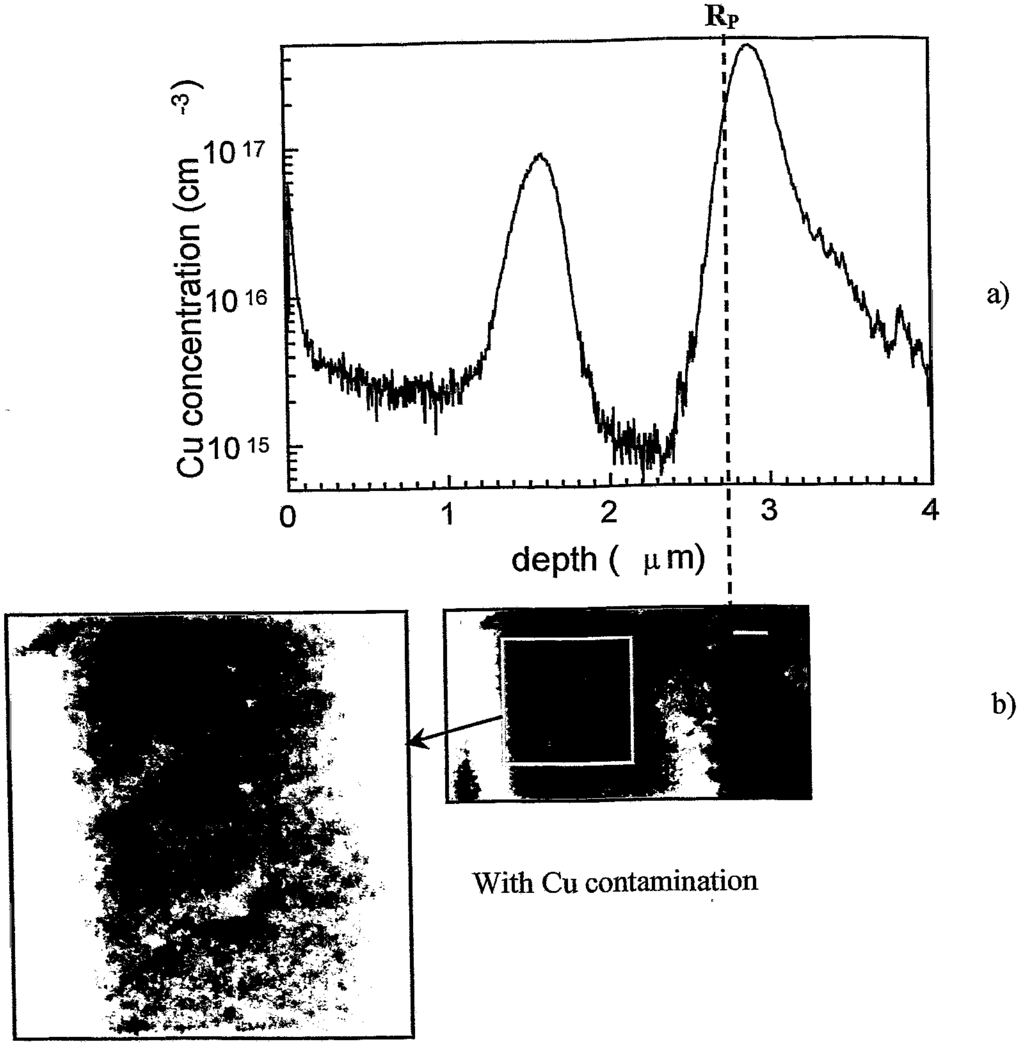

With Cu contamination

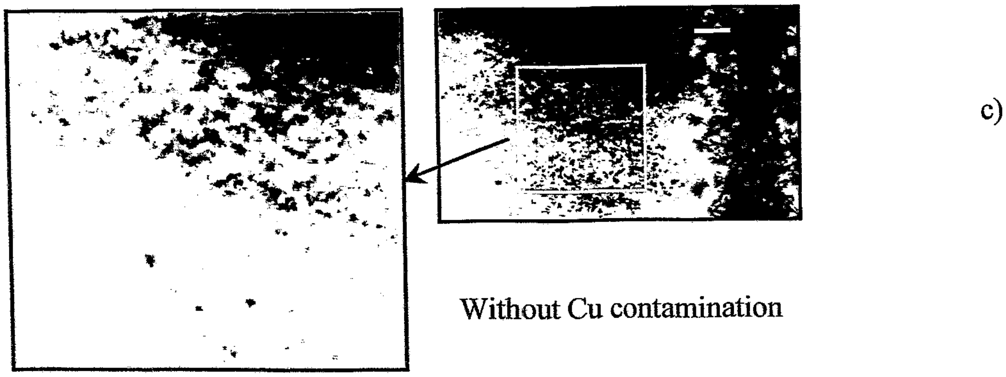

Without Cu contamination

Fig.4.3 (a)SIMS Cu depth profile for 3.5 MeV, 5×10^{15} $Si^{+}cm^{-2}$ implanted Cz-Si(100) contaminated by 3×10^{13} $Cu^{+}cm^{-2}$ after RTA at 900°C for 180s; (b) XTEM bright field micrographs for the same sample as in (a); (c) XTEM bright field micrographs for the sample which is the same as in (a) but not contaminated with Cu. The incident milling angle is 77°. The bar in the micrographs corresponds to 200 nm. Fig. 4.3(b) and (c) are adjusted to the depth scale of Fig.4.3 (a).

4.1.1.1 Model for self-interstitial injection into Si during ion milling

It is important to know the mechanisms by which surface structure develops during ion milling and the nature of the radiation damage. Ion milling produces an amorphous surface layer (AL) on the crystalline Si target. The following experiment has been performed to investigate the damage production during ion-milling. A set of Ar^+ bombardments into Cz-Si (100) substrates was performed in order to measure the thickness of the AL versus the milling angle θ with respect to the sample surface. The Ar^+ sputtering was performed by using a 6 keV Ar^+ beam with a nominal beam current of 20 μA at room temperature. The thickness of the AL was measured by XTEM imaging. The XTEM specimens were prepared under the milling angle $\theta = 86°$ using the Gatan PIPS milling system. The thickness x of the AL has been measured from the cross-section TEM image and it follows the empirical rule $x = R_p+2\Delta R_p$, where R_p and ΔR_p are the mean projected Ar^+ range and range straggling calculated via the TRIM(95) code (see Fig. 4.4).

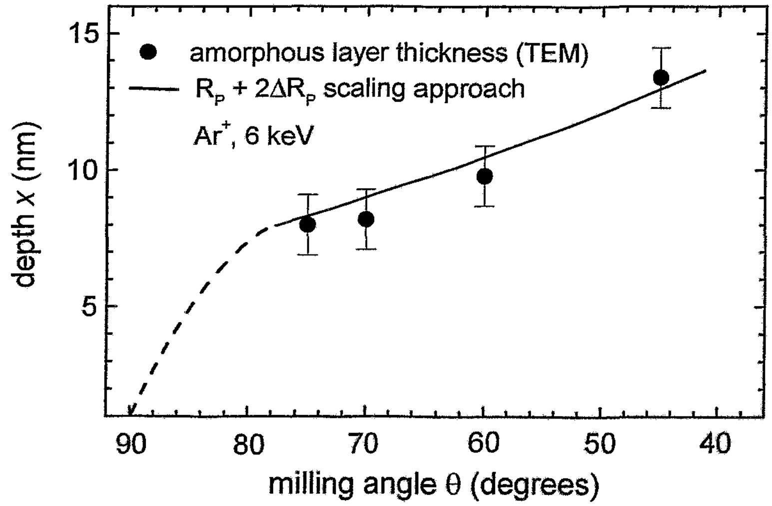

Fig. 4.4 Thickness of the amorphous surface layer versus the milling angle θ for Ar bombardment at 6 keV. The continuous line represents the $R_p+2\Delta R_p$ empirical scaling obtained using the Ar range predictions from the TRIM code.

Using the empirical $R_p+2\Delta R_p$ scaling, the amount of recoiled Si atoms distributed in the crystalline part of a 4 keV Ar^+ irradiated Si has been estimated. Fig. 4.5 illustrates the concentration N of the Si recoils versus the depth, predicted by TRIM(95), considering the case of a 4 keV Ar^+ beam and $\theta = 75°$. The thickness of the amorphous layer according to the $R_p+2\Delta R_p$ rule is 6 nm. The areal density of the Si recoils in the amorphous layer is

$$N_{amorph} = \int_0^{R_P+2\Delta R_P} N dx$$

The concentration of the Si recoils injected into the crystalline part of the target can be calculated to be:

$$N_c = \int_{R_P+2\Delta R_P}^{\infty} N dx$$

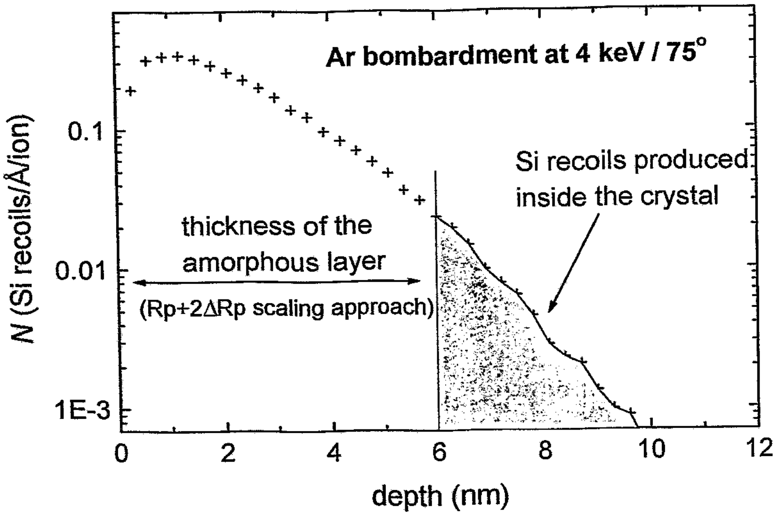

Fig. 4.5 The concentration N of the Si recoils generated in the Si target during the Ar bombardment at 4 keV and $\theta = 75°$ as a function of depth. The shaded area is proportional to the amount of Si recoils produced inside the crystalline part of the sample.

Fig. 4.6 shows the results of the above calculations, expressed in terms of the number of Si atoms (I_{Si}) injected into the crystal per incident Ar^+ ion (i.e. I_{Si}/Ar^+ injection rate). The maximum of the injection rate achieves a value of about 0.8 and occurs for an incidence angle $\theta \approx 75°$. The injection rate decreases with decreasing θ ($\theta < 75°$) because the thickness of the amorphous layer increases faster than the maximum depth of the Si recoils. On the other hand, for $\theta > 75°$, the decrease of the injection rate with increasing θ is a consequence of a faster reduction of the Si recoil range as compared to the AL thickness.

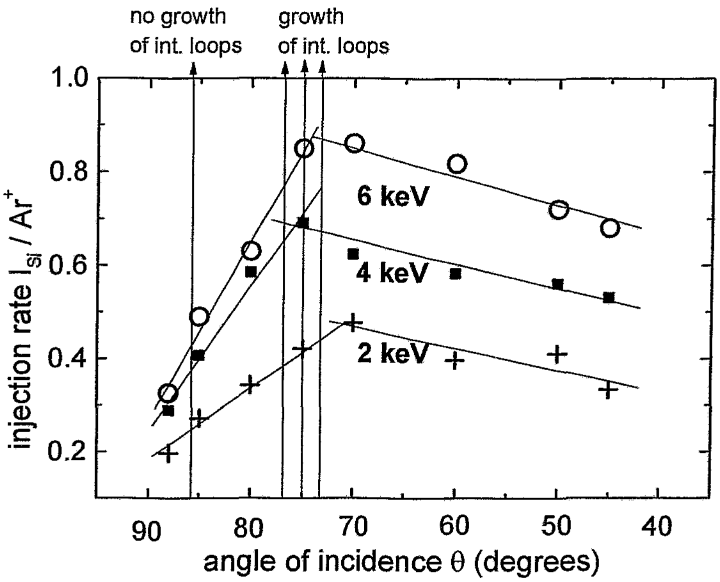

Fig. 4.6 Rate of Si self-interstitial atoms produced inside the crystalline part of the sample per incident Ar^+ ion. Continuous lines are fitted to guide the eyes through the calculated points.

A similar effect of a self-interstitial injection into Si has been recently reported in the case of SIMS profiling [Car98]. The authors found that Si interstitials, rather than vacancies, are preferentially injected inside the Si substrate during the sputtering process which is part of the SIMS technique. The injection of interstitials inside the Si target during sputtering was proven by the broadening found for the boron (interstitial diffuser) delta doped layers, epitaxially-grown in Si substrate, while such broadening was not found for the antimony (vacancy diffuser) doped layers.

The incidence angle of the Ar^+ ions is found to be the crucial parameter for the occurrence of TEM-visible defects at $R_P/2$. The high milling angle $\theta = 86°$ (Fig. 4.1e) allows only very small number of Si recoils to penetrate within the specimen. The use of a lower sputtering angle increases the number of the Si recoils injected into the TEM specimen. These preparation-induced self-interstitials may interact with the defects at $R_P/2$ which are gettering centres for metals and form observable interstitial loops during ion milling. Therefore, the loop depth distribution reflects the existence of small, TEM-unobservable defects at about $R_P/2$ caused by the MeV Si^+ ion implantation.

4.1.1.2 Interstitial type defects in the $R_P/2$ region

It has been shown in 4.1.1 that the defects observed in the $R_P/2$ region are of interstitial type. These defects form during ion milling by interstitial injection as discussed in Chapter 4.1.1.1.

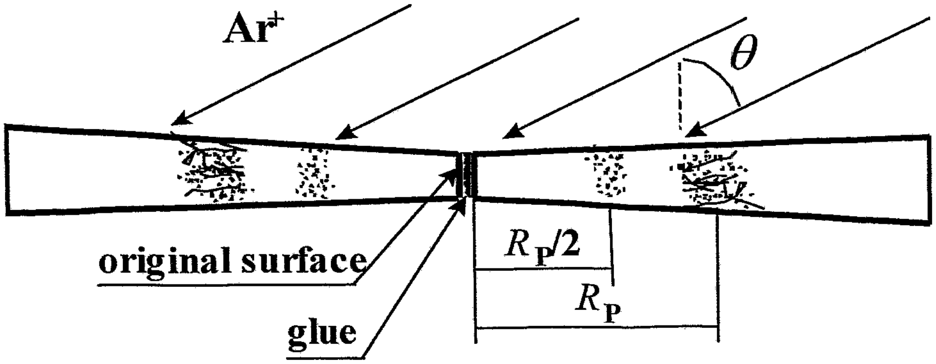

Fig. 4.7 A schematic of a XTEM specimen of a sample showing $R_P/2$ effect, θ milling angle. Defects around $R_P/2$ are observed by TEM after a conventional ion milling procedure.

During the ion milling process the whole surface of the specimen is bombarded by the Ar^+ ions (as shown in Fig. 4.7). It should be noticed that micrographs for unimplanted samples (not shown), milled under the same conditions as described above, do not show any defects at the $R_P/2$ region. This means that Ar^+ ions cannot trigger any defect formation without the previous existence of nucleation centres therein. The ion-milling induced defects are created only on the depth where the $R_P/2$ gettering is found in terms of metal gettering. This feature is demonstrated in Fig. 4.1 (a) where the concentration of interstitials bonded in loops at the $R_P/2$ region determined from Fig. 4.1 b is shown as bars together with the Cu distribution. The determination of the numbers of the Si interstitials bonded in loops has been carried out taking into account the depth distribution and size of the loops observed in the $R_P/2$ region. The thickness of the XTEM specimen in the $R_P/2$ region was estimated by counting the thickness fringes in the TEM image. The image was taken in two-beam dynamical conditions. The thickness fringes determine the areas with difference in thickness equal to the extinction length ξ_g of the microscope. The 220 two-beam excitation mode was used with $\xi_g = 53$ nm.

The geometry of XTEM specimen (discussed in Chapter 3.2.1) and the milling equipment does not allow exact measurement of the specimen temperature. One can estimate that during the bombardment of the Ar^+ ion beam the area of the TEM specimen around the perforation has elevated temperature. This elevated temperature is certainly high enough to enhance the mobility of the self-interstitials and trigger the defect creation during milling. It should be emphasised that the loops visible in the micrographs of Figs. 4.1 and 4.3 around the $R_P/2$ region are not the gettering centres for the Cu atoms because their appearance depends on the XTEM specimen preparation. However, the formation of interstitial loops can be taken as an evidence for the presence of nucleation centres for the formation of these loops. A question arises as to what are the nucleation sites of the formed interstitial loops. The oxygen and impurity contents do not play a major role in the formation of the defects during ion milling process as the defects were observed at $R_P/2$ for FZ (poor in oxygen), CZ (rich in oxygen) and Epi-Si (containing distinctly less impurities O, C than Cz-Si). The speculation for the existence of small interstitial clusters after annealing at the temperatures used in this study is consistent with the literature. Especially the clusters consisting 4 or 8 interstitials were found to be very stable under high temperature treatment (~ 800°C) [Cow99]. It is more likely that small interstitial clusters rather than the excess vacancies are the origin forming those interstitial loops. The transformation of self-interstitial clusters via rod like {113} defects to interstitial loops has been clearly demonstrated [Ben97,Cof00, Rob00]. To my knowledge there is no experimental evidence for a process which transforms vacancy-type defects to interstitial-type ones.

The possibility of existence of small interstitial clusters at $R_P/2$, discussed in this chapter, can be related also to the idea of incomplete local vacancy-interstitial recombination discussed in Chapter 2.

4.1.1.3 Other defects introduced by Ar^+ ion milling

The highly magnified images of the ion-milled Si specimen reveal specific contrast at overfocus and undefocus conditions. This contrast is pronounced in the thinnest part of the specimen, around the edge of the perforation. Fig. 4.8 presents underfocused BF image of a specimen revealing such ion-milling induced contrast. The through focus imaging of the specimen (discussed in Chapter 3.2) shows that the defects indicated by arrows on Fig. 4.8 could be nanocavities. The diameter of this cavities varies between 1 and 5 nm. The sample was milled using the high angle ion milling with $\theta = 86°$ which produces minimum damage on the surface as discussed in Chapter 3.2.1. One can clearly see from the image the artificial character of these defects. The cavities are found to form a layer, which strictly follows the edge of the hole perforated by the milling independent of the depth position in the sample. The area around the edge of the specimen where the cavities are found is the thinnest area of the wedge shaped XTEM specimen. During the Ar^+ bombardment this area reaches the highest temperature. The high local temperature of the specimen during ion milling process could be the main factor responsible for the formation of the cavities. The temperature increase favours the agglomeration of Ar to cavities. The hypotheses of formation of cavities in the above conditions are consistent with the literature. A similar effect was observed for the case of Ar^+-ion-beam etching of crystalline Si [Saw90]. The authors reported on formation of cavities in the surface layer of the etched and annealed samples. The Ar^+ beam induced cavities were found to appear in Cz, Fz and Epi- Si which means that their appearance is not oxygen or impurity related.

The roughness of the surface of the milled specimen and the amorphous layer created during milling also can contribute to the imaging contrast and can produce qualitatively similar images.

The presence of ion-milling induced cavities in the perforated edge region of the XTEM specimen has to be taken into account for the observation of the samples when the original defect structure, which needed to be investigated, consists of voids. Such a defect structure will be discussed in Chapter 4.2.

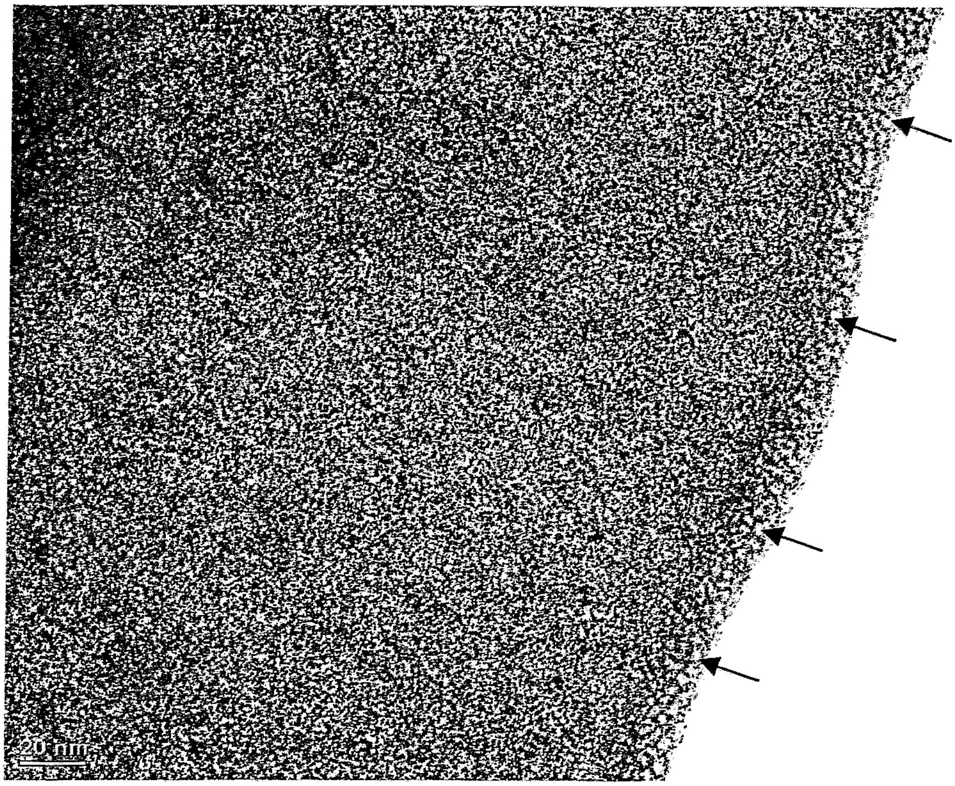

Fig. 4.8 Large magnified XTEM bright field micrographs for 3.5 MeV, 5×10^{15} $Si^{+}cm^{-2}$ implanted Epi-Si (100) after FA at 850°C for 30 min. Underfocused, kinematical conditions. The area close to the perforated by the ion milling hole reveals Ar^{+} bombardment induced cavities. Several cavities are indicated by arrows.

4.1.2 $R_P/2$ defects investigated in TEM specimens prepared by cleaving

Fig. 4.9 shows a bright field TEM micrograph of a cleaved specimen of a sample which is the same as the one shown in Fig. 4.1. The image is taken under dynamical (220) beam conditions in order to visualise the thickness fringes which reveal areas of equal thickness. The thickness fringes show that the XTEM specimen wedge is with uniform thickness in the direction perpendicular to the original surface. In the particular study of $R_P/2$ defects such a geometry is very suitable as it allows scanning the whole depth from the original sample surface to the R_P layer at equal high magnification conditions and searching for small defects in the thinnest part of the specimen. For such defects to be visualised by the TEM analyses, the specimen must be thin enough (with a thickness less than 100 nm), as it is for the well-prepared cleaved specimen. In contrast, the ion-milling prepared specimens (see Fig. 4.1 b) do not contain area with equal thickness perpendicular to the original surface but the one parallel to it.

A careful investigation of the thinnest area from the original surface to the R_P layer reveals small cavities in the $R_P/2$ region. Fig. 4.10 presents highly magnified BF kinematical TEM images of the area marked with a dotted square in Fig. 4.9.

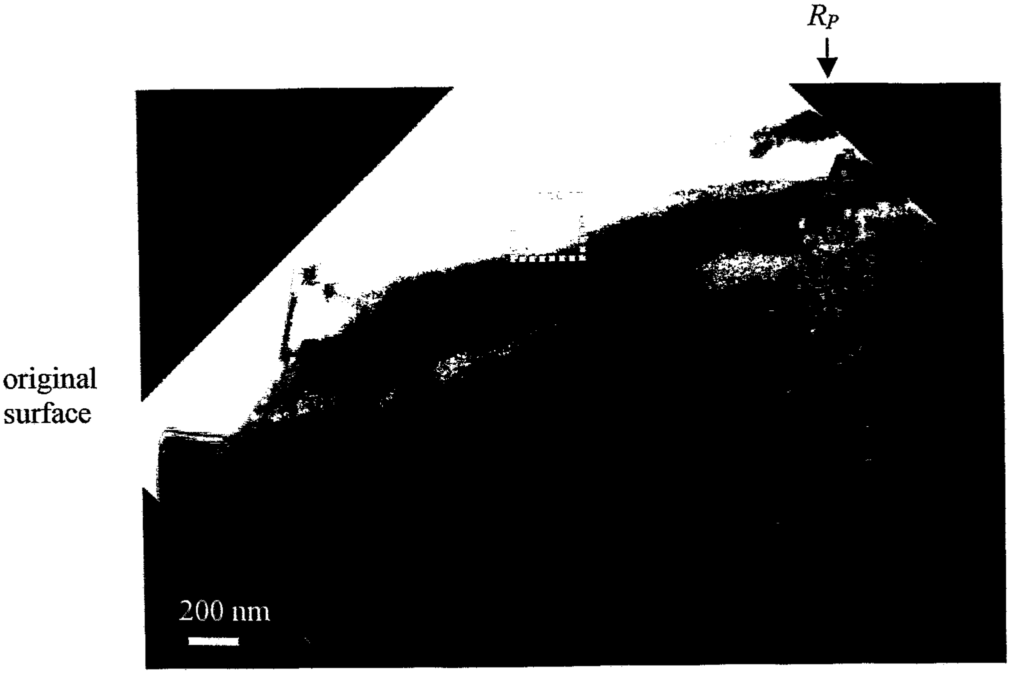

Fig. 4.9 XTEM bright field micrographs for 3.5 MeV, 5×10^{15} Si^+cm^{-2} implanted FZ-Si(111) contaminated by 3×10^{13} Cu^+cm^{-2} after furnace anneal of 850°C/1h. Dynamical (220) beam conditions. The R_P defect layer is visible. The marked area is shown under higher magnification conditions in Fig. 4.10.

The vacancy type character of the defects at $R_P/2$ was proved by the through focus imaging technique (explained in detail in 3.2). They appear darker than the background under overfocus conditions with a light fringe around (see Fig. 4.10 a). A similar degree of underfocus results in an image in which these contrast is reversed (see Fig. 4.10 b). The cavities are with the mean diameter of 3.5 nm. They appear in a depth corresponding to the $R_P/2$ gettering peak shown in (Fig. 4.1 a). Such cavities were invisible in TEM specimens prepared by ion milling.

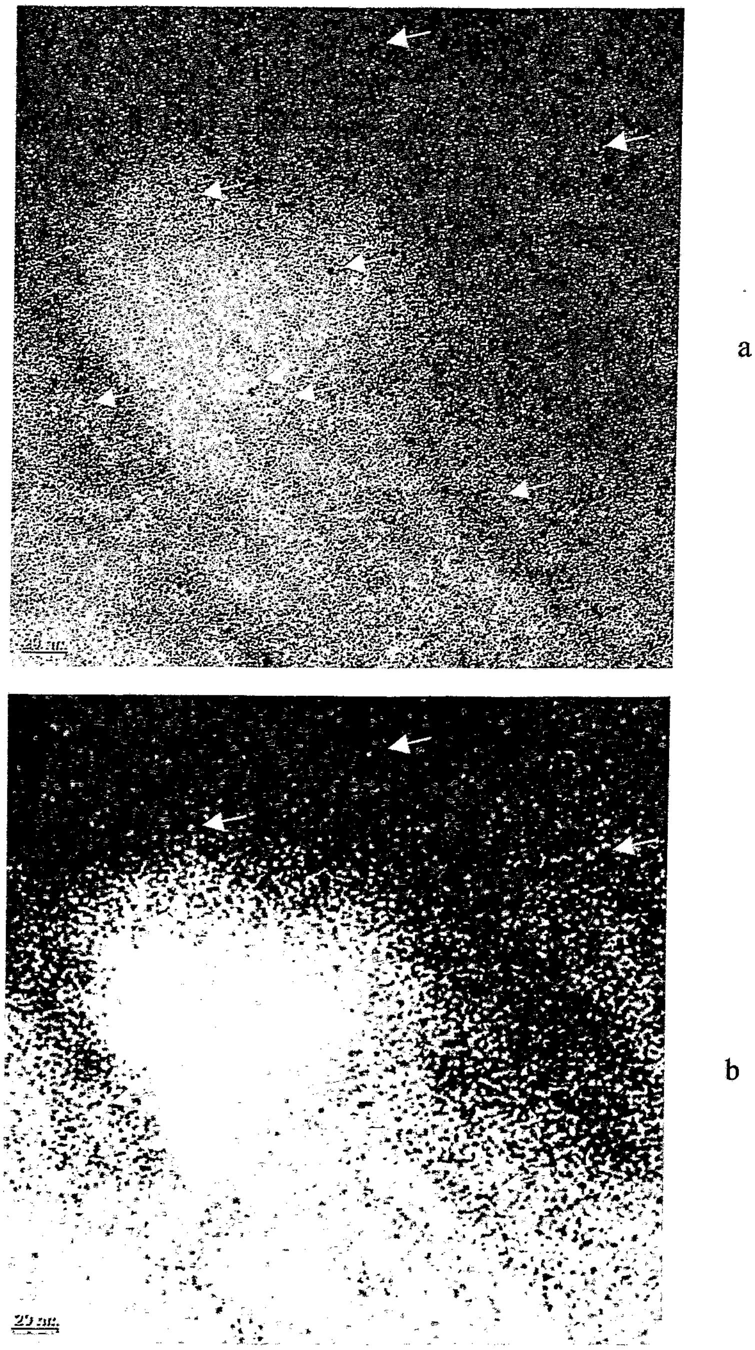

Fig. 4.10 XTEM bright field micrographs for 3.5 MeV, 5×10^{15} $Si^{+}cm^{-2}$ implanted FZ-Si (111) contaminated by 3×10^{13} $Cu^{+}cm^{-2}$ after furnace anneal of 850°C/1h; kinematical conditions, (a) overfocus; (b) underfocus ; the cavities are indicated with arrows.

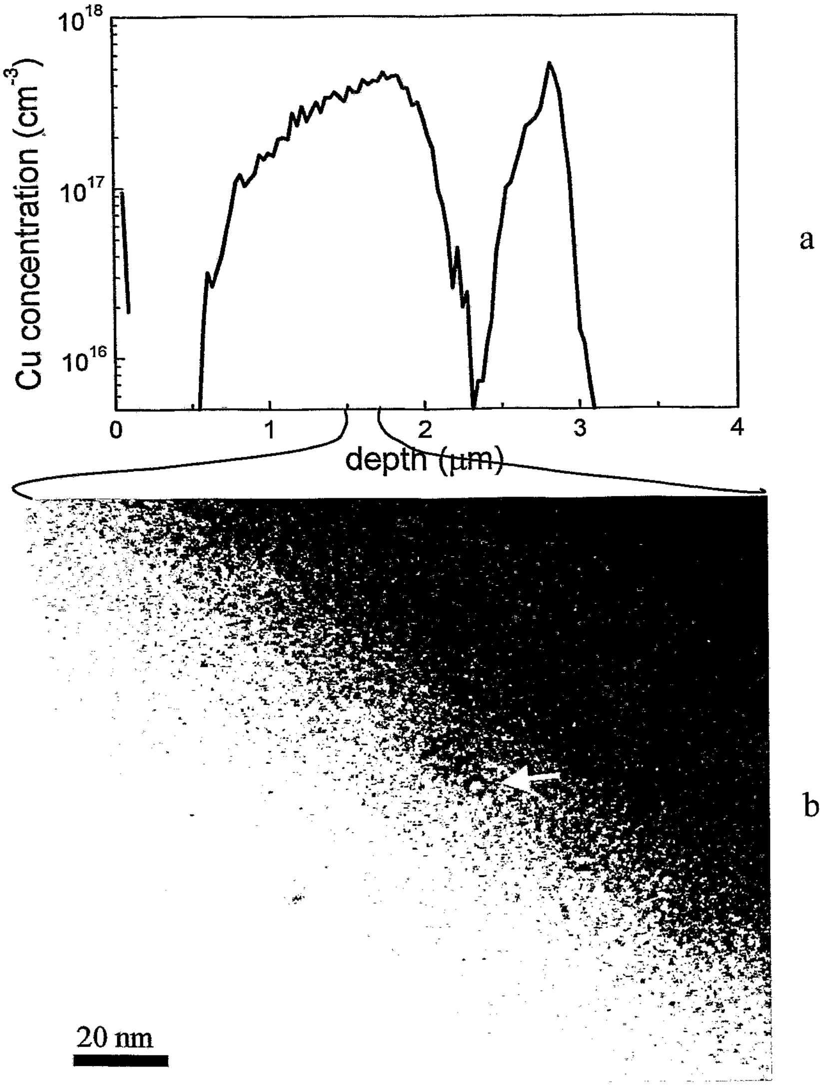

Fig. 4.11 (a) Cu depth SIMS profile of the 3.5 MeV, 5×10^{15} Si^{+}cm^{-2} implanted FZ n (100) Si contaminated by 3×10^{13} Cu^{+}cm^{-2} after furnace anneal of 700°C/1h followed by second anneal of 850°C/1h; (b); XTEM bright field micrograph of the $R_P/2$ region of the same sample as in (a), underfocus kinematical conditions, the cavities are indicated with arrows

Fig. 4.11 shows the Cu depth SIMS profile of the 3.5 MeV, 5×10^{15} Si^{+}cm^{-2} implanted n-FZ (100) Si together with the underfocus XTEM bright field micrograph of the $R_P/2$ region. The sample was implanted under the same conditions as the one shown in Fig. 4.10 but annealed at two steps: (700°C, 1h) and then subsequently (850°C, 1h) in furnace. The SIMS profile shows strong gettering at $R_P/2$ after the prolonged annealing time. The cleaved XTEM specimen reveals larger cavities at $R_P/2$ with lower density compared to the ones found in the 1 step annealed sample (Fig. 4.10). The mean diameter of the cavities $\phi = 5$ nm is bigger than the mean diameter of the cavities in the case of the one-step annealing (see Tab. IV.I). On the other hand, for samples implanted under the same conditions as the discussed ones but annealed for shorter time (30s, 180s – RTA) no defects were observed in the $R_P/2$ region while the corresponding Cu SIMS profile contains a pronounced $R_P/2$ gettering peak (not shown). It can be concluded that the vacancy type defects at $R_P/2$ are too small to be visible by TEM after the short RTA annealing. During the longer annealing time these vacancy clusters grow to bigger cavity type agglomerates which could be observed by TEM (Fig. 4.10 and 4.11).

Implantation conditions	**Annealing**	**Diameter ϕ of the cavities visible at $R_P/2$, nm**
3.5 MeV Si^+ into Si 5×10^{15} at/cm^2	RTA 900°C, 30s	not observable
	RTA 900°C, 180s	not observable
	FA 850°C, 1h	3.5
	FA 700°C, 1h + 850°C, 1h	5

Table IV.I Diameter ϕ of the cavities visible at $R_P/2$ region given with the corresponding implantation and annealing conditions. In all cases the existence of Cu gettering peak at $R_P/2$ was proven by SIMS depth profiling of the concentration of the subsequently introduced and annealed Cu.

The presence of vacancy-type defects in the $R_P/2$ region of ion-implanted and annealed Si is not sufficient in order to prove that they are the gettering sites for impurities. As it was shown in chapter 4.1.1, a coexistence of Si interstitials at $R_P/2$ is also possible and these kinds of defects are potential gettering centres for metals as well. Therefore, the relation between the excess vacancy generation and the appearance of $R_P/2$ gettering needs to be proven. This subject is dealt with extensively in the next two subchapters.

4.1.3 MeV ion implantation under inclined incidence

The study presented in the following chapter aims to prove the relation between the generation of excess vacancies after ion implantation and subsequent annealing and the $R_P/2$ metal gettering. One of the approaches applied is ion implantation at inclined incidence with respect to the sample surface. Fig. 4.12 shows a schematic of the disorder damage produced of ions implanted at normal (Fig. 4.12a) and inclined (Fig.4.12b) direction to the sample surface together with a schematic of the depth profile of the expected vacancy excess and interstitial excess profiles after subsequent annealing. The disorder production for implantation at inclined incidence basically proceeds in the same way as for implantation performed in perpendicular direction. However, the *depth* separation of the implantation generated vacancies and interstitials is expected to be not so pronounced for the inclined implantation as for the implantation performed in direction perpendicular to the surface. The depth region where the concentration of the generated vacancies is equal to the concentration of the interstitials (transition region) for inclined incidence implantation is expected to be much broader than the transition region for the implantation at perpendicular direction. Full vacancy-interstitial recombination is expected in the transition region after subsequent annealing. Because of the broad transition region (indicated with a grey rectangular in Fig. 4.12), the vacancy excess concentration and the interstitial excess concentrations after annealing are expected to be lower for the inclined implant than the corresponding ones after ion implantation at perpendicular to the surface incidence.

In order to prove the above discussed hypothesis the following experiment was carried out. The 3.5 MeV, 5×10^{15} at./cm^2 Si$^+$ implantation into Si was performed on n-type (100)CZ Si wafer under inclined directions of $\theta = 0$, 45° and 55°. The samples were RTA annealed at 900°C for 30s in Ar ambient. Cu was subsequently implanted into the rear side and redistributed throughout the sample by an additional thermal treatment of 700°C for 3min. SIMS analyses were performed in order to measure the Cu depth distribution.

Fig. 4.13 shows Cu profiles measured for Si$^+$ ion implantation under different incidence angles. The Cu profiles are plotted against the normalized ion range, x/R_P, to make them comparable because of the reduced R_P under inclined incidence. The Cu depth profile for perpendicular incidence (0°) shows the typical $R_P/2$ effect. For the 45° incidence

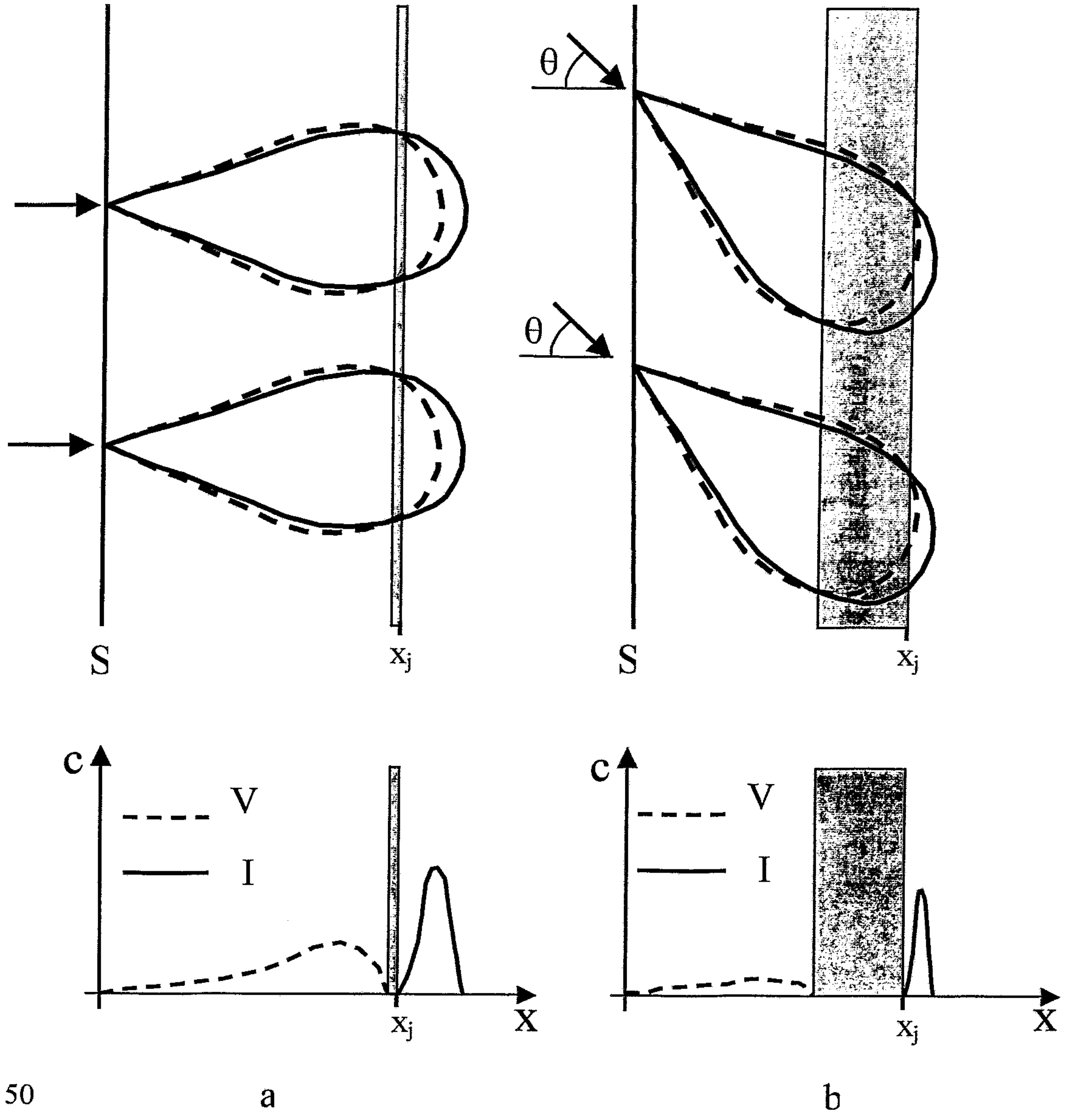

Fig. 4.12 A schematic representation of the disorder produced of ions implanted at perpendicular (a) and inclined (b) direction with respect to the surface. The dashed line represents the expected vacancy distribution after the ion implantation. The straight line represents the interstitial distribution after the ion implantation. S - the surface of the sample; x_j - junction depth; V_E - concentration of the excess vacancies after subsequent annealing, I_E - concentration of the excess interstitials after the subsequent annealing. The transition region is indicated as a grey rectangular.

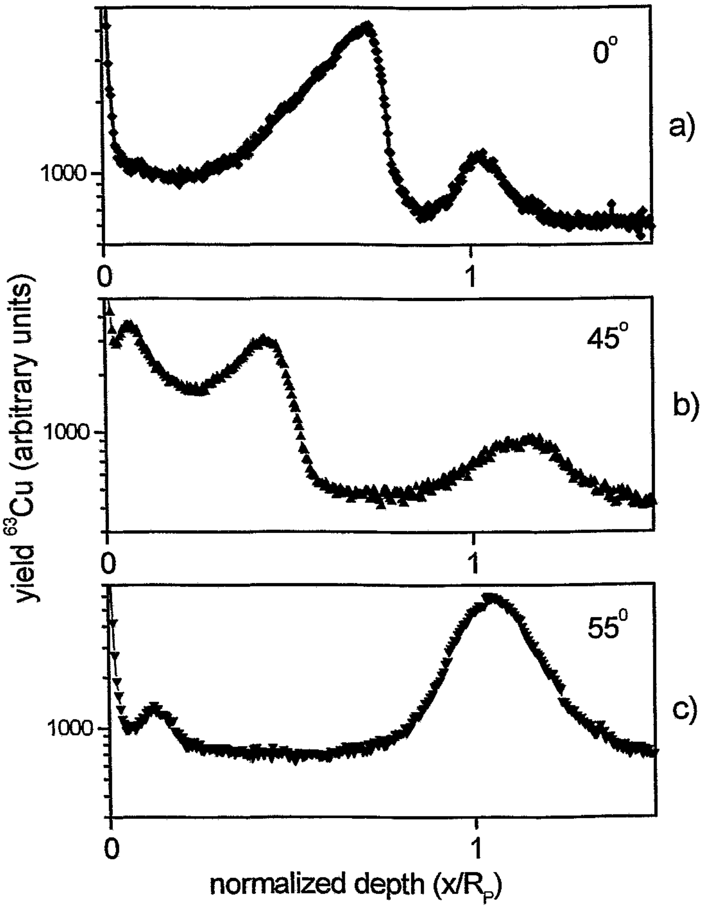

Fig. 4.13 Cu depth profiles of n-type (100) CZ-Si implanted with 3.5MeV Si^+ ions under different incident angles of 0° (a), 45° (b) and 55° (c), to a dose of 5×10^{15} cm^{-2} after annealing at 900°C for 30s.

the gettering layer around $R_P/2$ is significantly shifted to shallower depth position and the gettering layer at R_P is broader. For the 55° incidence the Cu gettering at $R_P/2$ disappears except for a small residual close to the surface. The residual gettering centres for metals in the sample are the ones at R_P. The defects at R_P getter the whole amount of Cu available in the sample. Therefore, the amount of Cu gettered at R_P is higher in this case than the amount of Cu gettered at R_P after perpendicular implantation. In the last case the R_P defects

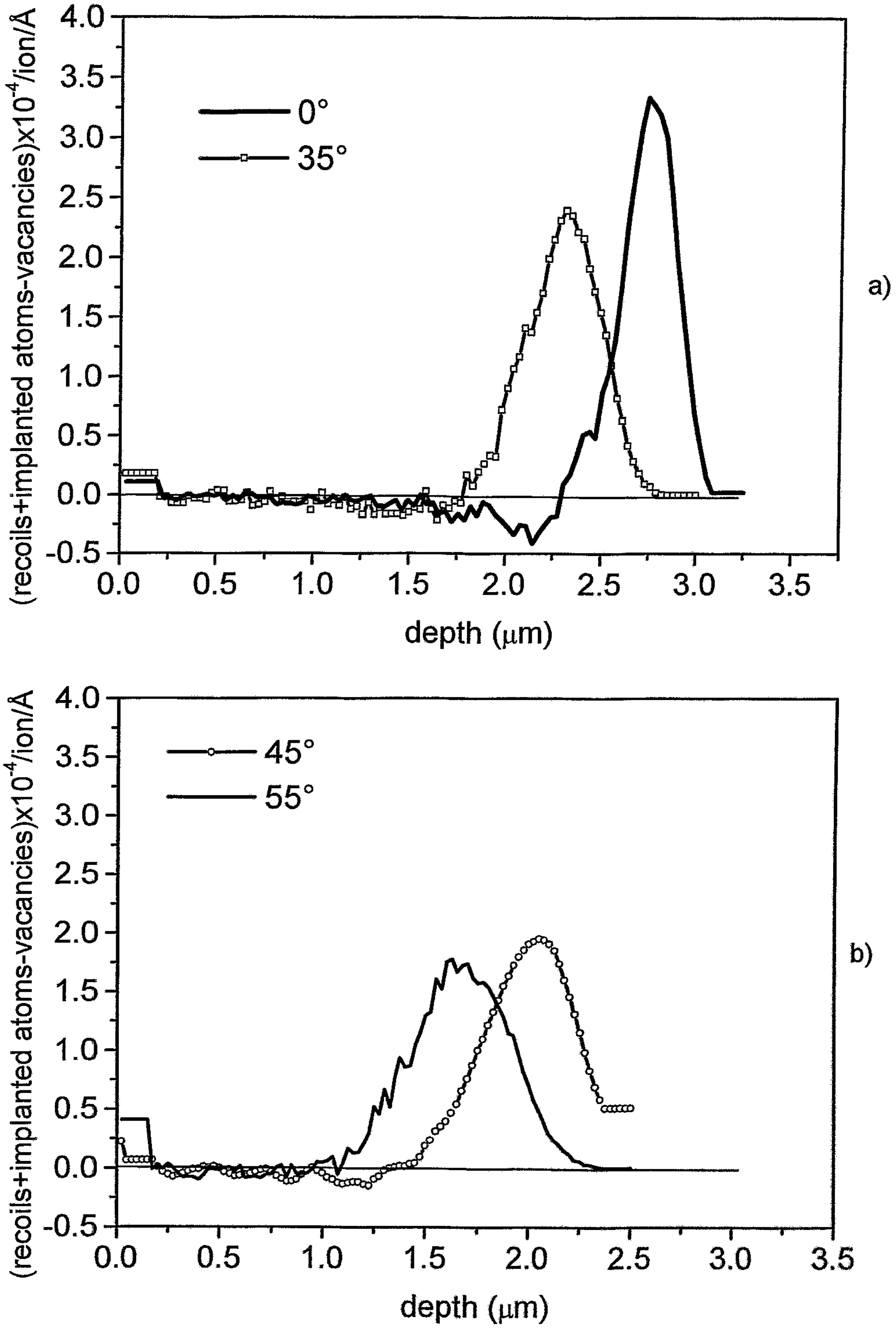

Fig.4.14 TRIM'98 calculations for the excess vacancy and interstitial profiles for the case of 3.5 MeV Si^+ion implantation into Si under different directions to the surface; 0°, 35°; (b) 45°, 55°.

and the $R_P/2$ defects getter the Cu competitively (discussed in Chapter 2.3). The results demonstrate the disappearance of $R_P/2$ gettering for an incidence angle of 55°.

The obtained experimental results can be compared with the calculated vecancy excess and interstitial excess profiles. The implantation process was simulated by a binary collision code TRIM'98. Fig. 4.14 shows the calculated excess vacancy and interstitial profiles for the 3.5 MeV Si^+-ion implantations under 0°, 35°,45° and 55°. The theoretically predicted narrowing of the vacancy excess region with increasing of the implantation angle is in very good agreement with the experimental data shown in Fig. 4.13. This means that excess vacancy agglomerates can be the gettering sites for metals at $R_P/2$. The total number of excess vacancies generated per implanted ion, V_E, in the axis perpendicular to the surface was calculated to decrease with increasing incidence angle, θ. However, these excess vacancies are localized in a narrower $R_P/2$ region, in the depth range, $0< x <x_J$. The value x_J is the junction depth between the vacancy-dominated $R_P/2$ region and the interstitial-dominated R_P region. The average concentration of excess vacancies, V_E /x_J, around $R_P/2$ is the crucial value for their agglomeration to form vacancy clusters or nanocavities at $R_P/2$ during annealing. Results of the calculations are summarized in Table IV.I.

θ (degree)	**R_P (μm)**	**x_J (μm)**	**V_E /ion**	**V_E /ion /cm**
0	2,59	2,27	0,186	819
35	2,12	1,77	0,112	634
45	1,82	1,28	0,068	530
55	1,48	1,05	0,023	220

Tab. IV.I Calculated implantation parameters for inclined incidence of 3.5MeV Si^+ ions.

The data of Tab. IV.I show that incidence angles, θ >45°, are necessary for a significant reduction of the excess vacancy concentration, to a value below 50% of that one for the perpendicular incidence (θ= 0°). These data agree well with the significant decrease of the amount of gettered Cu at $R_P/2$ in Fig. 4.13(c). That fact is another argument supporting the idea that the excess vacancy agglomerates could be the original gettering sites for metals at $R_P/2$.

4.1.4 Investigation of the $R_P/2$ effect by point defect recombination

Defect engineering was used by Holland and co-workers [Holl95] to avoid deterioration of surface Si layer after extremely high fluence oxygen implants (~ 1×10^{18} at/cm^2). In this study 150 keV Si$^+$ implant eliminated the vacancy related defects in the $R_P/2$ region of a 500 keV O$^+$ ion implant. A complementary effect was reported by Venezia et al. [Ven99] where the excess vacancies induced by a MeV Si$^+$ implant reduce the number of interstitial-related defects caused by low-energy implants during postimplantation annealing. However, in these experiments the undesired defects were either incompletely compensated or significantly overcompensated. The compensation factor **F** was calculated as a ratio of the additionally introduced Si interstitials to the excess vacancies needing to be recombined. The compensation factor was found to be **F** = 0.017 in Ref. [Holl95] and **F** = 34 in Ref. [Ven99].

The main goal of the following experiment is to check if the vacancy type defects are really and exclusively the gettering centres in $R_P/2$ region of MeV Si ion implanted Si. The idea is to balance the predicted excess vacancies at $R_P/2$ by implanting additional Si$^+$ ions (**F** = 1). This will give a quantitative evaluation of the excess vacancy concentration predicted by the theoretical simulations. The additional implants act as self-interstitials and have to be distributed in a way that their depth profile is equal to that of the excess vacancies. The gettering of intentionally introduced Cu atoms was used to evaluate the point defect annihilation. When full defect annihilation is achieved there will not be any more gettering centres for Cu and the gettering of Cu in the annihilation region will disappear. The use of this technique makes also possible to check if the vacancy-type defects are the gettering centres of metal impurities at $R_P/2$. The use of the metal gettering approach for evaluation of the point defect annihilation distinguishes this study from the studies discussed above. Holland et.al. [Holl95] used RBS/Channeling analyses to determine the damage level at $R_P/2$ of the extreme high fluence implants while Venezia et.al [Ven99] used the TED of boron to mirror the interstitial supersaturation.

The standard 3.5 MeV, 5×10^{15} at./cm^2 Si$^+$ implantation into Si was performed on p-type (100) Epi-Si with a thickness of 4 µm. An Epi-Si substrate was chosen in order to minimise the probability of metal gettering by impurities and intrinsic oxygen. In part of the samples an additional double Si$^+$ implantation was performed either with 1.7 and 0.75 MeV or with 1.4 and 0.7 MeV. The set of deeper implants was labelled (deep), the shallower one was labelled (shallow). This two sets of additional energies (s, d) were chosen in order to achieve fine fitting of the depth distribution of the additional implants to the depth distribution of the excess vacancies generated by the 3.5 MeV implant, as calculated by TRIM. It has to be considered that each additional implantation generates a new vacancy dominated region in its $R_P/2$ layer. The ion fluences of the additional implants were varied but the fluence ratio between the two implants was kept constant at ϕ_1: ϕ_2 = 2.7:1 and 1.7:1 for the deep and shallow implants respectively. In the results presented below only the sum, $\phi=\phi_1+\phi_2$ is given. The samples were annealed in furnace at 850°C for 30 min in Ar ambient. Subsequently Cu was introduced into the rare surface of the samples by implantation of 20 keV, 3×10^{13} Cu^+/cm^2 and redistributed throughout the sample by RTA at 700°C for 3 min.

The Cu depth distribution was measured by SIMS. The microstructure of each sample was analysed by XTEM.

Fig. 4.15 shows the depth distribution of the excess vacancies and excess interstitials resulting after the 3.5 MeV Si implant.

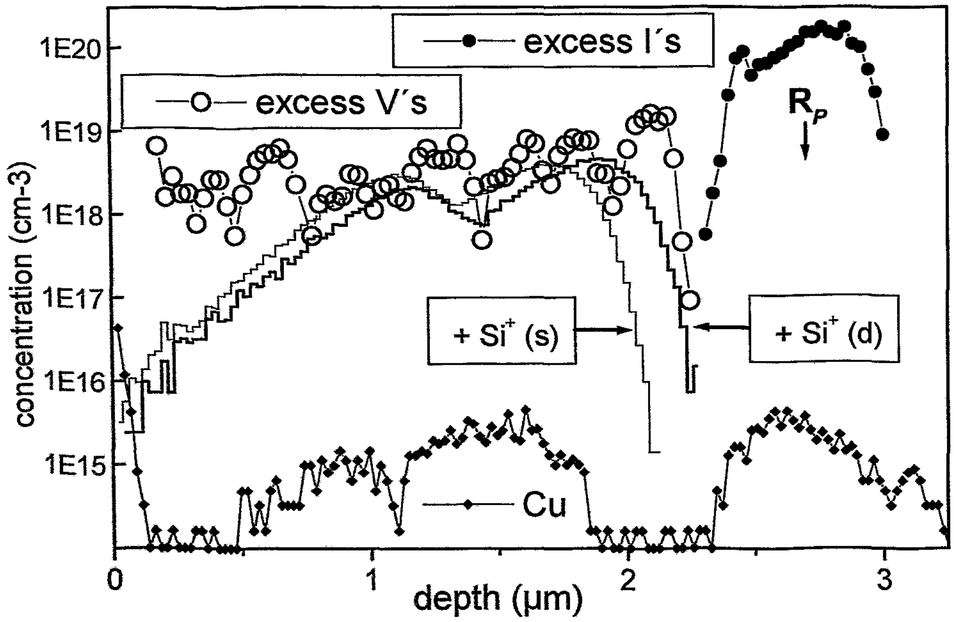

Fig. 4.15 Depth profiles of excess vacancies and excess interstitials calculated by TRIM 98 for implantation of 3.5 MeV, 5×10^{15} Si^+/cm^2 into Si, additionally the range profiles of Si^+ ions introduced by double implantation of 2.8×10^{14} at./cm^2 (shallow-s and deep-d) are shown. The Cu depth profile measured in Epi-Si without additional Si implants is indicated.

The profiles are calculated by TRIM 98 simulation code under the assumption of full local point defect recombination as described in Chapter 2.1. The calculated Si^+ implant profile sets (shallow and deep) of double Si implants are also presented in Fig. 4.15. Comparison of the additional implant profiles with the excess vacancy profile predicts point defect recombination in the region between 0.8 and 2.2 μm.

The effect of the point defect recombination by the deep additional Si implants is demonstrated in Fig. 4.16.

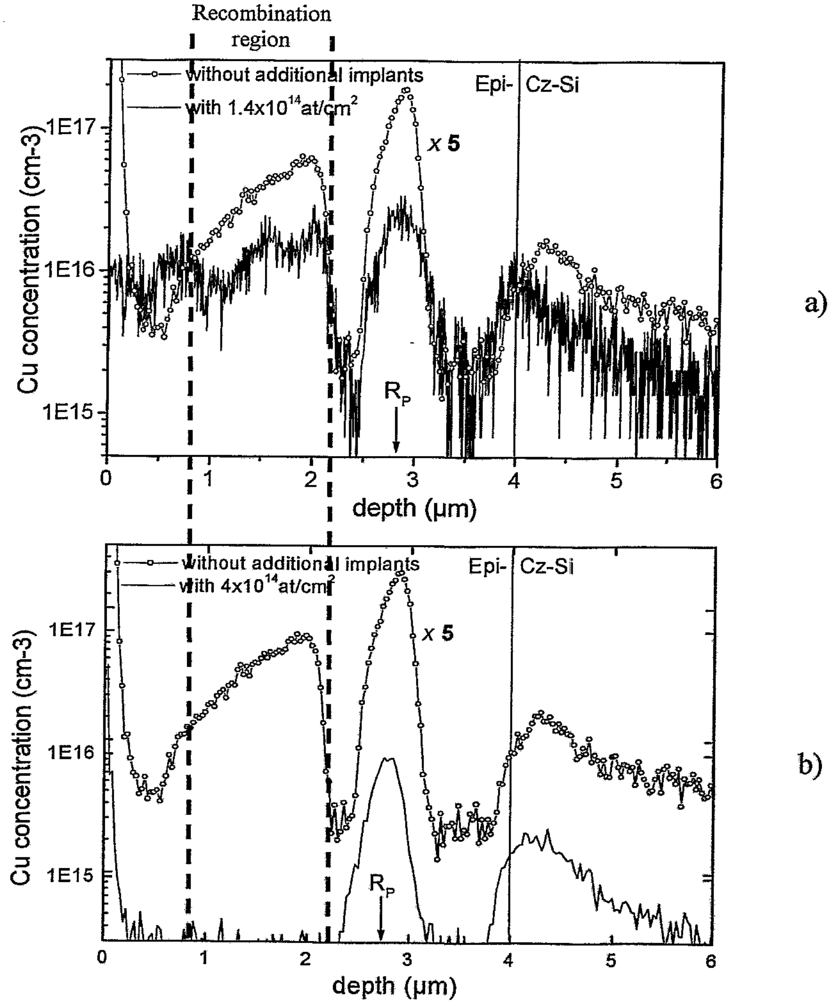

Fig. 4.16 SIMS Cu depth profile for 3.5 MeV, 5×10^{15} Si^+cm^{-2} implanted Epi-Si contaminated by 3×10^{13} Cu^+cm^{-2} after FA of 850°C/30 min correlated with the SIMS profiles of the samples with the deep additional implants to the fluences of (a)1.4×10^{14} at./cm^2 and (b) 4×10^{14} at./cm^2

The gettering at $R_P/2$ is slightly reduced for the 1.4×10^{14} at./cm^2 fluence of the additional implants compared to the gettering at $R_P/2$ in the reference sample (Fig. 4.16a). The increase of the additional implant fluence to 4×10^{14} at./cm^2 leads to complete disappearance of the $R_P/2$ metal gettering (Fig. 4.16b). The Cu peak at about 4 μm in Fig. 4.16 is attributed to the region around the Epi- to CZ-Si interface. This region contains defects, mainly dislocations, which are gettering centres for Cu therein. The TEM micrographs of the sample implanted with additional fluence of 4×10^{14} at./cm^2 and the reference sample (without additional implants) are shown in Fig. 4.17. The XTEM micrograph of the sample implanted with additional fluence of 4×10^{14} at./cm^2 (Fig. 4.17b) reveals that dislocation loops form an additional defect layer in the recombination zone at $0.8 < x < 2.2$ μm. These loops are of interstitial type and they are localised. The loops do not act as gettering centres for Cu as seen in the corresponding SIMS profile (Fig. 4.16b). For the lower fluence of the additional implants, 1.4×10^{14} at./cm^2 , the recombination region is free of defects by means of TEM (not shown). The additionally introduced self-interstitials for $\phi \geq 4\times10^{14}$ at./cm^2 overcompensate the excess vacancies. Moreover, the complete disappearance of the Cu gettering at $R_P/2$ in this case, is evidence that vacancy-type defects (excess vacancies) are the origin of those defects which getter metals at $R_P/2$. The total fluence of the additional implants needed to equalise the existing excess vacancies is between 1.4×10^{14} at./cm^2 and 4×10^{14} at./cm^2. Fig. 4.18 summarise the results of the full set of additional implantations performed. The fraction of Cu gettered in the $R_P/2$ region versus the fluence of the additional Si implantation in the recombination zone is plotted. It could be estimated that by an additional ion fluence of about $2.5 \div 3\times10^{14}$ at./cm^2 full vacancy compensation is achieved without formation of new defects. This value has to be compared with the theoretically predicted amount of excess vacancies of 6.3×10^{14} cm^{-2} in the same region (calculated from Fig. 4.1). These two values are in reasonable agreement considering that the TRIM calculations do not take into account defect diffusion, recombination at the surface and impurity-defect interaction.

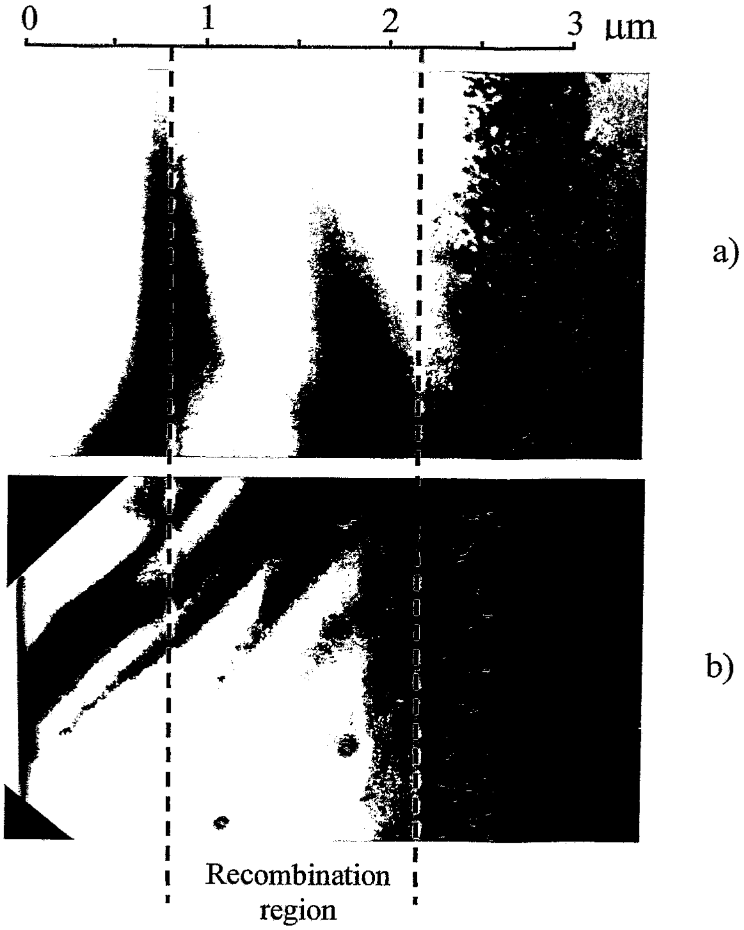

Fig. 4.17 XTEM bright field micrographs for (a) the reference sample implanted with 3.5 MeV, 5×10^{15} $Si^{+}cm^{-2}$ after furnace anneal of 850°C/30 min ; (b) with additional Si^{+} deep implants to the fluence of 4×10^{14} at./cm^2.

Fig. 4.19(a) shows the Cu SIMS profile for deep additional implants to the fluence of 2.8×10^{14} at./cm^2 together with the calculated profile of the self-interstitials introduced. Small resudual fraction of Cu is still gettered in the recombination region. This means that the depth distribution of the additionally implanted Si interstitials does not mirror exactly the depth profile of the excess vacancies generated by the 3.5 MeV Si^{+} ion implantatrion. Slight shift of the depth profiles of the additional implants towards the surface (shallow implants) leads to full compensation of the excess vacancies in the recombination region (Fig. 4.19b).

Comparing the defect structure at R_P of the sample with deeper 2.8×10^{14} at./cm^2 implant (Fig. 4.20b) and the reference sample without additional implants (Fig. 4.20a) one can see the broadening of the *R_P* defect layer towards the surface which could mean that part of the additionally implanted self-interstitials were trapped at R_P. This leads to the

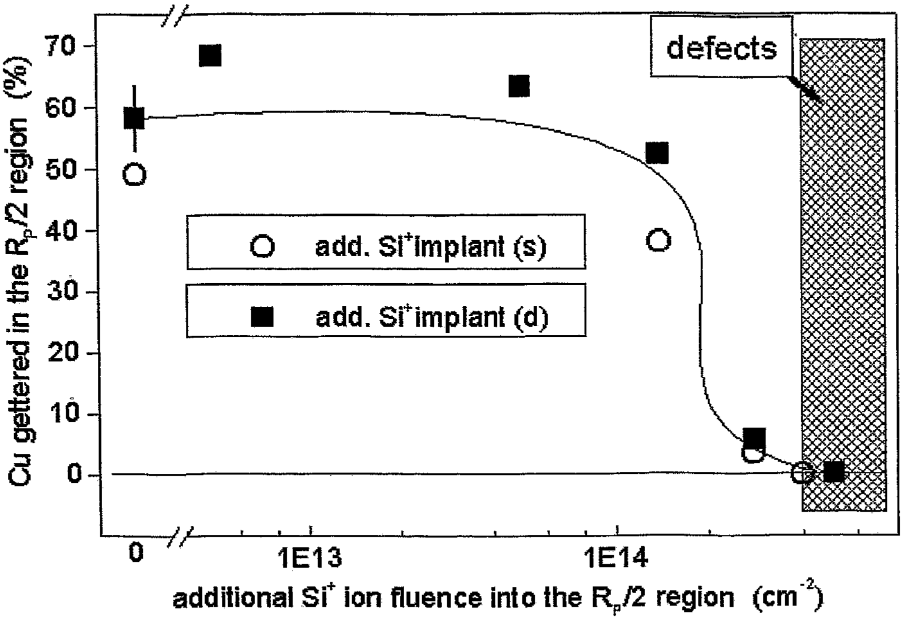

Fig 4.18 Fraction of Cu gettered in the $R_P/2$ region ($0.8 < x < 2.2$ μm) after implantation of 3.5 MeV, 5×10^{15} Si^+cm^{-2} into epi-Si and annealing at 850°C for 30 min versus the fluence of the additional Si into the $R_P/2$ region. The line is only to guide the eyes.

elongation of the defects therein. This result is consistent with previous work of Schreutelkamp et al [Schre91], which demonstrates that a spatially separated defect layer with higher damage concentration may act as a trap for self-interstitials. In the case of the deeper implant, the damage at R_P is the one with the highest damage concentration. The TEM image in the case of shallow additional implants (Fig. 4.20c) does not show broadening of the R_P defect layer as in the case of the deeper additional implants (Fig. 4.20b). This means that fewer self-interstitials introduced by the shallow additional implants are trapped by the defects at R_P than in the case of deep additional implants. Hence, more interstitials are recombining with the excess vacancies during the annealing after shallow additional implants than after deep additional implants. This leads to better compensation of the excess vacancies generated by the 3.5 MeV Si^+ ion implant in the recombination region (Fig. 4.19b80).

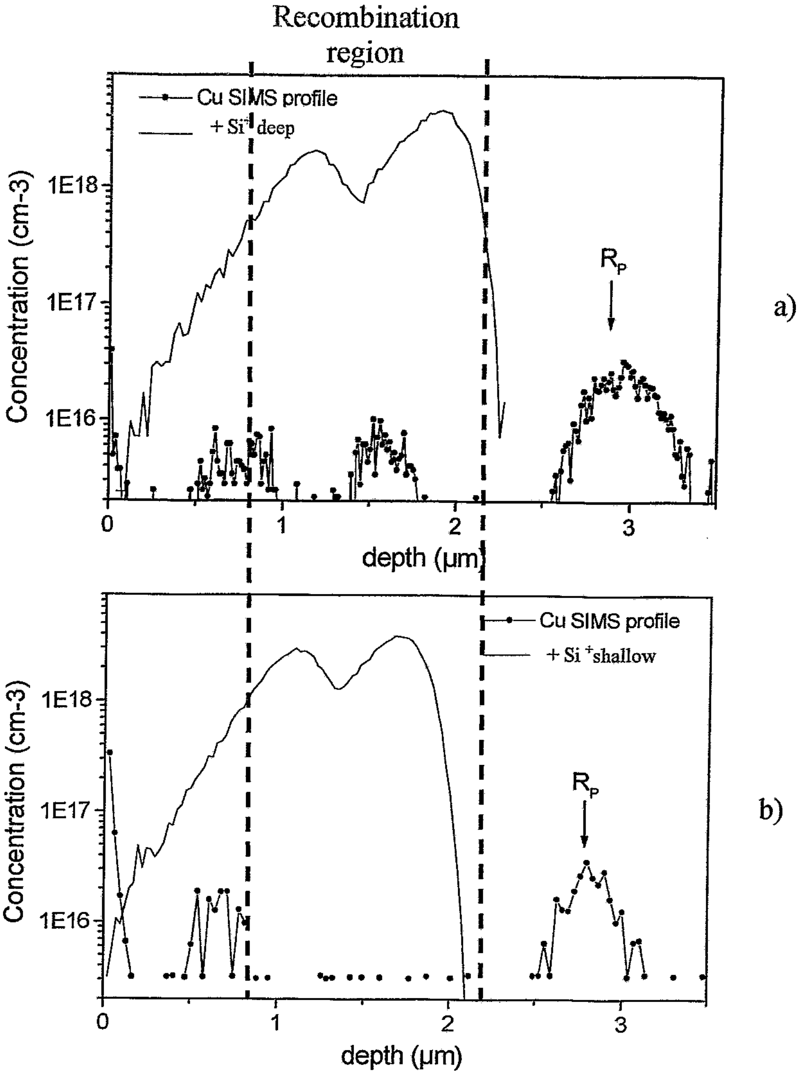

Fig. 4.19 SIMS Cu depth profile for 3.5 MeV, 5×10^{15} $Si^{+}cm^{-2}$ and additional 2.8×10^{14} $Si^{+}cm^{-2}$ deep (a) and shallow (b) implanted Epi-Si contaminated by 3×10^{13} $Cu^{+}cm^{-2}$ after FA of 850°C/30 min. The SIMS profiles are correlated with the depth profiles of the additional implants calculated by TRIM98.

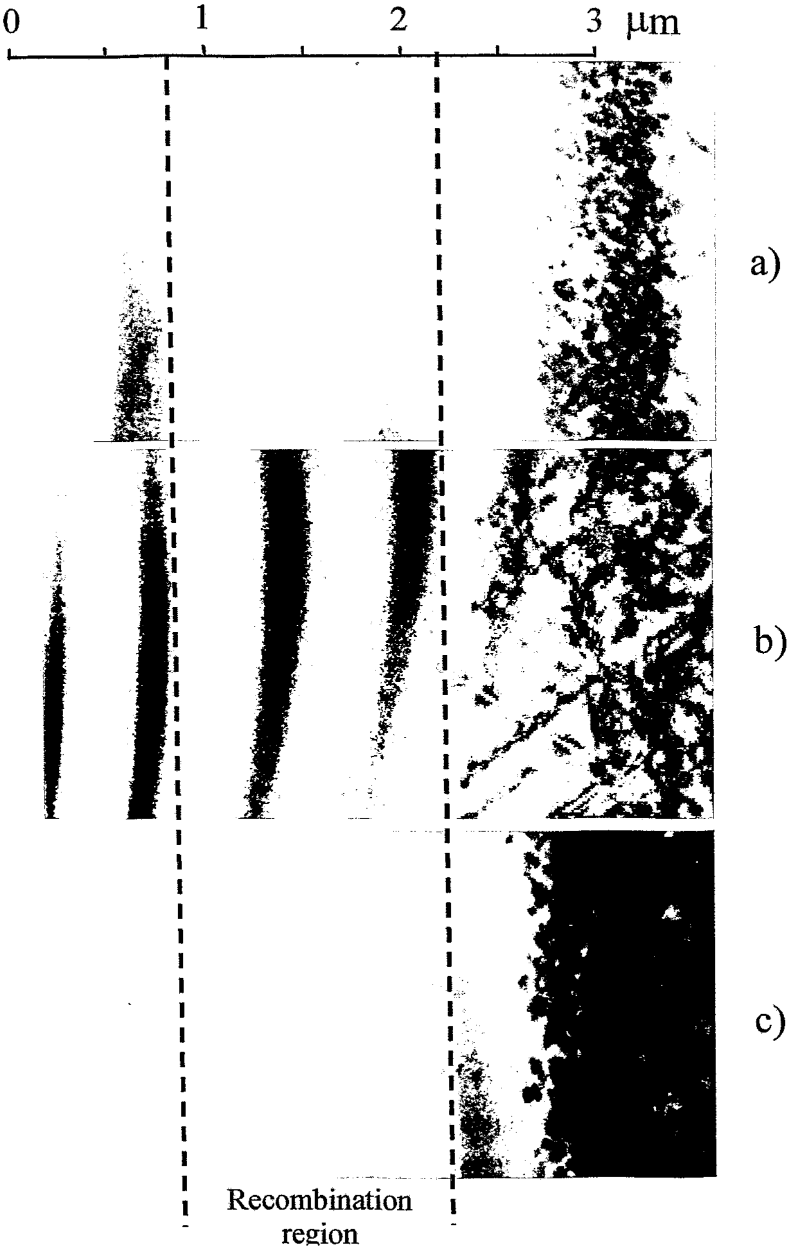

Fig. 4.20 XTEM bright field micrographs of the samples implanted with 3.5 MeV, 5×10^{15} $Si^{+}cm^{-2}$ and deep (b) and shallow (c) additional implants to the fluence of 2.8×10^{14} at./cm^{2} after furnace anneal of 850°C/30 min. The micrograph of a reference sample without additional implants is shown on (a).

4.1.5 The influence of the the R_P defect layer on the point defect recombination in the $R_P/2$ region

Eaglesham and co-workers [Eag97] showed large enhancement of antimony TED in the $R_P/2$ region of MeV Si^+ ion implanted and annealed Si. The experiments used delta-doped Sb superlattices grown by low-temperature molecular-beam epitaxy (MBE) as marker layers for the Sb diffusion. As Sb is known to diffuse by a vacancy mechanism, the large enhancement of the Sb TED is consistent with the pronounced vacancy supersaturation expected in this region of the implant. The authors suggest a total vacancy concentration ≈ 1×10^{18} cm^{-3}. Although unexpected, *a supersaturation of interstitials* in the same region was detected as MBE grown boron marker layers show diffusion on boron as well. Boron diffuses via interstitials hence its diffusivity is proportional to the concentration of Si self-interstitials. The enhancement of the B diffusion is found to be of the same magnitude as the enhancement of the Sb diffusion. Venezia et al [Ven99] suggested that the main reason for the presence of interstitials at $R_P/2$ is their indiffusion from the R_P region during annealing. A buried oxide layer (as a diffusion barrier for the silicon interstitials) in silicon-on-insulator (BESOI) substrate was used to isolate the B markers from the interstitial defects at R_P. The enhancement of B diffusion was significantly reduced but still present in the sample.

The simultaneous presence of both type of defects, interstitials and vacancies, in the $R_P/2$ layer after annealing in the absence of diffusion barrier for the interstitials coming from R_P open a question about the influence of the R_P - interstitials on the recombination processes in the $R_P/2$ layer. Do the R_P - interstitials recombine with the excess vacancies in the shallower than R_P region, or do the vacancies and the interstitials co-exist there? The idea of the following experiment is to investigate the influence of the R_P defects on the recombination processes in the Si top layer. The same implantations as described in the Chapter 4.1.4 were performed in Bond an Etched Silicon on Insulator (BESOI) structure with a 2.5 μm thick p-type FZ-Si top layer. This substrate was chosen in order to separate the R_P layer from the shallower ($R_P/2$) region. The R_P layer was deposited into the buried SiO_2 layer, which acts as a diffusion barrier for the Si interstitials. In this way the R_P defect layer is not able to contribute to the defect recombination in the Si top layer. The Cu depth profiles in the BESOI structure and in reference Epi-Si are compared in Fig. 4.21 for an additional shallow implant of 2.8×10^{14} at./cm^2. A pronounced Cu peak is observed in the Si top layer near the Si-SiO$_2$ interface whereas in the Epi-Si there is no Cu gettering at the same depth region. The difference between the Cu profiles in BESOI and Epi-Si substrate for one and the same implant can be explained by the recombination of a fraction of the interstitials at R_P with the excess vacancies at $R_P/2$.

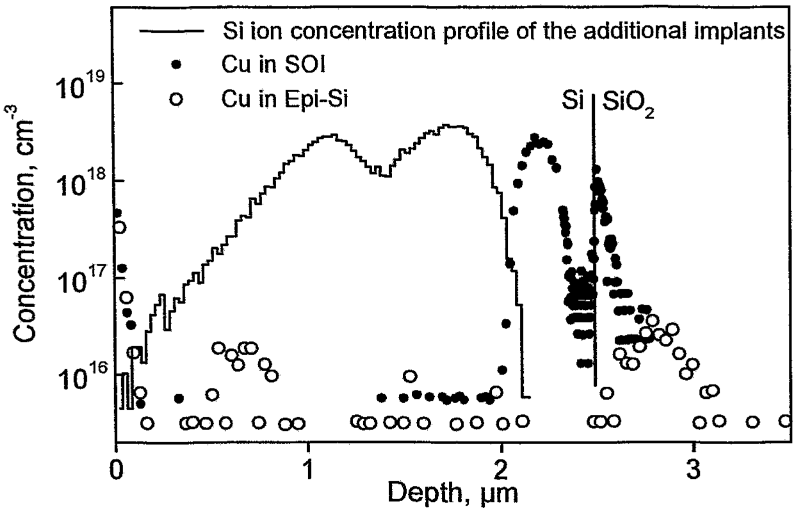

Fig. 4.21 Cu depth profiles measured for Epi-Si and BESOI substrates after implantation of 3.5 MeV, 5×10^{15} Si$^+$cm^{-2} and additional shallow implants to the fluence of 2.8×10^{14} at./cm^2 after FA of 850°C/30 min. The calculated depth profiles of the additional implanted Si ions are indicated.

The higher fluence of the additional implant, $\phi = 4\times10^{14}$ at./cm^2, leads to full loss of Cu gettering in the recombination zone in the BESOI structure (not shown), similar to the results obtained in Epi-Si for the same implantation and annealing conditions (Fig. 4.16b). There are no pronounced differences in the microstructure of the BESOI and the Epi-Si samples. An additional defect band of interstitial type dislocation loops (Fig. 4.22) indicats overcompensation of the excess vacancies.

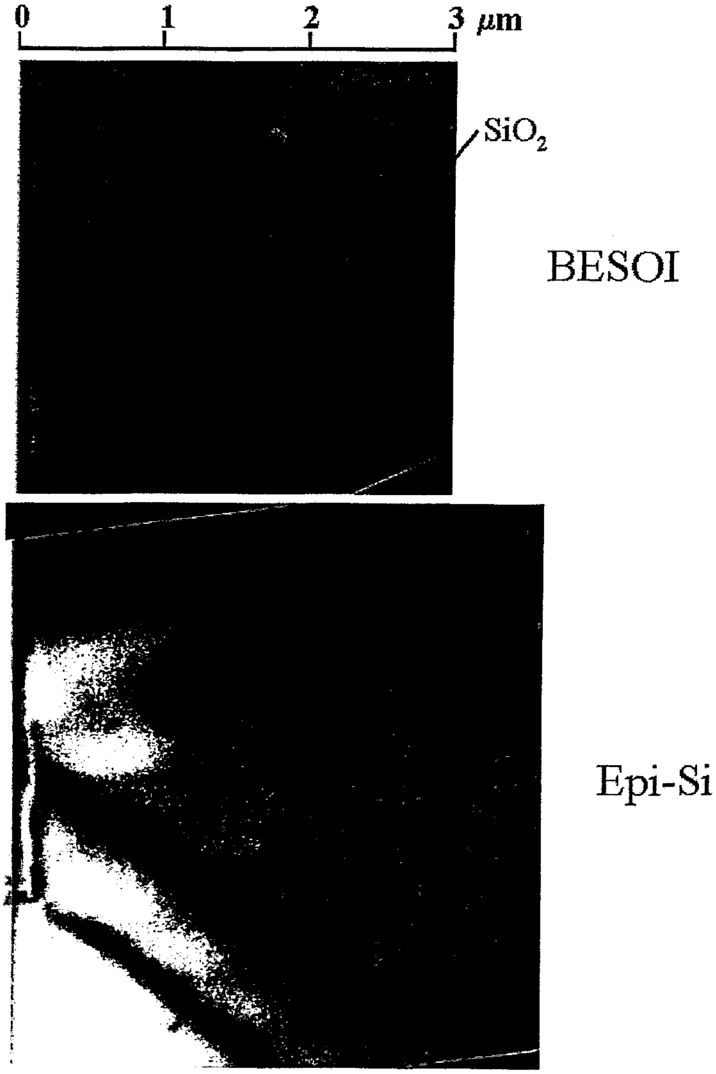

Fig. 4.22 XTEM bright field micrographs of the BESOI and the Epi-Si substrates implanted with 3.5 MeV, 5×10^{15} Si^+cm^{-2} and with shallow additional implantation of 4×10^{14} at./cm^2 after annealing at 850°C for 30 min.

In the present chapter it was shown that the metal trapping at $R_P/2$ can be prevented by means of additional Si^+ ion implantations. It was proven that the excess vacancies are the original gettering sides for Cu in the $R_P/2$ region.

4.2 Low energy He^+-ion implantation induced $R_P/2$ effect

In the following chapter an extension of the $R_p/2$-defect-related studies to the case of low defect production is presented. The low defect production regimes are induced by the implantation conditions: light ion implanted at low energies in random and channel direction. To avoid any chemical effects, He was chosen to be used as an implanted light ion.

4.2.1. Behavior of He in Si

Helium is a noble gas i.e. chemically almost inert. It is a light ion as well hence it causes low damage production while implanted into Si. Irradiation of Si with He^+ ions has been studied for many years. In particular, He is known to agglomerate into cavities when implanted in Si [Mye95]. A cavity band forms in the R_P region. The minimum Helium concentration required to form cavities is estimated to be ~ 3.5×10^{20} cm^{-3} [Rai95, Mye96]. He has a high permeability in Si, so that at relatively low temperatures it escapes from the wafer [Cri87, Fin88]. At ion implantation conditions (50 keV $He^+ \rightarrow$ Si, 2×10^{18} cm^2) close to the ones used in this work, after annealing at temperatures $T = 100 \div 250$ °C a strong gas release was observed and at $T = 300$°C a full loss of He was detected [Fin88]. The theoretical studies [Ala92, Est97] show that He is stable in the tetrahedral interstitial site in the Si lattice. This is not surprising since He does not interact chemically with the environment and therefore tends to be at the roomiest interstitial site available. Self-interstitials are not considered in the defect-He interactions theoretical studies because they are believed likely to repel He atoms rather than covalently bind to them. A single vacancy is found strongly to repel the He atom. In contrast, it was calculated that the He atom is stable in a divacancy [Est97]. When a He atom is placed in the divacancy, it remains very close to its geometrical center. The He-divacancy defect is more stable than the pure divacancy. The presence of He–divacancy complex has been also directly observed in photoluminescence spectra [Est97]. During the annealing, the small vacancy clusters, which are not decorated by He, dissolute to divacancies. These divacancies drift to the He-decorated vacancy clusters and form a shell of vacancies around them [Cer00]. Further, stable He-hexavacancy centers are formed during the annealing [Est97] and bigger He-vacancy agglomerates. At a certain stage this structure of He-vacancy clusters with a shell of vacancies around organize a cavity and capture therein most of He [Cer00]. Annealing at temperatures greater than 750°C drives out the He gas for several minutes [Mye98, W-Leu99]. Great interest has developed toward the applications of these cavities in the Si technology. It has been demonstrated that He filled cavities act as powerful gettering centers of transition metals [Rai95, Mye96, W-Leu95b, Moh95, Rai97, Kin97]. In particular, binding of Cu on the void internal surface has been intensively studied by Myers e*t al.* [Mye96]. ***Metals at low concentration*** are chemisorbed on the walls of the cavities. According to these authors the binding energy for Cu on void internal surface is 2.2 ± 0.2 eV. In particular, the experiments discussed in [Mye96] show that the saturation areal density of Cu in the cavity walls is 6.5 Cu atoms/nm^2. Moreover, cavity layers are able to reduce the solution impurity concentration by two orders of magnitude below the threshold for silicide precipitation [Mye96]. This is a noteworthy result taking into consideration that the road map for silicon device fabrication imposes levels for metal impurity concentration lower than the solid solubility which makes the metal gettering methods based on metal precipitation not longer usable. *Metals at high concentration* form a silicide phase on the internal surface of the cavity [W-Leu95a, Moh95].

4.4.2. Experimental details

In the present experiment n-type (100) oriented CZ-Si wafers. Details of the experimental data are given in Tab. IV.II.

In order to perform channeling implants, the Si wafers were aligned using a 500 keV He beam with an angular divergence of the order of 0.03°. The samples were mounted on a three-axis goniometer with a precision of 0.005°. The backscattered particles were detected by a surface Si(Li) detector placed at 170° with respect to the beam direction. The overall resolution of the detecting system was about 13 keV. When the HT channel implants were performed, first the sample was aligned into Si (100) direction at RT then, the goniometer was heated, and finally the alignment of the sample was checked again.

Energy (keV)	Fluence (He^+/cm^2)	Impl. temperature (°C)	Impl. direction	Anneal
40	0.5×10^{16} subthreshold fluence **(TF)**	room temperature **(RT)**	random	800°C/10 min RTA
	0.8×10^{16} low fluence **(LF)**	**RT**	channeling	
			random	
		350°C high temperature **(HT)**	channeling	
			random	
	3.5×10^{16} high fluence **(HF)**	**RT**	channeling	
			random	
		HT	channeling	
			random	
20	**LF**	**RT**	random	
40	**LF**	**RT**	random	800°C/1h FA

Table IV.II Experimental data for the He^+ ion implantation conditions

The implantation damage was annealed by RTA at 800°C for 10 min in Ar ambient. Some of the samples were annealed a second time by FA at 800°C for 1 h in an Ar ambient. All samples were contaminated with Cu by implantation at 20 keV, 1×10^{12} Cu^+/cm^2 on the back-side of the Si wafers in order to study the gettering of Cu atoms at the defect layer. The Cu was redistributed throughout the sample bulk either simultaneously with the damage annealing or subsequently after implantation using a second thermal treatment at 700°C for 3 min.

The following analyses were performed:

-The defect structure of the samples was investigated by TEM applied at cross-section and plan-view specimens. The specimens were prepared by low angle ion milling. For some of the samples additional XTEM specimens were prepared using the cleavage technique.

-The Cu distribution was measured by SIMS.

-The depth distribution of the equivalent of displaced silicon atoms was analyzed by RBS/C with a 1.2 MeV He^+ beam aligned to the (100) crystal direction.

-The distribution of the He content was investigated by ERDA technique, using a 10 MeV C^{4+} beam. The samples were tilted 73.5° and the detector placed at 28° with respect to the beam direction.

-XRD rocking curve analyses were performed using the θ-2θ scan on the (004) Si reflection using a double crystal setting in order to measure the stress in the Si lattice caused by defects created after the He^+ ion implantation and subsequent annealing. Stepwise etching was performed in order to determine the stress arising from defects located in different depth.

4.2.3 Damage production by He implantation in random and channeling direction

In order to reduce the implantation-induced damage in the $R_p/2$ region channeling implantation into the (100) Si channel was performed. The theoretical calculations for the helium distribution and the implantation induced damage i.e. vacancy and interstitial concentration for both random and channeling implantation are shown in Fig. 4.23.

The theoretical calculations presented in Fig. 4.23 predict that the vacancy and the interstitial concentrations at $R_P/2$ caused by the channeling implantation are almost one order of magnitude lower then the ones caused by the random implantation. The damage profiles of the channeling implantation are broader than the ones of the random implantation and the damage distribution is shifted with about 100 nm towards the bulk material.

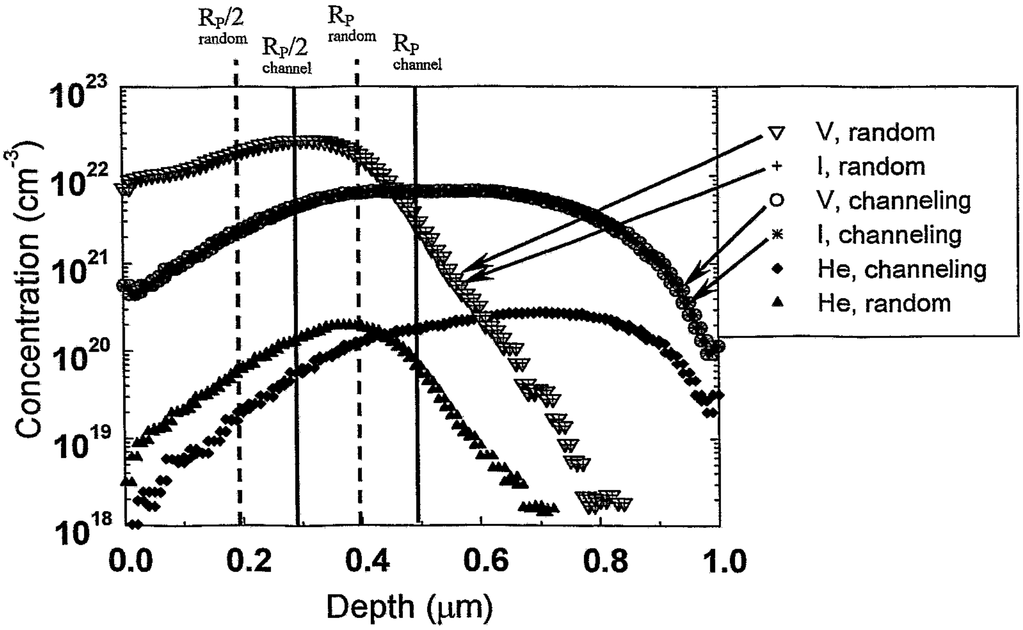

Fig. 4.23 Calculated depth profiles of vacancies **V**, interstitials **I** and He atoms for 40 keV, 0.8×10^{16} He^+/cm^2 implantation into random and channeling directions, using Crystal-TRIM [Pos]. The $R_P/2$ and the R_P depth positions are indicated for both channeling and random implantation. The vacancy and the interstitial profiles almost overlap for the random as well as for the channeling implants.

4.2.4 Low fluence He^+ implantation into Si: random and channeling implantation; RT and HT implantation

Fig. 4.24(a) presents the Cu distribution for the channeling implantation performed at RT together with the corresponding XTEM micrographs. The existence of two Cu peaks in Fig. 4.24(a) clearly reveals the $R_P/2$ effect in the implanted Si. The deeper peak in Fig. 4.24(a) is situated at the region of the He^+ ion mean projected range. No evidence of Cu precipitation was observed by TEM. The Cu gettering in the R_p region is consistent with what is known about the defect structure after He^+ ion implantation (discussed in Chapter 4.2.1). As discussed in details in Chapter 4.1, the TEM analyses are dramatically influenced by the XTEM specimen sample preparation. The cleaved specimen reveals cavities at $R_P/2$ with a mean diameter of 3 nm (not shown). The milled TEM specimen (Fig. 4.24a) does not show any additional defect structure at $R_P/2$. A detailed comparison of the TEM imaging of milled and cleaved He^+ ion implanted samples are presented in Chapter 4.2.11

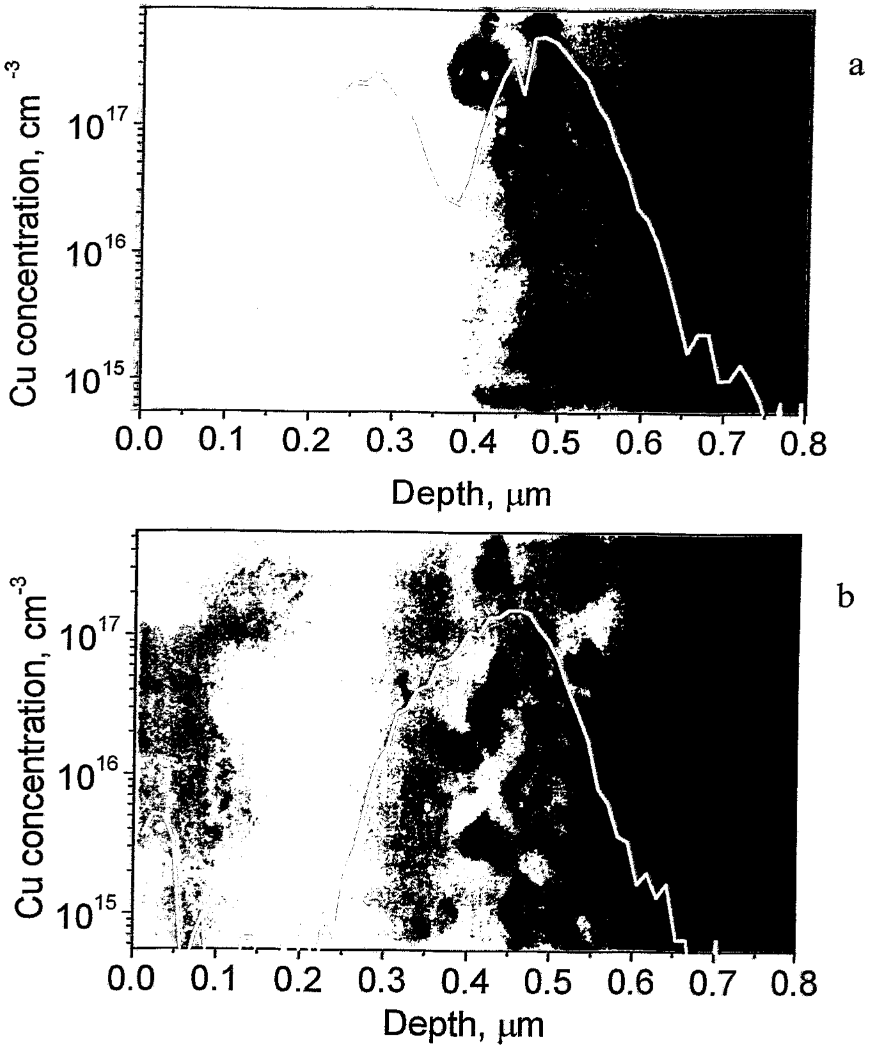

Fig.4.24 SIMS Cu depth profiles and a XTEM bright field micrographs for samples implanted at 40 keV, 8×10^{15} He^+/cm^2, channelling direction, contaminated by $1x10^{12}$ Cu^+/cm^2 after 800°C/10 min RTA; (a) – RT implant, (b) – HT implant, underfocus

Fig 4.24b) shows the Cu depth distribution for the 350°C implant together with the corresponding XTEM micrograph. As can be clearly seen, the SIMS spectrum has only one Cu peak with a maximum situated at ≈ 450 nm. This maximum is slightly shifted towards the surface as compared with the one obtained in the R_p region for the RT implant (Fig. 4.24a). This feature correlates with previous observations which demonstrate that under high temperature implantation the center of the cavity layer is formed not at the R_p of the He^+ ions but closer to the maximum of the damage distribution induced by the ion implantation [Fich00].

A careful investigation of the TEM results reveals quite different microstructural features in both samples (Fig. 4.24a, Fig.4.24b). After annealing, the RT He^+ implantation gives rise to a well-defined bimodal He cavity size distribution, characterized by a population of large cavities with mean diameter of ∅ ~ 25 nm and of a smaller ones with ∅ ~ 10 nm. The depth position of the cavity layer correlates with the Cu peak at R_p in the corresponding SIMS profile. The depth distribution of the cavities in the R_P region is narrow. On the other hand, for the HT He^+ implantation a single mode He cavity size distribution with a mean diameter ∅ ~ 9 nm is observed. The defect layer of the HT implant is broader as compared with the one observed after RT implantation. The depth distribution of the cavities for the HT implant is slightly inhomogeneous. The cavity concentration is a bit higher in the middle part of the damage layer than on the wings. Both micrographs also show dislocation loops emerging from the cavity structures.

The Cu distribution for the RT random implant together with the corresponding XTEM micrograph is shown in Fig. 4.25a). The existence of two Cu peaks is clearly indicated in the SIMS data. The first one is located at ≅ 200 nm and the second one at ≈ 370nm. The deeper peak is situated at the region of the He^+ projected range as deduced from the TRIM code range calculations (Fig. 4.23). As in the case of channeling implantation the shallower Cu peak can be ascribed as $R_p/2$ gettering peak.

The TEM analyses show similar features as in the case of the channeling implantation. The defect layers at R_P in the random implanted samples are shifted towards the surface with about 100 nm compared to the defect layers at R_P in the channeling implanted samples. This is in agreement with the TRIM calculations (Fig. 4.23).

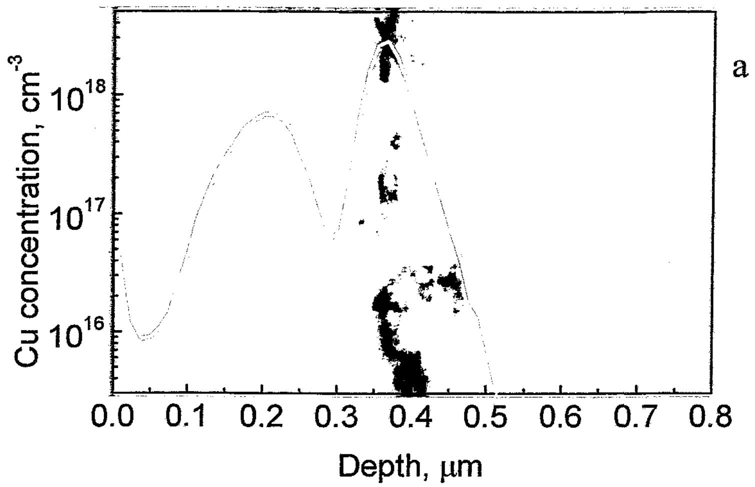

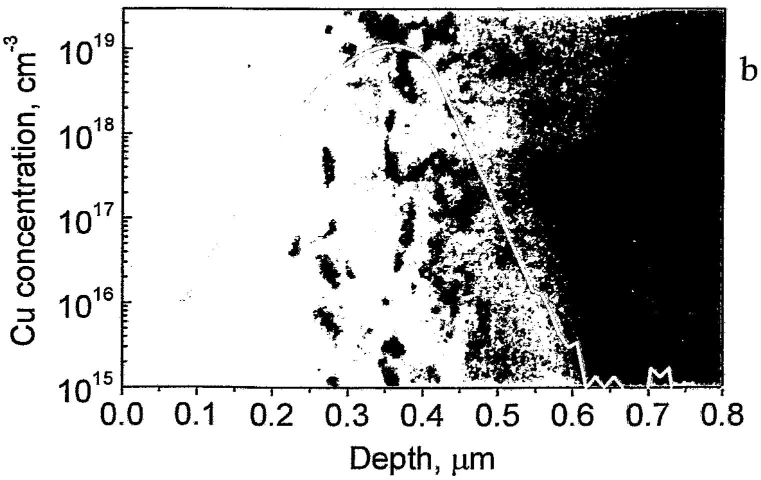

Fig. 4.25 (a) SIMS Cu depth profile after implantation at 40 keV, 8×10^{15} He^{+}/cm^{2}, RT, random direction, contaminated by 1x10^{12} Cu^{+}/cm^{2} after 800°C/10 min RTA. The SIMS profile is combined with an underfocused XTEM bright field micrograph of the same sample; (b) the sample is the same as in (a) but implanted at HT.

4.2.5 Damage observed by RBS/C after He$^+$ ion implantation: random and channeling implantation, RT and HT implantation

The RBS/C spectra corresponding to the random RT (solid circles), random HT (stars), channeling RT (open squares), channeling HT(open circles) He implants before the thermal annealing, together with the spectrum corresponding to the non-implanted sample (solid triangles) are shown in Fig. 4.26.

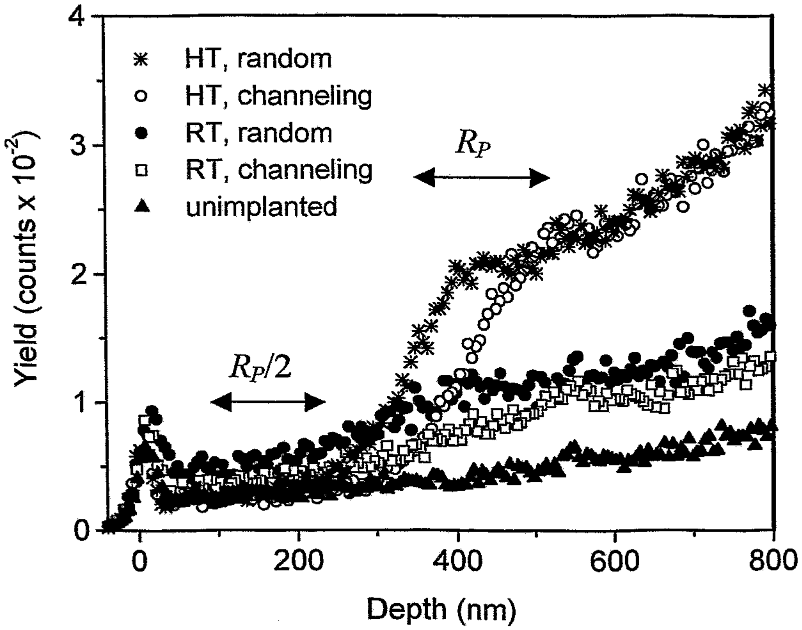

Fig. 4.26 RBS/C spectra from the samples implanted to the fluences of 8×10^{15} He$^+$/cm^2 at RT channelling (open squares) and random (solid circles) direction compared with the same samples implanted at HT channeling (open circles) and random (stars) direction. The spectrum from an unimplanted sample (solid triangulars) provides a scale for the minimum damage level detected in the RBS/C measurements.

Comparing the RBS/C spectrum for the HT random implanted sample with the non-implanted one it can be observed that up to a depth of ≈ 250 nm there is only a very small difference. For depth above 250 nm the backscattering yield of the spectra corresponding to the HT implant increases significantly. This feature is correlated with the nucleation and growth of the He cavities in the as-implanted sample, as revealed by TEM (not shown). On the other hand, the RBS/C spectrum corresponding to the random RT implant shows larger yield in the near surface region as compared to that one of the HT sample. Near the surface the minimum channeling yield is $\chi_{\min} = 6\%$ (compared to the HT sample, $\chi_{\min} = 4\%$).

The above measurements indicate that the HT implant does not induce any sizeable damage in the $R_p/2$ region, which is in agreement with the TEM observations. Concerning the RT implant the RBS/C measurements show that the implantation process leaves a damage that goes from the near surface up to the R_p region. The subsequent thermal treatment anneals out most of the damage in particular in the $R_p/2$ region of the sample. This statement is supported by the TEM observations performed after the thermal anneal which show the existence of extended defects only at the R_p region.

The results of the RBS/C measurements for the channeling implanted samples mirror the results obtained for the random implantation. The only difference is that the obtained spectra are slightly shifted to the depth by ≈100 nm as a consequence of the channeling implantation conditions.

After performing the annealing, the RBS/C spectra of both RT and HT samples show in the $R_p/2$ region no difference when compared with the non-implanted one (not shown).

4.2.6 Comparison of the Cu gettering in He$^+$ ion implanted Si for the different implantation conditions

Results for high fluence (HF) He$^+$ ion implantation in channeling direction are presented. In Fig. 4.27 Cu distributions for the implantation performed at RT (Fig. 4.27a) and 350°C (Fig. 4.27b) together with the corresponding TEM micrographs are shown. The SIMS profile obtained for the RT implant indicates the existence of one peak at 500 nm, a shoulder around 400 nm and a broad Cu distribution centered at around 250 nm which can be characterized as a $R_p/2$ peak. The mean diameter of the cavities at R_P for the HF implant is about 13 nm.

Comparing the Cu SIMS profiles for the HF and the LF implantation (Figs 4.24a and 4.27a) one can observe that the R_p peak for the HF implant is broader than the one obtained for the LF implant. This correlates with the cavity layer at R_p which for the HF (Fig 4.27a) is broader and the cavity concentration much higher than for the LF case (Fig 4.24a). For the HF implant the depth distribution of the cavities in the R_p region is, in contrast to the LF implantation, inhomogeneous.

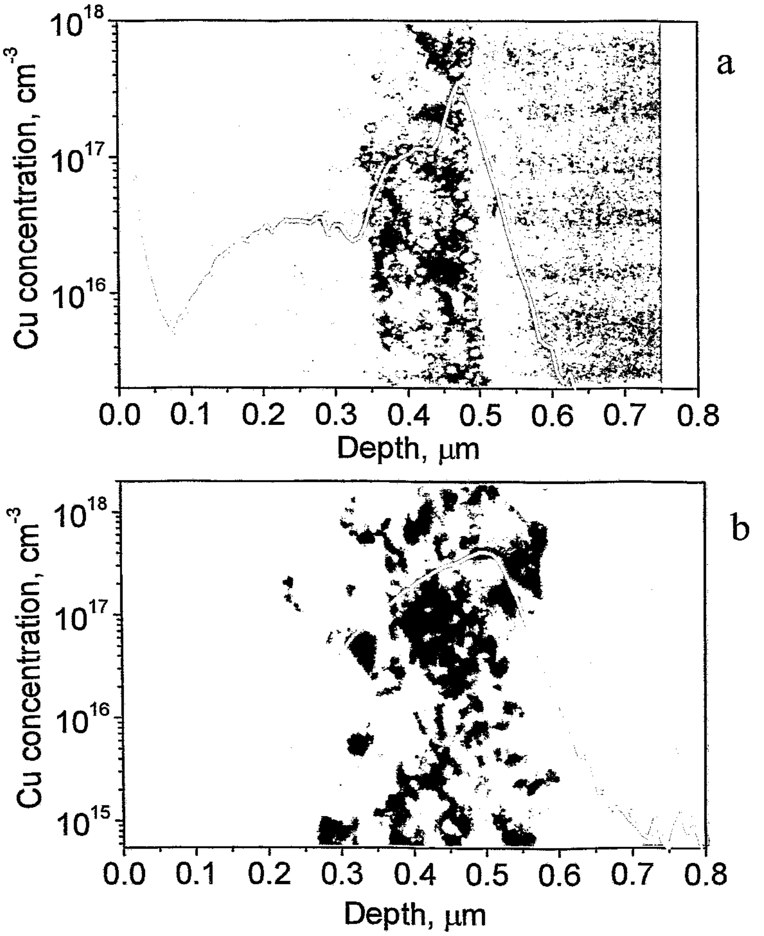

Fig.4.27 (a) SIMS Cu depth profile for the sample implanted at 40 keV, 3.5×10^{16} He^+/cm^2, RT, channelling direction, contaminated by $1x10^{12}$ Cu^+/cm^2 after 800°C/10 min RTA. The SIMS profile is combined with an underfocused XTEM bright field micrograph of the same sample. (b) the sample is the same as in (a) but implanted at HT.

The cavity concentration is higher at the deeper border of the R_P defect layer. This is the reason for the asymmetrical shape of the Cu profile at R_p in Fig. 4.27(a). No extended defects are observed in the vicinity of the $R_p/2$ peak as in the case of LF implantation (Fig

4.24a). In the case of LF HT implant (Fig. 4.24b), the Cu depth profile obtained after the HF HT He implant (Fig. 4.27 b) shows the existence of only one peak that goes from 600 nm down to the 100 nm depth with the maximum around 400 nm. The TEM micrograph shows at the R_p region a buried defect layer containing dislocations and cavities with mean diameter ∅ ~ 14 nm. This value is slightly higher than the one for the LF HT implant (∅ ~ 9 nm). The depth distribution of the cavities at R_P in the HT HF implanted sample, as in the LF HT sample, is slightly inhomogeneous with a tendency to slightly higher defect concentration in the middle part of the damage layer then on the wings.

The RBS/C measurements in the as-implanted and annealed samples of the HT and RT implants indicate (not shown) similar behavior as the one observed for the LF implants. Only in the case of the as implanted RT sample larger backscattering yield was observed in the $R_p/2$ region as compared to the non-implanted sample.

High fluence random implantations were performed, for both RT and HT conditions. The HF random implants have the same features as the HF channeled implants being present only shallower about 100 nm compared to the ones in the channeling implantation spectra (not shown).

On closer inspection, the Cu profiles of the results presented above show that the profiles of the RT implants have a double peak structure for the LF and HF samples implanted at random or channeling direction. This feature can be deduced from Fig. 4.28. In the figure are displayed the Cu concentration depth profiles according to reduced depth (x/R_P) and concentration variables. The reduction of the depth was performed for the channeled spectra by comparing the micrographs of the random and the channeled implant and overlapping the middle parts of the damaged layers at the R_P region. In this manner the channeled spectra were shifted towards the surface with about 100 nm. The Cu concentrations of all spectra were normalized to the highest R_P peak, the one of the Cu profile in Fig. 4.25(a). Comparing LF and HF implants, different features can be observed. The LF implanted sample show two different Cu regions corresponding to R_p and $R_p/2$. At variance the Cu profile of the HF implant has three distinct regions: one in the R_p region corresponding to gettering on the larger cavities; a shoulder, which indicates gettering on the small bubbles and a less pronounced peak corresponding to the gettering of Cu by the nanocavities in the $R_p/2$ region.

It is remarkable that all the HT implants display a single Cu peak located at R_p. This feature is seen in Fig. 4.29, which shows the normalized Cu concentration versus the reduced depth for both fluences and implantation directions. For all HT implants a similar shape of the R_p gettring peak is observed.

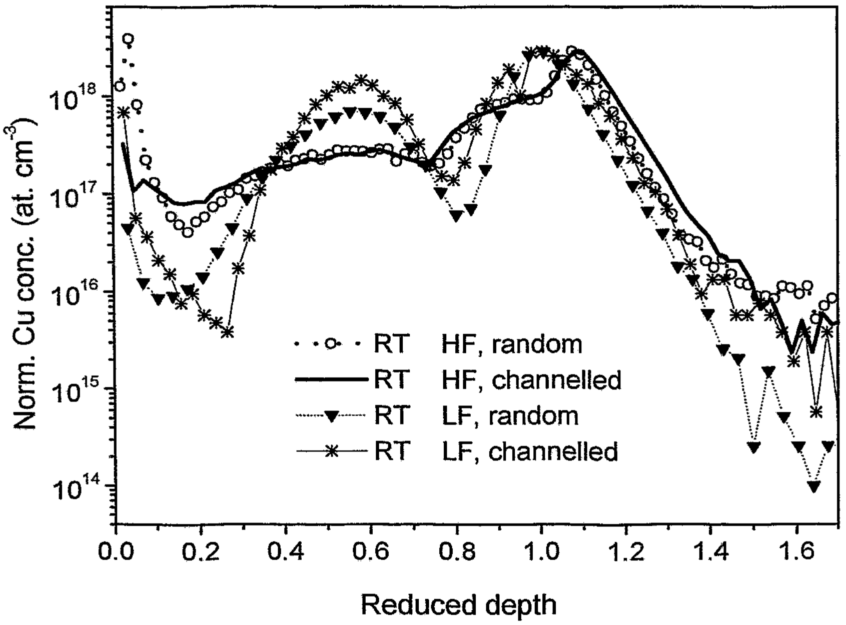

Fig.4.28 Normalised SIMS Cu depth profiles versus the reduced depth of the **RT** implants: HF random (open circles), HF channelling (straight line), LF random (solid triangular), LF channeling (stars).

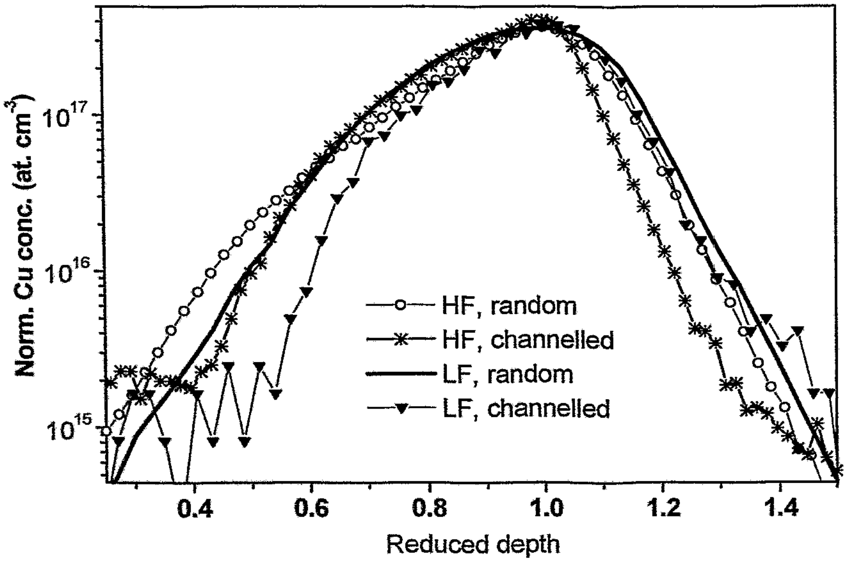

Fig. 4.29 Normalised SIMS Cu depth profiles versus the reduced depth of the **HT** implants: HF random (open circles), HF channelling (stars), LF random (straight line), LF channeling (solid triangulars).

4.2.7 Annealing effects

ERDA measurements were performed for all HF He^+-implanted samples. The measurements for the LF samples show that the concentration of He inside the samples was under the sensitivity level of the ERDA measurements.

In Fig. 4.30 the ERDA spectra are displayed corresponding to the RT and HT implants in the as implanted and annealed state for the random implants. The measured He concentration profiles for the as-implanted samples (Fig. 4.30a) show different behavior for each implantation condition. The He concentration peak for the RT implanted sample is deeper then the calculated R_P, whereas the HT implanted He distribution is located closer to the region where the maximum damage production is predicted. The shift of the maximum He concentration of the profile indicates that depending on the implantation temperature, distinct cavity nucleation mechanism takes place. If the temperature of the sample during the implantation is high enough, the He mobility is enhanced. The He-vacancy reaction rate could be increased and the cavity formation takes place at the region of the maximum production of the damage.

The results obtained after the annealing at 800°C for 10 min (Fig. 4.30b) reveal that the RT implanted sample has lost about 80% of the implanted Helium content. On the other hand, the HT implanted sample has lost about 90% of the He content. These values are in agreement with the results reported in reference [Kasch97]. Both distributions become narrower and shift a bit toward the surface. The maximum of the He concentration profile corresponds to the depth where the cavity layer is observed by means of TEM. The present results show that a measurable amount of He is still present within the cavity layer even after the 800°C annealing.

The ERDA spectra of all the HF He channel implants (not shown) have the same characteristics as described above. Only the channel He spectra is shifted toward the bulk.

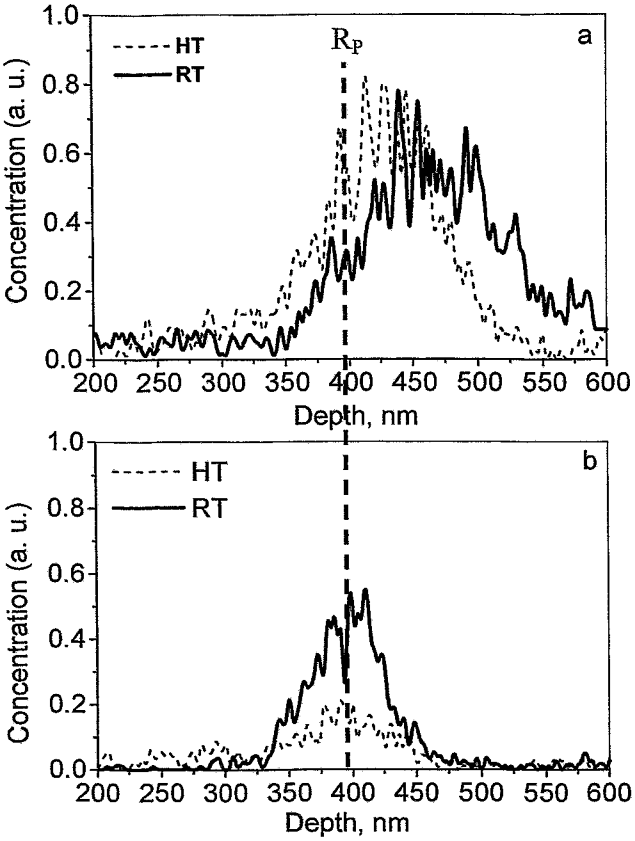

Fig. 4.30:

(a) He concentration depth profiles from the as-implanted samples at 40 keV, $3.5\times10^{16}He^+/cm^2$, random direction at RT (straight line) and HT (dotted line) evaluated by ERDA; (b) the samples are the same as in (a) but annealed at 800°C/10 min.

4.2.8 Threshold fluence for the $R_P/2$ effect induced by He^+ ion implantation

40 keV He^+ ions were RT implanted at random direction with $\phi= 0.5x10^{16}at/cm^2$. In Fig. 4.31 the Cu distribution is shown together with the corresponding TEM micrograph. The Cu depth profile shows a single peak located in the R_p region with no indication of Cu trapping at the $R_p/2$ vicinity. This feature indicates threshold fluence for the $R_p/2$ effect induced by He^+ ion implantation. From the present results it can be concluded that this threshold fluence is $0.5\div0.8\times10^{16}$ He^+/cm^2. These values correspond to the peak He concentration $2.7\div3.5\times10^{20}$ He^+/cm^3. The corresponding excess vacancy concentrations were calculated to be $2.6\div3.5\ \times10^{18}$ He^+/cm^3.

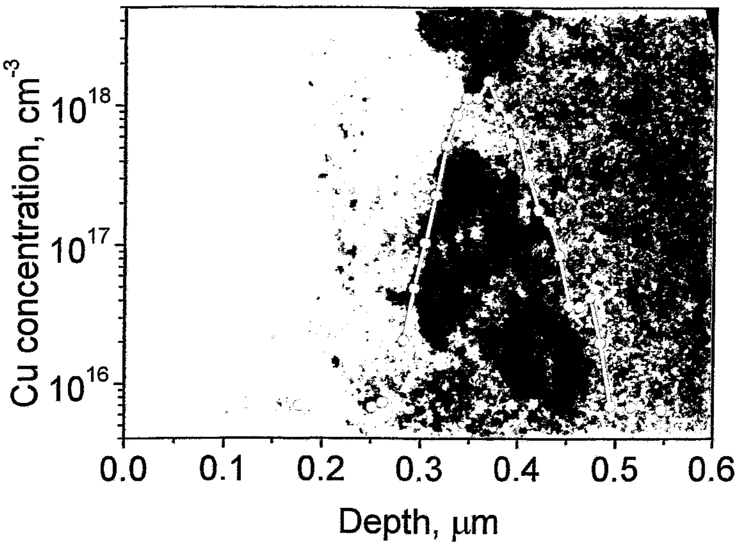

Fig. 4.31 SIMS Cu depth profile for the sample implanted at 40 keV, 0.5×10^{16} He$^+$/cm^2, RT, random direction, contaminated by $1\text{x}10^{12}$ Cu$^+$/cm^2 after 800°C/10 min RTA. The SIMS profile is combined with an underfocused XTEM bright field micrograph of the same sample.

4.2.9 The influence of the surface proximity on the $R_P/2$ gettering induced by He$^+$ ion implantation

Twenty keV He$^+$ ions were implanted at RT in random direction with $\phi = 0.8\text{x}10^{16}$ at/cm^2. In Fig. 4.32 the Cu distribution after annealing is shown together with the corresponding TEM micrograph. The SIMS measurements show the existence of two Cu peaks. The first is located at 240 nm, that is in the R_p region and the second at about 120 nm, which corresponds to the $R_p/2$ vicinity. The TEM micrograph show the existence of dislocations and cavities around the R_p. The use of lower energy is a particular experiment in order to investigate the influence of the proximity of the surface to the defects at $R_p/2$. Experimental observations on the point defect diffusion show that both interstitials and vacancies exhibit migration interrupted by trapping at impurities (C, O) and dopant atoms [Rim98].

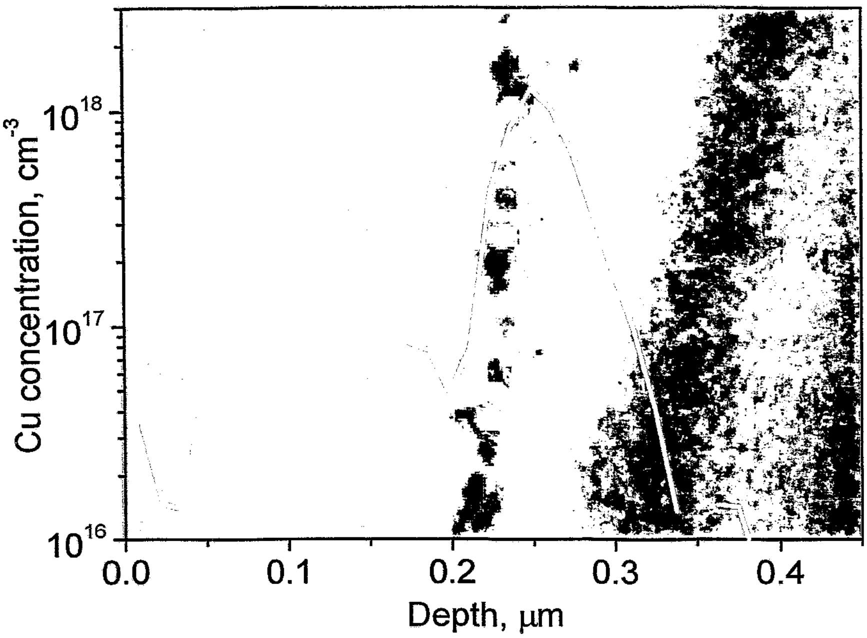

Fig. 4.32 SIMS Cu depth profile for the sample implanted at 20 keV, 8×10^{15} He$^+$/cm^2, RT, random direction, contaminated by $1\text{x}10^{12}$ Cu$^+$/cm^2 after 800°C/10 min RTA. The SIMS profile is combined with an underfocused XTEM bright field micrograph of the same sample.

The above study presents results showing the interstitials being faster than the vacancies. It is estimated that the trap-limited diffusion length of the vacancies in the Cz-Si material (with oxygen concentration ~ 3×10^{18} Cm^{-2}) is ~ 0.1 µm [Rim98]. Hence it is expected that part of the excess vacancies in the $R_P/2$ region produced by the 20 keV implant could recombine either at the surface or with the excess interstitials in the R_P region (note that the distance between the $R_P/2$ gettering peak and the surface in Fig. 4.32 is ~ 0.1 µm). The well pronounced double peak structure in the SIMS Cu profile observed for the 20 keV implant is similar to the one measured for 40 keV implant (Fig. 4.25a). It can be concluded that no remarkable defect recombination at the surface is taking place. This means that the proximity of the surface does not play a significant role for the appearance of the $R_p/2$ gettering effect in the frame of the present implantation and annealing conditions.

4.2.10. Time evolution of the nanocavities during annealing

Fig. 4.33 shows the Cu SIMS profiles of the sample presented in Fig. 4.25(a) together with the SIMS profile of the same sample after an additional FA at 800°C for 1 h. In this case Cu gettering was found only at the R_p region. This means that the defects acting as gettering sites at $R_p/2$ have been removed during the prolonged annealing cycle. The bright field kinematical overfocused images of the cleaved samples whose SIMS profiles are shown in Fig. 4.33 are presented in Fig. 4.34. The sample that shows $Rp/2$ gettering also reveals small cavities at $R_p/2$ in the cleaved TEM specimen (Fig. 4.34a). These cavities are not present in the sample that was annealed for longer time (Fig. 4.34b). The last sample also does not show gettering at $R_p/2$. Therefore the disappearance of the gettering at $R_p/2$ in conjunction with the disappearance of the cavities therein supports the hypothesis that the nanocavities at $R_p/2$ are the real gettering centers for Cu.

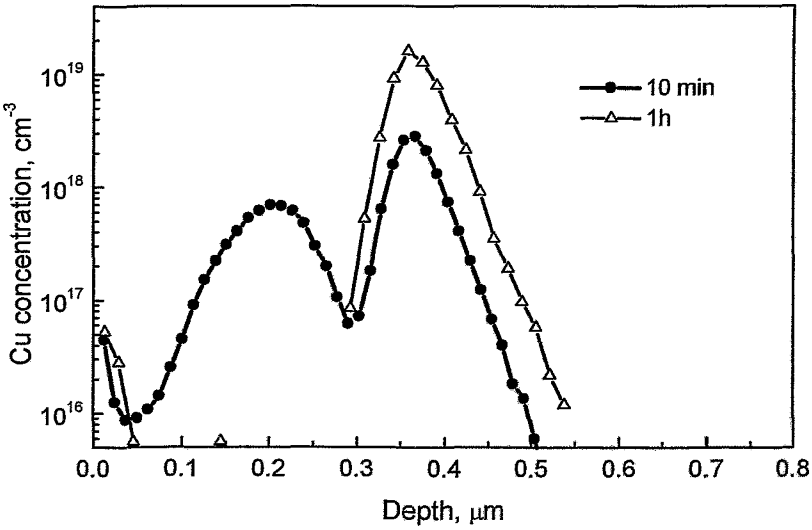

Fig. 4.33 (a) SIMS Cu depth profile for the sample implanted at 40 keV, 8×10^{15} He^+/cm^2, RT, random direction, contaminated by $1x10^{12}$ Cu^+/cm^2 after 800°C/10 min RTA (solid circles) and after additional FA at 800°C/1h (open triangular).

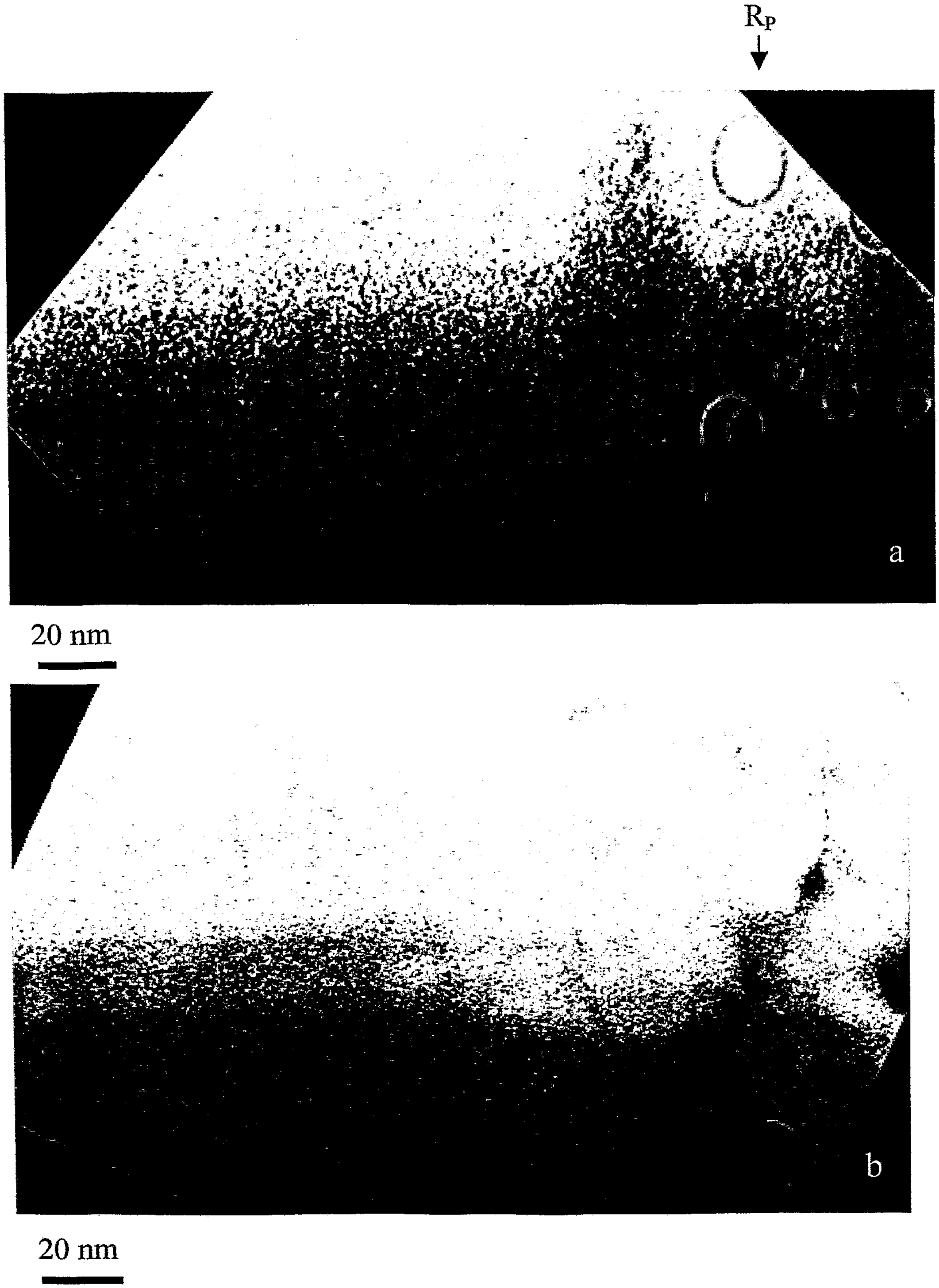

Fig. 4.34 XTEM bright field micrographs of cleaved specimens of the sample implanted at 40 keV, 8×10^{15} He^+/cm^2, RT, random direction, contaminated by $1\text{x}10^{12}$ Cu^+/cm^2 after 800°C/10 min RTA (a) and after additional FA at 800°C/1h (b). Kinematical conditions. Overfocus. Note the small cavities at the $R_P/2$ region in (a) appearing as darker spots than the background.

4.2.11 Comparison of the TEM investigations of cleaved and ion-milled He^+ ion implanted specimens

In the following description, a representative example will be given which compares the TEM results obtained by the high-angle-ion milled specimen and by the cleaved one. The 20 keV He^+ ion implanted sample was chosen as representative because, as can be seen below, the complete structure of the sample (original surface, the $R_P/2$ defect layer and the R_P defect layer). can be shown in *one* extremely highly magnified XTEM image. This allowes the imaging of the complete defect structure of the sample under high magnification which is needed for the visualisation of the $R_P/2$ cavities. To have only one image with all structural features of the sample is a good way of illustration of the comparison that is a topic of this chapter. The SIMS Cu profile and a low magnified TEM image obtained from the milled specimen of this sample is presented in Fig. 4.32.

The cleavage technique was used for the TEM sample preparation. Fig. 4.35 presents a bright field TEM micrograph of a cleaved specimen prepared of a sample which was implanted at 20 keV, 8×10^{15} He^+/cm^2, contaminated by $1x10^{12}$ Cu^+/cm^2 and after that annealed (RTA, 800°C/10 min). The $R_P/2$ effect is observed for this sample by means of Cu gettering (presented in the next chapter in Fig. 4.31). The images are taken under kinematic underfocused (a), and overfocused (b) conditions. For comparison images of the same sample from a milled specimen taken exactly under the same magnification and imaging conditions are presented in Fig. 4.36. A careful look at figures 4.35 and 4.36 shows the following features:

The R_P defect layer is clearly visible in both milled and cleaved specimen. It consists of relatively big He^+ ion implantation induced cavities with a diameter $\varnothing = 15 \div 20$ nm. For defects with these and bigger dimensions both kind of sample preparation techniques, ion milling and cleaving, give similar results.

The milled specimen does not show any defects at $R_p/2$ distinguishable from the background. The background of the milled sample reveals specific contrast which is not observed in the cleaved specimen. Extremely small vacancy-type defects (diameter ≈ 1 nm) cover homogeneously the whole surface of the milled specimen. These defects are introduced during the Ar-beam milling of the TEM specimen (discussed in 4.1.1.3). The size of the defects is under or just about the resolution of the microscope. The roughness of the surface of the milled specimen and the amorphous layer created during milling also contribute to the contrast of the background. The existence of these artefacts blur the original defect structure at $R_p/2$ in the milled specimen and obscure it in the microscope. Moreover, the size of the sample preparation induced cavities becomes bigger approaching the wedge of the specimen. They form a layer there (indicated with an arrow in Fig. 4.36). Such a cavity layer is not observed in the cleaved specimen (Fig. 4.35). This fact proves that the defects observed close to the surface are introduced during the TEM specimen preparation. The appearance of the artefact-cavities does not depend of the presence of He in the sample as such ion-milling induced cavities were observed in the Si^+ ion implanted Si samples as well (discussed in 4.1.1.3). The presence of the ion-milling induced cavities tends to confuse the TEM analysis leading to incorrect conclusions on the original defect structure, especially when the sample needed to be investigated contains small cavities with diameters $\varnothing \sim 2 \div 4$ nm, as in the present study of $R_P/2$ effect.

The cleaved specimen reveals, additionally to the cavities at R_p, another cavity band situated at $R_p/2$. The mean diameter of the cavities in the $R_p/2$ region is $\varnothing \sim 3$ nm. The through focus imaging confirms their vacancy-type character (explained in details in 3.1 and shown in Fig 4.35). The depth distribution of the cavities at $R_p/2$ coincides with the position of the Cu peak measured by SIMS (Fig. 4.32). The presence of Cu in the sample plays no role for the imaging of the cavities at $R_p/2$ as a sample implanted and annealed under the same conditions but not contaminated with Cu reveal the same cavity structure at $R_p/2$ as the sample which was contaminated with Cu (not shown).

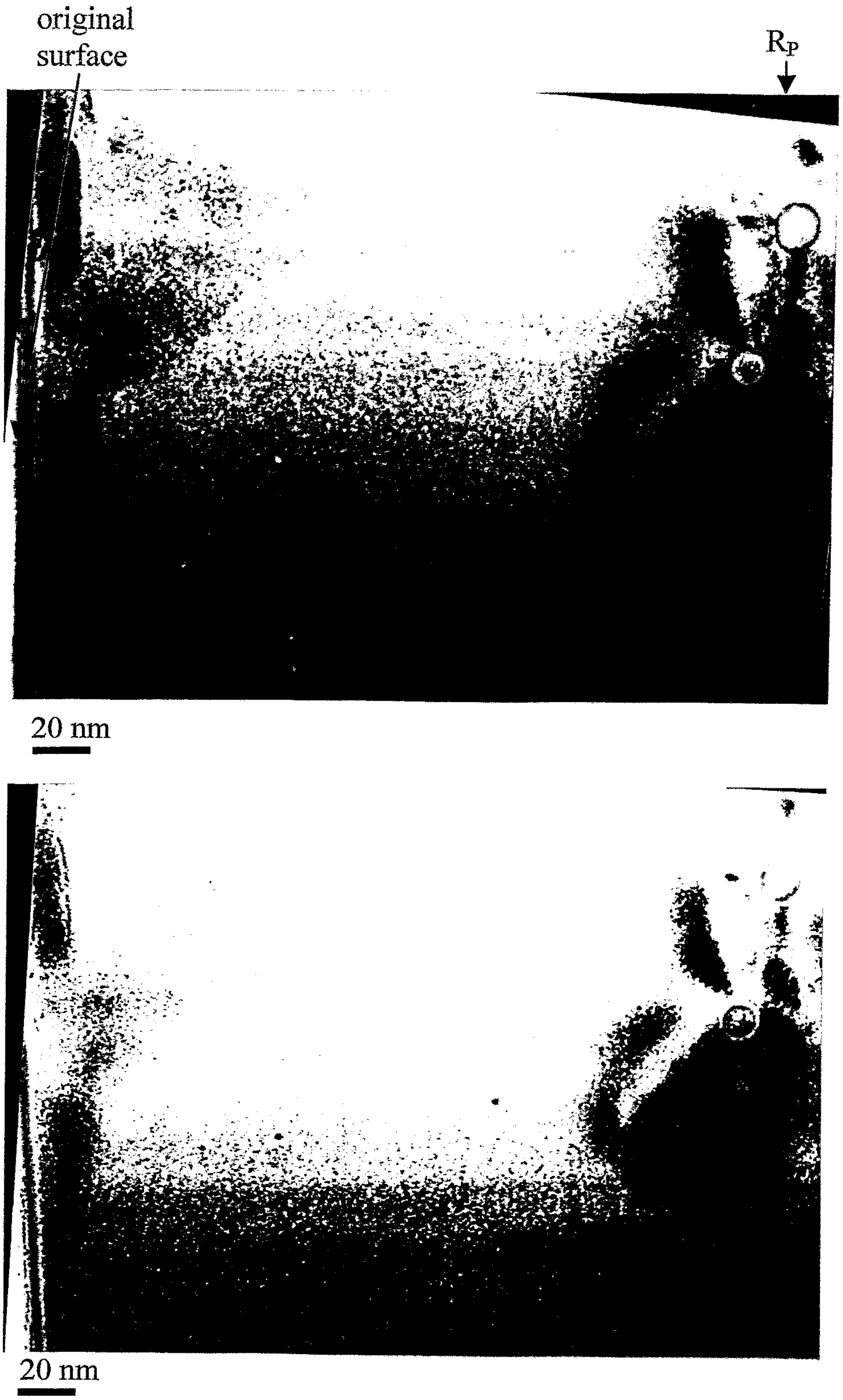

Fig. 4.35 XTEM bright field micrographs of a cleaved specimen of the sample implanted at 20 keV, 8×10^{15} He^+/cm^2, RT, random direction, contaminated by $1x10^{12}$ Cu^+/cm^2 after 800°C/10 min RTA. Kinematical conditions (a) underfocused; (b) overfocused

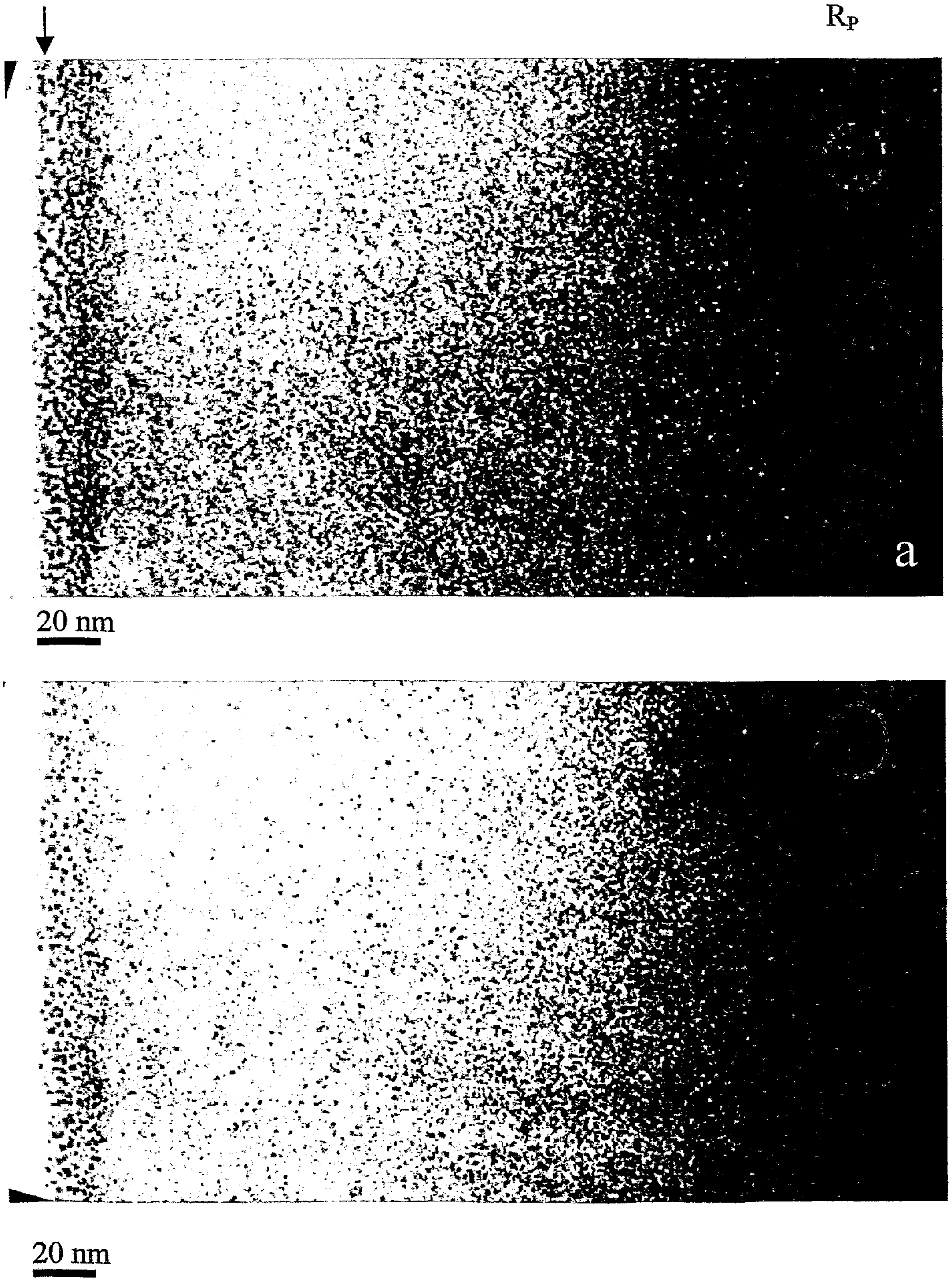

Fig. 4.36 XTEM bright field micrographs of a milled specimen of the sample implanted at 20 keV, 8×10^{15} He^+/cm^2, RT, random direction, contaminated by $1x10^{12}$ Cu^+/cm^2 after 800°C/10 min RTA. Kinematical conditions. (a) underfocused; (b) overfocused . Note the small ion milling introduced cavities appearing all over the specimen surface as white spots in (a) and dark spots in (b)

4.2.12 Determination of the crystal lattice deformation due to the He$^+$ implantation induced R$_p$/2 defects in Si

It was shown in the previous chapter that TEM is a powerful tool for the investigation of the microstructure of defects. In contrast to the TEM direct defect imaging, x-ray scattering under Bragg condition can give an average insight into the Si crystal lattice and its changes caused by the formation of defects. Compared to the perfect crystal, the defect induced changes in the diffraction pattern essentially can be: (a) a shift of the position of the Bragg peacks corresponding to the average change of the lattice parameter, (b) a broadening of the Bragg peaks due to a strain / lattice parameter fluctuation in the defect region, (c) a diffuse x-ray scattering background, that reflects the non-perfectly destructive interference between the Bragg peaks. The distribution of this diffuse scattering intensity contains very detailed information on the defects. A special region where the intensity of the x-ray diffuse scattering is relatively high is the region close to the Bragg reflection (Huang diffuse scattering).

For the further discussion it should be kept in mind that:

- in the kinematical scattering theory the intensity of scattered x-rays is proportional to the scattering volume;

- the real space and the diffraction pattern are connected to each other reciprocally: a small crystalline particle produces a broad diffraction line and vice versa.

Therefore, a perfect Si material with lattice defects due to He$^+$ implantation can reveal the following characteristic features in the x-ray diffraction line:

(1) the narrow and intense (central) peak of the large volume of the undisturbed perfect substrate;

(2) a very broad and low intense peak of x-rays scattered by the defects themselves;

(3) a diffuse peak (like tails to the substrate peak) of x-rays scattered in the disturbed Si volume surrounding the defects. As this volume is much larger than the intrinsic defect volume the intensity of the diffuse scattering is larger than the intensity scattered by the defect and located close to the substrate peak i.e. Huang scattering. It is

more promising to study small defects by means of diffuse scattering than by the genuine defect scattering. In this study the strain in the lattice in He^+ ion implanted Si caused by the $R_p/2$ defects is investigated by means of diffuse scattering.

Two samples were prepared:

1) One sample was chosen to reveal pronounced $R_p/2$ effect by means of metal gettering: Si(001) implanted with $8x10^{15}$ He^+ cm^{-2} at 40 keV and RTA annealed at 800°C for 10 min.
2) The sample is implanted as this one in 1) but additionally annealed at 800°C for 1 h in furnace. This sample does not reveal $R_p/2$ effect. The defects responsible for the Cu gettering are annealed during the nnealing cycle used (as discussed in Chapter 4.2.10).

In order to distinguish the lattice deformation caused by the $R_p/2$ layer from the one caused by the R_p layer a step etching of the samples was performed. A very slow etching procedure was used to keep the surface quality unchanged. First the samples were introduced into H_2SO_4/H_2O_2 (4/1) solution for 5 seconds at 120°C. During this procedure the surface is oxidised. The samples were further washed in distilled water and introduced in 10% of hydrofluoric acid in order to remove the oxide layer. In such a cycle a silicon layer with thickness ~ 8Å is removed from the surface. The procedure was repeated till the desired thickness was etched away. The etching rate was measure by RBS/C depth profiling using the dechanelling yield peak from R_p layer as a depth mark.

The (004) rocking curves were measured with a step size of 0.0001° or 0.001° in the range of ±0.15° or ±1.5° using a double crystal diffractometer with a sealed x-ray tube for Cu-Kα radiation.

In Fig. 4.37 the Si (004) rocking curves for 3 samples are shown: a non-etched RTA annealed sample containing the information for the whole damage region from the surface to the R_p layer; a 215 nm etched RTA annealed sample which contain the R_p layer but the main part of the $R_p/2$ layer was etched away, and a 600 nm etched RTA sample which does not contain any damage layer and correspond to unimplanted material.

The profile of all three rocking curves is symmetric around its centre. This indicates that the sample is in a thermally relaxed state. The profiles show tails with different intensity of the diffuse scattering, which is the result of the thermal vibrations of lattice atoms (thermal diffuse scattering TDS) and of lattice distortions due to small lattice defects.

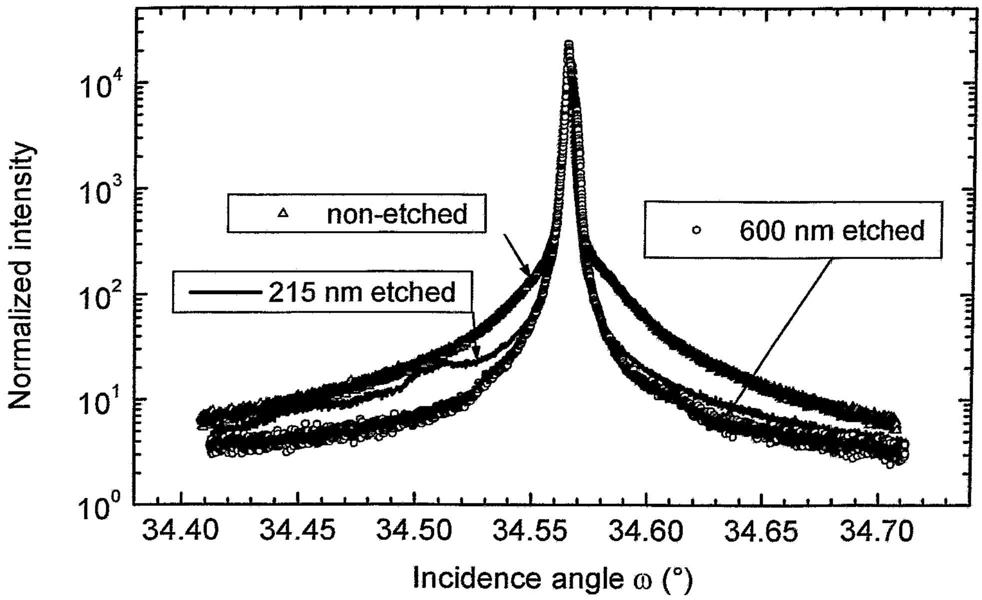

Fig. 4.37 The (004) rocking curves of the (001) Si sample implanted with $2x10^{16}$ He^+/cm^2 at 40 keV and RTA annealed at 800°C for 10 min

The sample without the implanted surface layer (600 nm crystal thickness is etched-off) has the lowest tail intensity. Its profile coincides with the profile of a perfect reference sample. Therefore, this intensity can be assumed as TDS which only depends on the temperature and is constant for all samples. The excess over TDS corresponds to X-ray intensity scattered by lattice defects. For comparison the measured curves are normalised to the same intensity at the highest measured angles (at the maximum distance from the central substrate peak). Fig. 4.38 shows the diffuse scattering by lattice defects of the non-etched sample, which is the difference of the diffuse intensities of the non-etched sample and the 600 nm etched sample (taken from Fig. 4.37), in logarithmic scale versus the deviation (θ-θ_{Bragg}) which is the incidence angle distance from the substrate peak also in logarithmic scale. The $(\theta-\theta_{Bragg})^{-2}$ dependence indicates Huang scattering of very small defect clusters. Their size can be estimate only if the $(\theta-\theta_{Bragg})^{-2}$ crosses a $(\theta-\theta_{Bragg})^{-4}$ dependence. As such crossing is not observed in the measuring range it can be concluded that the size of the defect clusters is smaller than 5 nm [Ehr94]. As it can be seen in Fig. 4.38 the intensity of the diffuse scattering for angles lower than θ_{Bragg} and for the angles higher than it is equal. This means that both kind of strain (compressive and tensile) are present in the sample, what may be correlated to the existence of both kind of small defect clusters, vacancy and interstitial type. Moreover, comparing the integral intensities of the diffuse scattering of the non-etched and the 215 nm etched samples (Fig. 4.37) one can conclude that 75% of the defective volume which causes strain in the lattice is located in the surface layer up to the depth of 215 nm. This is in the $R_P/2$ region of the sample (see Fig. 4.23)

The rocking curve of the 215 nm etched sample shows weak interference fringes at its low angle side what indicates the existence of a volume part with a mean distortion. Such fringes may be caused by a (41±3) nm thick layer located (75±2) nm below the surface of the etched sample with a crystal lattice expanded by (0.0035 ± 0.0002) as calculated using the computer code RCSim3.18A by P. Zaumseil [Zau98]. It correlates with the depth of the R_P defect layer. Such interference fringes are not detected in the profile of the non-etched sample most probably because of their masking by the diffuse scattering.

The rocking curves measured for the samples from the second type which were furnace annealed are presented in Fig. 4.39. The results for the FA samples which does not reveal $R_P/2$ effect in means of Cu gettering, surprisingly show similar diffuse scattering as the RTA annealed samples. The diffuse scattering intensity as a function of the deviation (θ-θ_{Bragg}) indicates Huang scattering from small defect clusters. The comparison of the scattering intensities of the non-etched and the 215 nm etched samples (Fig. 4.38) show that 50% of the damage volume is located in the surface layer up to the depth of 215 nm (compared to the value of 75% in the RTA annealed samples which show $R_P/2$ gettering). The results for the furnace annealed sample (which by means of TEM is free of defects in the $R_P/2$ area (Fig. 4.34b)) show that a significant part of the damage is still present in this

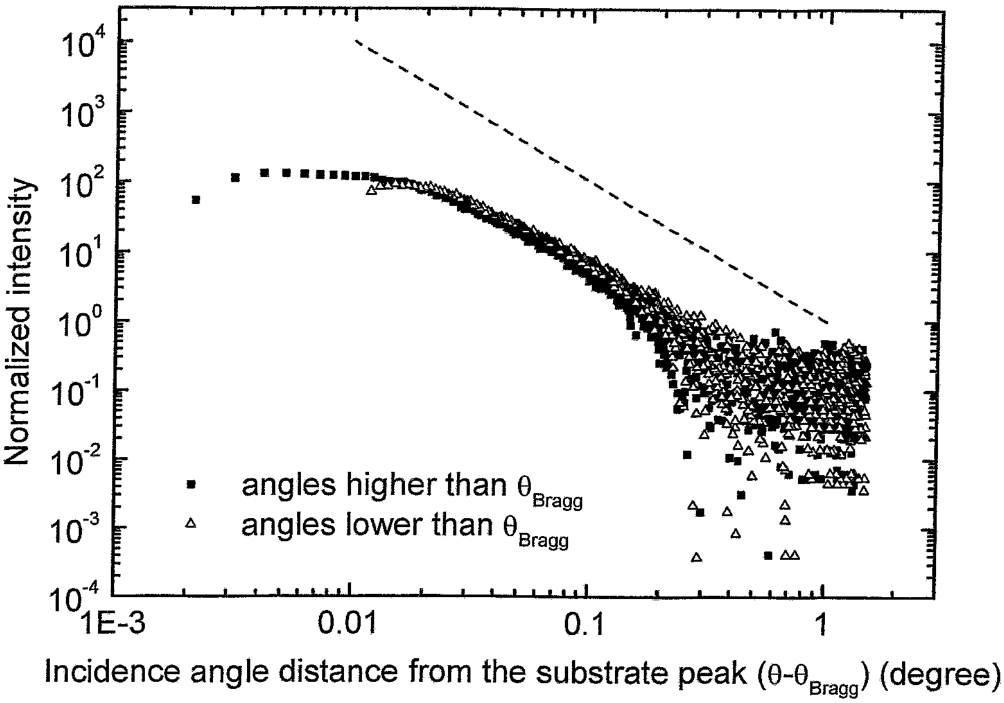

Fig. 4.38 Diffuse scattering intensity as a function of the deviation (θ-θ_{Bragg}) from the (004) reflection. The $(\theta$-$\theta_{Bragg})^{-2}$ law indicates Huang scattering from small defect clusters. The line, showing the theoretical dependence $(\theta$-$\theta_{Bragg})^{-2}$, was drawn to guide the eyes.

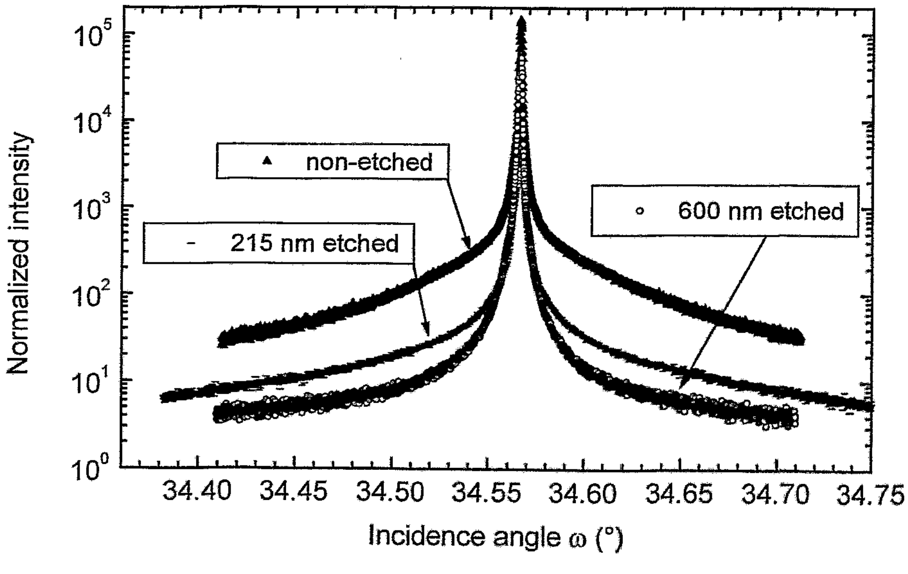

Fig. 4.39 The (004) rocking curves of the (001) Si sample implanted with $1x10^{16}$ He^{+}/cm^{2} at 40 keV and FA annealed at 800°C for 1 hour.

region. This is an indication for a presence of small defects at *$R_P/2$*, which are not observable by TEM. These residual defects are not gettering centres for Cu, as the SIMS Cu profiling in that case does not show any $R_P/2$ peak (Fig. 4.33).

Table IV.III summarise all the results of the experiments presented in Chapter 4.2. There are quoted for each implantation and annealing conditions the peak positions of the corresponding Cu depth profile as obtained from SIMS experiments. In addition the characteristics of the damage are also shown, the region where it is located as well as the mean size of the He cavities.

A general remark to all gettering studies reported in Chapter 4.2 is that the Cu gettering at $R_P/2$ has been found to be independent of the way of introducing Cu, simultaneously or subsequently to the damage annealing. This means that the presence of Cu does not play an important role for the defect evolution at $R_P/2$ during annealing.

Anneal	Energy (keV)	Fluence (cm^{-2})	IT (°C)	Impl. direction	Depth of $R_p/2$ peak position (µm)	Depth of R_p peak position (µm)	Cavity mean diameter (nm)	
800°C 10 min RTA (Ar)	40	TD	RT	random		0.38	10	24
		LD	RT	channeling	0.25	0.5	10	25
				random	0.2	0.4	11	21
			HT	channeling		0.45	9	
				random		0.35	9	
		HD	RT	channeling	0.25	0.45	13	
				random	0.2	0.35	11	
			HT	channeling		0.45	14	
				random		0.35	12	
	20	LD	RT	random	0.12	0.26	7	20
800°C/1h FA (Ar)	40	LD	RT	random		0.4		

Table IV.III Depth of the $R_p/2$ and R_p peak positions and the cavity mean diameter for each implantation and annealing condition

Chapter 5

Discussion

5.1 Gettering ability of the nanocavities in the $R_P/2$ region

The nanocavities in the $R_P/2$ region visualised in the cleaved TEM specimens are assumed to be agglomerates of implantation-generated excess vacancies formed during annealing. For the 3.5 MeV Si^+ ion implantation into Si to the fluence of 5×10^{15} cm^{-2}, the predicted amount of excess vacancies is about 6.4×10^{14} cm^{-2} and their maximum concentration is 7.6×10^{18} cm^{-3}. The concentration of the nanocavities c_v visualised in the cleaved TEM specimen (Fig. 4.10) can be estimated to be $c_{cav} = 1.3\times10^{15}$ cm^{-3}, taking into account the TEM specimen thickness of about 60 nm. The nanocavity total volume is $Vc = 580\times10^{-21}$ cm^3 corresponding to a monovacancy concentration of $c_v = 5.9\times10^{18}$ cm^{-3}, which is in a very good agreement with the above prediction of the maximum concentration of the excess vacancies.

If Cu atoms are chemisorbed in one monolayer on the inner walls the gettering capability of the $R_P/2$ layer is limited. For He^+ implantation generated cavities into Si a saturation value of 6.5 Cu atoms/nm^2 on the inner walls of the cavities has been determined [Mye-96]. Using this value the maximum concentration of Cu gettered at $R_P/2$ can be estimated to be $c_{Cu\ max} = 8.6\times10^{17}$ Cu/cm^3. This value is in good agreement with the SIMS experimental data showing the peak Cu concentration at $R_P/2$ always in the same order of magnitude (Fig. 4.11a).

5.2 Effects of metal contamination on the visualisation of nanocavities

It has been demonstrated in Chapter 4.1.1.3 that Ar^+ milling induced nanocavities covering the TEM specimen may disturb the observation of a defect structure which consists of nanocavities. This undesired effect can be avoided by the cleaving of the TEM specimen. It is worthwhile to point out that in this work the Cu content in the samples is restricted to a level that Cu acts exclusively as a tracer without changing the defect structure (see Chapter 2.4). Therefore, the presence of Cu in the sample plays no role for the visualisation of cavities at $R_P/2$. The samples implanted and annealed under the same conditions, one contaminated with Cu and the other not, both reveal cavities at $R_P/2$ by means of TEM. This means that the visualisation of the cavities at $R_P/2$ is not metal related when the XTEM samples are cleaved. This fact differs to results reported by Venezia et al.[Ven98] and Kalyanaraman at al.[Kal00, Kal01] where gold was introduced in the samples to very high fluences (~ 10^{16} at/cm at 30÷50 keV) on the front side of the wafer after the MeV implantation and distributed through the wafer during the subsequent anneal. There are two points to be noted: (1) The metal implantation performed on the front side of the wafer causes damage in the same region where the defect recombination caused by the MeV implantation is investigated, from the surface to R_P. The damage caused by the Au implant was found to amorphise a layer around the R_P of the Au implant in the as-implanted state of the sample [W-Leu95a]. The presence of this damage was assumed not to influence the recombination of the MeV implantaton induced defects during annealing. This assumption needs to be proved. (2) The cavities at $R_P/2$ were visualised by TEM *only* by the means of the Z-contrast on the cavity walls caused by the Au decoration. Imaging of cavities at $R_P/2$ in the samples where Au was not implanted to a very high fluences (mentioned above) was never reported. Moreover, the amount of Au at $R_P/2$ was found to exceed the monolayer coverage on cavity walls and excess Au has precipitated and completely filled some cavities. In that way a new phase is formed in the damage region, presumably a silicide that also could influence the recombination of the MeV implantation induced defects which needed to be investigated. The results presented in this study show promise for visualising vacancy type defects at $R_P/2$ without a need of any metal decoration.

5.3 Comparison of the keV He^+ ion implantation induced $R_P/2$ effect with MeV Si^+ ion implantation induced $R_P/2$ effect

In this section the possible reasons for the appearance of the $R_p/2$ effect generated by He^+ ion implants will be discussed. The defect production and recombination during ion implantation and subsequent annealing for the case of MeV implantation of Si^+ ions and for the case of keV implantation of He at random direction will be compared.

5.3.1 Predictions from ballistic models

As discussed in details in Chapter 4.1, for the MeV implantation of heavy ions, the $R_p/2$ gettering effect is attributed to the formation of excess vacancies at the $R_p/2$ region. The assumption of a complete local vacancy-interstitial annihilation during annealing leads to the following results: (i) the formation of a vacancy-rich layer from the surface nearly up to R_p and (ii) the formation of an interstitial-rich region slightly extended beyond the R_p depth (with the maximum concentration of excess interstitials at about 1.2 R_p). For 3.5 MeV Si^+ random implant into Si, for example, TRIM/98 calculations provide a ratio of $V_E = 0.182$ excess vacancies per implanted Si^+ ion located within the surface and the R_p depth. The same calculations performed for 40 keV He^+ implant into Si result in an amount of $V_E = 0.015$ excess vacancies per implanted He^+ ion. Hence, the excess vacancy generation per implanted He^+ ion at the $R_p/2$ region is more than 10 times lower than for the MeV Si^+ implant. However, it is important to note that the vacancy-rich region produced by the 3.5 MeV Si^+ ions extends from the surface to the junction depth $x_j \approx 2.25 \mu m$. In contrast, the corresponding region for the 40 keV He^+ random implant extends from the surface to $x_j \approx 0.35 \mu m$. As a consequence, the average number of excess vacancies per depth interval α ($\alpha = V_E / x_j$) for the Si and He cases are $\alpha_{Si} = 8.10 \times 10^{-6}$ excess-vacancies/ion/Å and $\alpha_{He} = 4.37 \times 10^{-6}$ excess-vacancies/ion/Å, which renders a ratio $\alpha_{He}/\alpha_{Si} \approx 0.5$. Considering the typical implanted fluences of $\phi_{Si} \approx 0.5 \times 10^{16}$ cm^{-2} and $\phi_{He} \approx 0.8 \times 10^{16}$ cm^{-2} one obtains a ratio for the effective excess vacancy concentrations of $\alpha_{He}\,\phi_{He}/\alpha_{Si}\,\phi_{Si} \approx 0.8$ for the random implant case. From these arguments in can be concluded that it is not the total number of excess vacancies (i.e the ion-implantation induced damage) itself which is important for the appearance of the $R_P/2$ effect but the average number of excess vacancies per depth interval, excess vacancy concentration, α. The channelling experiment also supports the idea that the ion-implantation induced damage is not the main factor for the appearance of the $R_P/2$ effect. Although the damage at $R_P/2$ caused by the channelling implantation is one order of magnitude lower than the one caused by the random implantation (Fig. 4.23) the $R_P/2$ effect appears for both implantation conditions.

Table IV.IV summarises the results of the TRIM calculations for the different He and Si ion implantations for which the $R_P/2$ effect appears. A similar value of the excess vacancy concentration α, calculated for the 20 keV He^+ ion implant supports the above conclusion of that α as a dominating factor for the appearance of the $R_P/2$ effect.

The results presented in this chapter support the idea that the damage production during implantation is not important, but the excess vacancy concentration is the main factor for the appearance of the $R_P/2$ effect.

Ion	***E*, keV**	**ϕ, cm^{-2}**	**x_j**	**V_E/ion**	**α, V_E/cm^3**
Si	3500	0.5×10^{16}	2.25	0.1820	4.05×10^{18}
He	40	0.8×10^{16}	0.35	0.0153	3.50×10^{18}
He	20	0.8×10^{16}	0.20	0.0085	3.40×10^{18}

Table IV.IV Comparison of the width of the excess vacancy determined by the junction depth x_j, the number of the excess vacancies per implanted ion V_E /ion and the effective excess vacancy concentration α for the Si and the He implants for the typical fluences ϕ for the appearance of the $R_P/2$ effect.

5.3.2 Processes which take place during annealing

Here is the point where one significant difference between the Si implant and the He implant must be taken into consideration: the defect structure in the R_p region after annealing. In the case of Si implantation the R_p region consists of extended defects (dislocation loops) with pure interstitial character. The excess silicon interstitials generated during the implantation process in this region plus the implanted ions themselves form these defects. When considering the He^+ ion implantation one has also to take into account the cavity formation and evolution (discussed in Chapter 4.2.1). He atoms are known to be trapped by divacancies stabilising them and favouring their evolution into more complex He-V clusters during annealing [Ala92, Est97]. This results in accumulation and stabilisation of vacancies in the R_p region contrary to what happens in the case of the Si implant into Si. The excess vacancy model discussed above predicts $V_E.\phi = 1.5\times10^{14}$ cm^{-2} excess vacancies in the R_p /2 region for the case of He implant to the fluence $\phi = 0.8\times10^{16}$ cm^{-2}. Using the plan-view TEM analyses (not shown) it was estimated that in this case the number of vacancies trapped in the cavities at R_p is $\approx 2\times10^{15}$ cm^{-2}, a number which is one order of magnitude higher than the number of the calculated excess vacancies. Hence the equal number of displaced Si atoms was generated and not recombined with vacancies during the annealing. This implies that local defect recombination is incomplete under the annealing conditions used. While the vacancies remain trapped in the cavities at R_p, at the same time self-interstitials migrate and recombine elsewhere during annealing. They are trapped in the radiation damage close to the cavities (as observed in TEM) and at the silicon surface. Recent studies report on the measurable swelling of the sample surface caused by the Si recoils recombining there after annealing at temperatures between 200°C and 1200°C [Fuk99, Rai00]. It cannot be excluded that a part of these silicon interstitials also contribute to the defect structure at R_p/2 at the annealing conditions used in this study. The presented X-ray measurements support this hypotheses as the equal intensity of the diffuse scattering in both slopes of the Bragg peak could indicate the presence of both type of small defect clusters in the samples, vacancy and interstitial type, both of them are mainly located in the R_P/2 layer (as it was demonstrated in Fig. 4.37). Nevertheless that small interstitial clusters could be also present at R_P/2, the cavities therein, observed in the XTEM cleaved samples (Fig. 4.8), must be the gettering centres for Cu as with their disappearance the Cu gettering at R_P/2 is also lost (Fig. 4.33 and 4.34).

The absence of Cu gettering at R_p/2 for the HT implantation is ascribed to the damage annealing that occurs during the implantation process. The vacancies and the interstitials have longer mean free path during the HT implantation. This means that the defect recombination during the HT implantation will be enhanced. From the plan view TEM analyses (not shown), it was estimated the total cavity volume in terms of Si atoms displaced in order to open space for the cavity formation. An amount of $\approx 4\times10^{14}$ at./cm^2 for the case of 40 keV HT implant to the fluence of 1×10^{16} He$^+$/cm^2 (Fig. 4.25b) was estimated. This value is 5 times lower than the one calculated for the corresponding RT implant (Fig. 4.25a) for which the total cavity volume is $\approx 2\times10^{15}$ cm^{-2} (discussed above). This confirms the enhanced point defect recombination during implantation in the case of the HT implant.

Chapter 6

Summary

The phenomenon named $R_P/2$ effect describes the effect of metals and oxygen gettering at the depth of approximately $R_P/2$ of the MeV heavy ion implanted and annealed Si. The gettering centres for metals at $R_P/2$ were not observed by TEM or other structural analyses techniques. They were considered to be too small to be visible by TEM. Some indirect methods were used to monitor the presence of $R_P/2$ defects. The ballistic models predict special separation of the vacancies and the interstitials created during ion implantation process. There are two different explanations proposed for the existence of the $R_p/2$ effect. The first explanation is based on the assumption that a full local vacancy-interstitial recombination takes place during annealing. Under this assumption vacancies are supposed to remain in the region from the surface up to about R_P after subsequent annealing. It was suggested that the remaining vacancies are the origin of the defects responsible for the metal gettering at $R_P/2$. The second proposed explanation for the existence of defects in the $R_P/2$ region assumes that during the annealing the implantation induced defects do not annihilate locally. There could be remains from both kind of defects, vacancies and interstitials that can agglomerate during annealing and form interstitial type defects as well as vacancy type defects that can co-exist in the $R_P/2$ region. The nature of the defects acting as gettering centres for impurities in the $R_P/2$ region was not undoubtfully proved so far.

In this work, nanocavities at $R_P/2$ are observed directly by TEM analysis. The evolution of these vacancy-type defects at $R_P/2$ for samples that are MeV implanted and annealed under typical conditions for appearance of $R_P/2$ (implantation : 3.5 MeV, $Si^+ \rightarrow Si$, $\phi = 0.5\times10^{16}$ cm^{-2}; annealing: 800 – 900°C) was investigated.

The crucial point for visualisation of the vacancy type defects at $R_P/2$ is the XTEM specimen preparation technique. Only the samples prepared by cleaving reveal cavities at $R_P/2$. Minimum damage production caused during the preparation of the TEM specimen using cleaving allows the imaging of the cavities at $R_P/2$. On the other hand the use of the conventional and the low angle ion milling techniques for TEM specimen preparation leads to a completely different defect structure visible at $R_P/2$: not vacancy type but interstitial loops were found therein. The conventional ion milling process, which is the final procedure of the TEM specimen sample preparation, generates these interstitial loops. The TEM sample preparation induced defects loops are found only in the $R_P/2$ region of the samples showing $R_P/2$ gettering effect. Their generation does not depend on the presence of metal in the sample or on the concentration of the impurities in the substrate. The formation of interstitial loops gives evidence supporting the hypothesis of a co-existence of small interstitial clusters in the same region where the cavities are observed.

It must be pointed out that the widely used conventional ion milling systems explored under standard conditions can introduce significant modifications on the defect structure of the samples. Not only interstitial loops at $R_P/2$ but also nanocavities were generated during the ion milling process. In contrast to the growth of the interstitial loops at $R_P/2$, the generation of the nanocavities is not connected to the presence of the original $R_P/2$ defects in the sample. The nanocavities are found to cover the surface of the milled XTEM specimens even in the unimplanted areas. The ion milling introduced cavities are found to be bigger in the thinnest parts of the TEM specimen. Their presence not only prevents from visualising the original cavities at $R_P/2$, but confuses the TEM analysis - especially in cases where the defect structure to be investigated consists of cavities.

The present study proves that the excess vacancies are the origin of the metal gettering at $R_P/2$ of the MeV Si^+ ion implanted and annealed Si, nevertheless the possibility of co-existence of a small proportion of interstitial type defects in the same region. The relationship between the excess vacancy generation and Cu gettering was demonstrated by implantation at inclined incidence with respect to the sample surface. It was experimentally shown that for incidence angle of 55° the $R_P/2$ gettering disappears. This finding is in agreement with the performed ballistic calculations. They predict that the depth separation of the vacancy and the interstitial profile is not so pronounced for ion implantation at inclined incidence as for ion implantation at perpendicular incidence. This leads to enhanced vacancy-interstitial recombination during annealing in the case of inclined incidence implantation. The use of inclined incidence implantation is a way to inhibit the creation of vacancy-type defects at $R_P/2$ during annealing.

It was shown that the impurity trapping at $R_P/2$ could be prevented also by means of additional Si^+ ion implantations into the vacancy-rich region of MeV ion-implanted Si. The additional implanted ions act as self-interstitials and recombine with the excess vacancies. Variation of the parameters of the additional Si^+ ion implantations was used in order to monitor the exact location of the excess vacancies by Cu gettering. The threshold fluence of the additional Si^+ implants necessary to recombine with the gettering centres for Cu at $R_P/2$ is determined to be about 50% of the calculated excess vacancies. Above this threshold fluence interstitial-type dislocation loops form in the defect recombination zone. The gettering ability of these new interstitial defects is negligible compared to the gettering ability of the nanocavities.

The contribution of a fraction of the excess-interstitials at R_P to the defect recombination in the $R_P/2$ was proven. Part of the interstitials at R_P diffuses a limited distance towards to the surface and recombines there with the excess-vacancies.

For low energy He^+ ion implants in Si, Cu gettering appears at both: the R_p and $R_p/2$ region during annealing at relatively high temperatures (800-900°C). It was shown by the ballistic considerations that the damage production is not important for the appearance of the $R_p/2$ effect. This was also experimentally supported as the $R_P/2$ effect was found to be independent of the damage production during ion implantation as the $R_P/2$ effect appears for both conditions, random and <100> channeled direction (with a difference of the damage production at $R_P/2$ of about one order of magnitude between the random and the channeled case) as well as for implantations of ions with big differences in the ion mass, (He^+ and Si^+) implanted in a huge energy range (from keV to MeV).

As in the case of MeV Si^+ ion implanted and annealed Si, the TEM analyses of the cleaved He^+ ion implanted and annealed specimens show nanocavities at $R_p/2$. These nanocavities are proposed to be the gettering centres for Cu at $R_p/2$ as with their disappearance the Cu gettering at $R_P/2$ also disappears.

Whenever He was implanted at RT, the $R_p/2$ effect was observed. However HT implants led to the disappearance of the Cu peak in the $R_p/2$ region. This feature is attributed to the enhanced defect recombination in the damage region during the implantation. The longer mean free path of the vacancies and the interstitials during the HT implantation leads to a higher degree of recombination at the surface and the R_P region compared to the RT implantation case.

The He^+ ion implantation induced $R_p/2$ effect is explained by the radiation-induced defects, and in connection with the point defect fluxes associated with the formation of the He cavities. It was found that a peak He concentration (between 2.7 and 3.5×10^{20} He^+/cm^3) is necessary for the appearance of a gettering defect layer at $R_p/2$. This corresponds to the excess vacancy concentration between 2.6 and 3.5×10^{18} vacancies/cm^3.

It was shown by the comparison of the experimental results for the MeV Si^+ ion implantation and the keV He^+ implantation, as well as by the comparison of the ballistic calculations for these two implantations, that the basic mechanism for the appearance of the $R_P/2$ effect is the same for the He^+ and the Si^+ ion implantation. The same model can be used for the description of the effect. It was found out that ***the excess vacancy concentration is the main factor for the appearance of the $R_P/2$ effect.*** The last finding verify that the $R_P/2$ effect is not an effect attributed only to the MeV ion implantations of heavy ions but it is a general effect of the ion implantation process.

Ion implantation continues to be the selective doping technique of choice in silicon integrated circuit manufacturing, and its applications continue to grow in doping and damage gettering. However, in both technology and manufacturing equipment development there is a rapidly increasing need to understand in detail the dependence of implant-induced damage profiles in silicon on all key implant and annealing parameters. These reasons include largely reduced thermal budgets in integrated circuits processing. As it was shown in this study, the presence of the $R_P/2$ defects after low thermal budget anneals is a common feature in the ion implanted Si substrates and needs to be considered in the semiconductor technology. A promising result of the investigations presented in this thesis is the possibility to control the appearance of the $R_P/2$ effect by additional silicon self-implantations or by implantations performed at inclined angle with respect to the Si substrate surface. This defect engineering could be important for the further applicability of the MeV ion implantation in the proximity gettering technology in the conditions of reduced thermal budgets in manufacturing. On the other hand the nanocavities in the $R_P/2$ region could be used as a source of vacancies. Such a vacancy source with a controlled concentration and depth position could be useful for many applications like for instance the suppression of the TED of low energy B^+ implants in Silicon. Such a method could give a future to the ion implantation to be a selective doping technique for the realization of ultrashallow junctions for the semiconductor technology.

REFERENCES

[Aga96] A. Agarwal, K. Christensen, D. Venables, D.M. Maher and G. Rozgonyi, Appl. Phys. Lett. **69** (1996) 3899

[Ala92] A. Alatalo, M. J. Puska and R. M. Nieminen, Phys. Rev. B **46** (1992) 12806

[Apel94] M. Apel, I. Hanke, R. Schindler and W. Schröter, J. Appl. Phys. **76** (1994) 4432

[Ben96] J.L. Benton, P.A. Stolk, D.J. Eaglesham, D.C. Jacobson, J.Y. Chang, J.M. Poate, N.T. Há, T.E. Heynes and S.M. Myers. J. Appl. Phys. **80** (1996) 3275.

[Ben97] J. L. Benton, S. Libertino, P. Kringhoj, D. J. Eaglesham, J. M. Poate and S. Coffa. J. Appl. Phys. **82** (1997) 120

[Behrisch] [Ber81] R. Behrisch, Physical Sputtering of Single-Element Solids, Sputtering by Particle Bombardment I (Springer-Verlag Berlin Heidelberg 1981)

[Bier80] J. B. Biersack and L. G. Haggmark, Nucl. Inst. and Meth. Phys. Res. B **174** (1980) 257

[Bor95] A. Borghesi, B. Pivac, A. Sassella and A. Stella, J. Appl. Phys. **77** (1995) 4169

[Bro98] R.A. Brown, O. Kononchuk, G.A. Rozgonyi, S. Koveshnikov, A.P. Knights, P.J. Simpson and F. Gonzalez, J. Appl. Phys. **84** (1998) 2459

[Caf91] J. P. McCaffrey. Ultramicroscopy **38** (1991) 149

[Car98] J. Cardenas, B.G. Svensson, W.-X. Ni, K.B. Joelsson, G.V. Hansson. Appl. Phys. Lett. **73** (1998) 3088.

[Cer00] G.F. Cerofolini, F. Corni, S. Frabboni, C. Nobili, G. Ottavini, R. Tonini, Mat. Sci. Engng. 27 (2000) 1

[Che89] N.W. Cheung, C.L. Liang, B.K. Liew, R.H. Mutikainen and H. Wong, Nucl. Instrum. Methods Phys. Res. B **37/38** (1989) 941

[Chu78] W-K. Chu, J. W. Mayer, M- A. Nicolet. Backscattering Spectrometry, Academic Press, New York, (1978)

[Cof00] S. Coffa, S. Libertino and C. Spinella. Appl. Phys. Lett. **76** (2000) 321

[Cow99] N.E.B. Cowern, G. Mannino, P.A. Stolk, F. Roozeboom, H.G.A. Huizing and J.G.M. Berkum, Phys. Rev. Lett. **82** (1999) 4460

[Cri87] C. C. Criffioen, J. H. Evans, P. C. de Jong and V. van Veen, Nucl. Instrum. and Meth. B **27** (1987) 417

[Eag97] D.J. Eaglesham, T. E. Haynes, H.-J. Gossmann, D.C. Jacobson, P.A. Stolk and J.M. Poate, Appl. Phys. Lett. 70, (1997) 3281

[Edin76] J. W. Edington. Practical Electron Microscopy in Materials Science, N. V. Philips' Gloeilampenfabrieken, Eindhoven (1976).

[Ehr94] P. Ehrhart, J. of Nucl. Materials **216** (1994) 170

[Est97] S. K. Estreicher, J. Weber, A. Derecskei-Kovacs and D. S. Marynick, Phys. Rev. B **55**, (1997), 5037

[Fal97] R. Falster, M. Pagani, D. Gambaro, M. Cornara, M. Olmo, G. Ferrero, P. Pichler and M. Jacob, Solid. State Phenom. 57-58 (1997)129

[Fed99] L. Fedina, A. Gutakovskii, A. Aseev, J. Van Landuyt and J. Vanhellemont, Phys. Stat. Sol (a) **171** (1999) 147

[Fin88] D. Fink, Raddiation Effects **106** (1988) 231

[Fich00] P. F. P. Fichtner, A. Peeva, M. Behar, G. de M. Azevedo, R. L. Maltez, R. Koegler and W. Skorupa, Nucl. Instrum. Meth. Phys. Res. B **161-163**, (2000) 1038

[Fuk99] W. Fukarek and J. Kaschny, J. Appl. Phys. **86,** (1999) 4160

[Gill90a] D. Gilles, E.R. Weber and S.-K. Hahn, Phys. Rev. Lett. **64** (1990) 196

[Gill90b] D. Gilles, W. Schröter and W. Bergholz, Phys. Rev. B **41** (1990) 5770

[Gös91] U.M. Gösele, T.Y. Tan, in electronic Structure and Properties of Semiconductors, edited by W. Schröter, Materials Science and Technology Vol. 4 (VCH, New York, 1991) 197-247

[Hei99] K.-H. Heinig and H.-U. Jaeger. Proc. of 1st ENDEASD workshop Santorini/Greece, (edited by C. Claeys, April 1999) 297

[Holl93] O. W. Holland, D. S. Zhou and D. K. Thomas, Appl. Phys. Lett. **63** (1993) 896.

[Holl95] O.W. Holland, D.K. Thomas and D.S. Zhou, Appl. Phys. Lett. **66**, (1995) 1892

[Holl96] O.W. Holland, L. Xie, B. Nielsen and D.S. Zhou. J. Electronic Mat. **25,** (1996) 99

[Hug98] S.A. McHugo, R.J. McDonald, A.R. Smith, D.L. Hurley and E.R. Weber, Appl. Phys. Lett. **73** (1998) 1424

[Ista98] A.A. Istratov, C. Flink, H. Hieslmair, E.R. Weber and T. Heiser, Phys. Rev. Lett. **81** (1998) 1243

[Kasch97] J.R. Kaschny, P.F.P. Fichtner, A. Muecklich, U. Kreissig, R.A. Yankov, R. Koegler, A.B. Danilin and W. Skorupa, Mater. Res. Soc. Symp. Proc. Vol. **469**, (1997) 451

[Kal00] R. Kalyanaraman, T.E. Haynes, V.C. Venezia, D.C.Jacobson, H.-J. Gossmann, C.S. Rafferty, Appl. Phys. Lett. **76** (2000) 3379

[Kal01a] R. Kalyanaraman, T.E. Haynes, M. Yoon, B.C. Larson, D.C. Jacobson, H.-J. Gossmann and C.S. Rafferty, Nucl. Instrum. Meth. Phys. B **175-177** (2001) 182

[Kal01b] R. Kalyanaraman, T.E. Haynes, O.W. Holland, H. –J. L. Gossmann, C. S. Rafferty and G. H. Gilmer, Appl. Phys. Lett. 79 (2001) 1983

[Kei98] D. Keith Bowen and B. K. Tanner, High Resolution X-ray Diffractometry and Topography, Taylor & Francis Ltd, 1998

[Kin97] A. Kinomura, J. S. Williams, J. Wong-Leung and M. Petravic, Nucl. Instrum. Meth. **B 127/128** (1997) 297

[Kon96] O. Kononchuk, R.A. Brown, Z. Radzimski, G.A. Rozgonyi, F. Gonzalez, Appl. Phys. Lett. 69 (1996) 4203

[Kon97] O. Kononchuk, R.A. Brown, S. Koveshnikov, K. Beaman, F. Gonzalez and G.A. Rozgonyi, Solid State Phenomena **57-58**, (1997) 69

[Kov98a] S. V. Koveshnikov and G. A. Rozgonyi, J. Appl. Phys. **84** (1998) 3078

[Kov98b] S. Koveshnikov and O. Kononchuk. Appl. Phys. Lett. **73**, (1998). 2340

[Kög98] .R. Koegler, D. Panknin, W. Skorupa, P. Werner and A. Danilin, Proceedings of the conference „Ion Implantation Technology 96" p. 679

[Kög99a] R. Kögler, R.A. Yankov, M. Posselt, A.B. Danilin and W. Skorupa, Nucl. Instrum. and Meth. B **147** (1999) 96.

[Kög99b] R. Kögler, A. Peeva, W. Anwand, G. Brauer and W. Skorupa, Appl. Phys. Lett. **75**, (1999) 1279

[Kra00] R. Krause-Rehberg, F. Börner and F. Redmann, Appl. Phys. Lett 77, 3932 (2000)

[Kur93] Kuroi, Y. Kawasaki, S. Komori, K. Fukumoto, M. Inuishi, K. Tsukamoto, H. Shinyashiki, T. Shingyoji, Jap. J. Appl. Phys. **32** (1993) 303.

[Mes94] A. Mesli and T. Heiser, Mater. Sci. Enging. B 25 (1994) 141

[Moh95] B. Mohadjeri, J. S. Williams and J. Wong-Leung, Appl. Phys. Lett. 66, (1995), 1889

[Mye95]S. M. Myers, H. J. Stein and D. M. Follstaedt, Phys. Rev. B **51**, 9742 (1995)

[Mye96] S. M. Myers and D. M. Follstaedt, J. Appl. Phys. **79** (1996) 1337

[Mye98] S. M. Myers and G. A. Petersen, Phys. Rev. B **57**, (1998) 7015

[Pell01] P. Pellegrino, P. Leveque, J. Wong-Leung, C. Jagadish and B.G. Svensson, Appl. Phys. Lett. **78** (2001) 3442

[Pos] M. Posselt and A. Lebedev, unpublished results

[Rai95] V. Raineri, P. G. Fallica, G. Percolla, A. Battaglia, M. Barbagallo and S. U. Campisano, J. Appl. Phys. **78** (1995) 3727

[Rai97] V. Raineri, Solid State Phenomena, **57-58**, (1997) 43

[Rai00] V. Raineri, M. Saggion and E. Rimini, J. Mater. Res. **15,** (2000) 1449

[Rei97] L. Reimer. Transmission Electron Microscopy, 4th Edition, Springer – Verlag Berlin Heidelberg (1997)

[Rim98] E. Rimini, S. Coffa, S. Libertino, G. Mannino, F. Priolo and V. Privitera, Defect and Diffusion Forum **153-155**, (1998) 137

[roadmap] *The National Roadmap for Semiconductors* (Semiconductor Industry Association, San Jose, CA, 1997)

[Rob90] M. T. Robinson, Nucl. Instrum. Methods Phys. Res. B **48**, 408 (1990).

[Rob00] L. S. Robertson, K. S. Jones, L. M. Rubin and J. Jackson. J. Appl. Phys. **87** (2000) 2910

[Roz00] G.A. Rozgonyi, J.M. Glasko, K.L. Beaman and S.V. Koveshnikov, Mat. Sci. and Eng. B72 (2000) 87

[Sei98] M. Seibt, H. Hedemann, A.A. Istratov, F. Riedel, A. Sattler and W. Schröter, Phys. Status Solidi A **166** (1998) 171

[Saw90] W. D. Sawyer, J. Weber, G. Nabert, J. Schmälzlin and H.-U. Habermeier, J. Appl. Phys. **68** (1990) 6179

[Schre91] R. J. Schreutelkamp, J.S. Custer, J.R. Liefting, W. X. Lu and F. W. Saris, Mat. Sci. Reports, Vol. 6, No. 7/8 (1991) 311

[Schrö91] W. Schroter, M. Seibt, D. Gilles, in electronic Structure and Properties of Semiconductors, edited by W. Schröter, Materials Science and Technology Vol. 4 (VCH, New York, 1991) 539-589

[Str01a] B. Stritzker, M. Petravic, J. Wong-Leung, J.S. Williams, Nucl. Instrum. Meth. Res. B **175-177** (2001)154

[Str01b] B. Stritzker, M. Petravic, J. Wong-Leung, J.S. Williams, Appl. Phys. Lett. **78** (2001) 2682

[Tam91] M. Tamura, T. Ando and K. Ohya. Nucl. Instrum. and Meth. B **59/60** (1991) 572.

[Tho82] R.D. Thompson and K.N. Tu, Appl. Phys. Lett. **41** (1982) 440

[Ven98] V.C. Venezia, D.J. Eaglesham, T.E. Haynes, A. Agarwal, D.C. Jacobson, H.-J. Gossmann and F.H. Baumann. Appl. Phys. Lett. **73** (1998) 2980

[Ven99] V.C. Venezia, T.E. Haynes, Aditya Agarwal, L. Pelaz, H.-J. Gossmann, D.C. Jacobson and D.J. Eaglesham, Appl. Phys. Lett. 74 (1999) 1299

[Vena92] D. Venables, K. S. Jones and F. Namavar, Appl. Phys. Lett. **60** (1992) 3147.

[Wen89] H. Wendt, H. Cerva, V. Lehmann and W. Palmer, J. Appl. Phys. 65 (1989) 2402

[Will01] J.S. Williams, M.J. Conway, B.C. Williams, J. Wong-Leung, Appl. Phys. Lett. 78 (2001) 2867

[Wong88] H. Wong, N.W. Cheung, P. K. Chu, J. Liu, J. W. Mayer, Appl. Phys. Lett. **52** (1988) 1023

[W-Leu95a] J. Wong-Leung, C.E. Ascheron, M. Petravic, R.G. Elliman and J.S. Williams, Appl. Phys. Lett. **66** (1995) 1231

[W-Leu95b] J. Wong-Leung, E. Nygren and J. S. Williams, Appl. Phys. Lett. 68 (1995) 416

[W-Leu98] J. Wong-Leung, D.J. Eaglesham, J. Sapjeta, D.C. Jacobson, J.M. Poate and J.S. Williams, J. Appl. Phys. **83** (1998) 580

[W-Leu99] J. Wong-Leung, J. S. Williams, A. Kinomura, Y. Nakano, Y. Hayashi and D. J. Eaglesham, Phys. Rev. B 59, (1999) 7990

[Zau98] P. Zaumseil, Phys. Stat. Sol. (a) **165** (1998) 195

[Zhou93] D. S. Zhou, O. W. Holland and J. D. Budai, Appl. Phys. Lett. 63 (1993) 3580

Abbreviations

a.u.	arbitrary units
AL	Amorphous layer
BESOI	Bond and Etched Silicon on Insulator
BF	Bright field
Cz	Czochralski silicon
DF	Dark field
DLTS	Deep Level Transient Spectroscopy
Epi	Epitaxial silicon
FA	Furnace annealing
FZ	Float zone silicon
HF	High fluence
HT	High temperature
LF	Low fluence
MBE	Molecular beam epitaxy
PAS	Positron annihilation spectroscopy
RBS	Rutherford backscattering spectrometry
RBS/C	Rutherford backscattering channeling spectrometry
RT	Room temperature
RTA	Rapid thermal annealing
SAED	Selected area electron diffraction
SIMS	Secondary ion mass spectrometry
TDS	Thermal diffuse scattering
TEM	Transmission electron microscopy
TED	Transient enhanced diffusion
TF	Subthreshold fluence
TRIM	Transport of ions in matter
V-O	Vacancy-oxygen complexes
XRD	X-ray diffraction

Symbols

α	Average number of excess vacancies per depth interval per implanted ion
α_{He}	Average number of excess vacancies per depth interval per implanted He^+ ion
α_{Si}	Average number of excess vacancies per depth interval per implanted Si^+ ion
c_{cav}	Concentration of nanocavities
c_{Cumax}	Maximum concentration of Cu chemisorbed on the inner walls of the $R_P/2$ cavities
C_V	Monovacancy concentration
d; d_{hkl}	Lattice plane distance
λ	wavelength
E_{RP}	Binding energy for Cu in the R_P region
$E_{RP/2}$	Binding energy for Cu in the $R_P/2$ region
F	Compensation factor
ϕ	Fluence
$\varnothing$	Mean diameter of cavities
g	Diffraction (reflective plane) vector
I_E	Number of excess interstitials generated per implanted ion
I_{Si}	Concentration of Si self interstitials bound in loops
ξ_g	Extinction length of the microscope for the actual diffraction vector g
l	vector joining the black to the white lobe of a TEM image of a loop
θ	Angle of incidence of the ion beam
θ_{Bragg}	Bragg angle given by the Bragg's law for constructive interference
T	Temperature
R	Range
R_P	Mean projected ion range (projection of R along the direction perpendicular to the surface of the wafer)
ΔR_P	Range straggling
ω	Angle between the incident X-rays and the sample surface
Vc	Total volume of nanocavities
$\mathrm{V_E}$	Number of excess vacancies generated per implanted ion
x	Thickness of the amorphous surface layer of the ion-milled XTEM specimen

x_j	Junction depth
χ_{min}	Minimum channeling yield

Acknowledgments

There are numerous people to whom I am greatly indebted for having helped me in this work.

I would like to express my sincere gratitude to Prof. Dr. Wolfhard Möller, for giving me the great opportunity to work in the Institute of Ion Beam Physics/Forschungszentrum Rossendorf, for initiating my PhD project and the support he gives to the PhD students.

I am greatful to my supervisor, Dr. Reinhard Kögler, for introducing and guiding me in the field of Ion Beam Physics. His expertise, understanding, and patience, added considerably to my work. I would like to thank him for his assistance in writing reports (i.e. publications and this thesis).

I would like to acknowledge the head of the New Materials Group, Dr. Wolfgang Skorupa, for the scientific support and encouragement he provides in all levels of this research project. I would like also to thank him for letting me take part in many international collaborations and conferences.

I would like to thank Dr. Arndt Mücklich, Dr. Peter Werner/MPI Halle and Dr. Paulo Fichtner/UFRGS Porto Alegre, Brazil for introducing me in the TEM field and supervising my work in the TEM laboratory. I would like to thank all of the members of the TEM Lab in the Institute of Ion Beam Physics for the great working environment and their help in preparing a huge number of TEM specimens.

I am very grateful to Prof. Dr. Moni Behar and Dr. Paulo Fichtner from the Federal University of Rio Grande do Sul, Porto Alegre, Brazil for introducing me in the field of Ion Beam Analyses techniques, for their support and good discussions during my stay in the Ion Implantation Lab at the Institute of Physics in Porto Alegre.

Many thanks go to my colleagues in the New Materials Group. The friendly and supportive atmosphere inherent to the New Materials Group contributed essentially to the final outcome of my studies.

I would like also to thank Dr. Per Perrson/University of Linköping, Sweden for showing me the cleaving technique for XTEM specimen preparation.

I would like to thank Dr. Frank Eichhorn for performing the X-ray diffraction analyses.

I thank Mrs. Ingrid Beatus and Mrs. Gudrun Schnabel for the chemical cleaning and etching of a huge number of Si samples.

I express my deep thanks to Dr. Rossen Yankov and Dr. Maria Kalitzova/ Institute of Solid State Physics, Bulgarian Academy of Sciences, for engaging me in international collaboration with Forschungszentrum Rossendorf that introduced me in this PhD project.

I would like to thank my PhD fellows and friends in Dresden: Aneta Jordanova, Galina Satchanska, Galina Radeva, Stefka Zotova, Radinka Kojuharova and Georgi Furlinski for the good time we had together in the last years.

I would like to thank my family for the support they provided me through my entire life.

It would be impossible to mention all those who have helped and assisted me with my research over the past years. To all those who have contributed to this thesis whom I have lacked to mention, I would like to bestow a special word of thanks.

Veröffentlichungen in Rahmen dieser Arbeit

R. Koegler, A. Peeva, W. Anwand, G. Brauer, W. Skorupa, P. Werner and U. Gösele, Experimental evidence for interstitial defects away of the projected ion range of high energy ion implanted and annealed silicon, Appl. Phys. Lett. **75** (1999) 1279

R. Koegler , A. Peeva, W. Anwand, P. Werner, A.B. Danilin, W. Skorupa, Gettering centres for metals and oxygen formed in MeV-ion-implanted and annealed silicon, Solid State Phenomena **70** (1999) 235

A. Peeva, R. Koegler, P. Werner, A.A.D. de Mattos, P.F.P. Fichtner, M. Behar and W. Skorupa, Evidence for interstitial-type defects in the $R_P/2$ region of MeV-self-ion-implanted silicon produced by standard ion milling procedure, Nucl. Instrum. and Meth. In Phys. Res. B 161-163 (2000) 1090

P. F. P. Fichtner, A. Peeva, M. Behar, G. de M. Azevedo, R. L. Maltez, R. Koegler and W. Skorupa, He-induced cavity formation in silicon upon high-temperature implantation, Nucl. Instrum. and Meth. In Phys. Res. B 161-163 (2000) 1038

P. F. P. Fichtner, M. Behar, J. R. Kaschny, A. Peeva, R. Koegler and W. Skorupa, Copper gettering at half of the projected ion range induced by low - energy channeling He implantation into silicon, Appl. Phys. Lett. 77 (2000) 972

A. Peeva, R. Kögler, G. Brauer, W. Skorupa and P. Werner, Metallic impurity gettering to defects remaining in the $R_P/2$ region of MeV-ion implanted and annealed silicon,
Materials Science in Semiconductor Processing 3 (2000) 297

A. Peeva, P.F.P Fichtner, M. Behar, R. Koegler, W. Skorupa,
Helium implantation induced metal gettering in silicon at half of the projected ion range,
Nucl. Instr. Meth, B **175** (2001) 176

R. Kögler, A. Peeva, F. Eichhorn, J.R. Kaschny, M. Voelskow, W. Skorupa, H. Hutter, Implantation induced defects in silicon detected by Cu decoration technique, Electrochem. Soc. Proc. **29** (2001) 133

R. Kogler, A. Peeva, P. Werner, W. Skorupa, U. Gösele,
Gettering centres in high-energy ion-implanted silicon investigated by point defect recombination, Nucl. Instr. Meth, B **175** (2001) 340

R. Koegler, A. Peeva, J. Kaschny, W. Skorupa and H. Hutter,
Defect Engineering and Prevention of Impurity Gettering at $R_P/2$ in Ion - Implanted Silicon, Solid State Phenomena **82-84** (2002) 399

R. Koegler, A. Peeva, J. Kaschny, W. Skorupa, H. Hutter,
Prevention of impurity gettering in the $R_P/2$ region of ion-implanted silicon by defect engineering, Nucl. Instr. Meth, B **186** (2002) 298

A. Peeva, P.F.P. Fichtner, D.L. da Silva, M. Behar, R. Koegler and W. Skorupa,
Gettering of copper in silicon at half of the projected ion range induced by helium implantation, Journal of Appl. Phys. **91** (2002) 69

A. Peeva, R. Koegler, W. Skorupa,
Visualisation of vacancy type defects in the $R_P/2$ region of ion implanted and annealed silicon, Nucl. Instr. Meth B, **206** (2003) 71

Weitere Veröffentlichungen

Y. M. Guerguiev, R. Koegler, A. Peeva, D. Panknin, A. Muecklich, R. Yankov and W. Skorupa, Impurity gettering by high-energy ion implantation in silicon beyond the projected range, Appl. Phys. Lett. 75 (1999) 3467

Y. M. Gueroguiev, R. Koegler, A. Peeva, D. Panknin, A. Muecklich, R. Yankov and W. Skorupa, High-energy ion-implantation-induced copper gettering in silicon beyond the projected ion range: the trans-projected range effect, Journal of Appl. Phys. 88 (2000) 5645

Y. M. Gueorguiev, R. Koegler, A. Peeva, D. Panknin, A. Muecklich, R. Yankov and W. Skorupa, Trans-projected-range gettering of copper in high-energy ion-implanted silicon, to be published in Journal of Appl. Phys. 88 (2000) 6934

Y. M. Gueroguiev, R. Koegler, A. Peeva, D. Panknin, A. Muecklich, R. Yankov and W. Skorupa, Trans-projected-range effect in proximity gettering of impurities in silicon,
Vacuum 62 (2001) 309

D.L.da Silva, P.F.P Fichtner, A. Peeva, M. Behar, R. Koegler, W. Skorupa,
The effects of implantation temperature on He bubble formation in silicon,
Nucl. Instr. Meth, B **175** (2001) 335

K. Gammer, M. Gritsch, A. Peeva, R. Koegler, H. Hutter,
SIMS investigations of gettering centers in ion-implanted and annealed silicon,
J. Trace Microprobe Tech. **20** (2002) 47

D.L. da Silva, P.F.P. Fichtner, M. Behar, A. Peeva, R. Koegler, W. Skorupa,
Implantation temperature dependence of He bubble formation in Si,
Nucl. Instr. Meth, B 190 (2002) 756

Versicherung

Hiermit versichere ich die vorliegende Arbeit ohne unzulässige Hilfe Dritter und ohne Benutzung anderer als der angegebenen Hilfsmittel angefertigt habe. Die aus fremden Quellen direkt oder indirekt übernommenen Gedanken sind als solche kenntlich gemacht. Die Arbeit wurde bisher weder in Inland noch im Ausland in gleicher oder ähnlicher Form einer anderer Prüfungsbehörde vorgelegt.

Diese Arbeit wurde am Institut für Ionenstrahlphysik und Materialforschung des Forschungszentrums Rossendorf e.V. unter Betreuung von Dr. Reinhard Kögler und Dr. Wolfgang Skorupa angefertigt.

Die Promotionsordnung der Fakultät Mathematik und Naturwissenschaften der Technischen Universität Dresden in der Fassung vom 20 März 2000 wird anerkannt.

Dresden, 19 Dezember 2001